DISSERTATION

PART I: STRUCTURAL CHARACTERIZATION OF DOPED NANOSTRUCTURED MAGNESIUM: UNDERSTANDING DISORDER FOR ENHANCED HYDROGEN ABSORPTION KINETICS

PART II: SYNTHESIS, FILM DEPOSITION, AND CHARACTERIZATION OF QUATERNARY METAL CHALCOGENIDE NANOCRYSTALS FOR PHOTOVOLTAIC APPLICATIONS

Submitted by

Max B. Braun

Department of Chemistry

In partial fulfillment of the requirements

For the Degree of Doctor of Philosophy

Colorado State University

Fort Collins, Colorado

Fall 2017

Doctoral Committee:

Advisor: Amy Prieto

Richard Finke
Anthony Rappe
James Neilson
Jose de la Venta

ABSTRACT

PART I: STRUCTURAL CHARACTERIZATION OF DOPED NANOSTRUCTURED MAGNESIUM: UNDERSTANDING DISORDER FOR ENHANCED HYDROGEN ABSORPTION KINETICS

PART II: SYNTHESIS, FILM DEPOSITION, AND CHARACTERIZATION OF QUATERNARY METAL CHALCOGENIDE NANOCRYSTALS FOR PHOTOVOLTAIC APPLICATIONS

The production, storage, and subsequent consumption of energy are at the foundation of all human activity and livelihood. The theme of this dissertation is the pursuit of fundamental understanding of the chemistry of materials that are used for energy production and storage. A strong emphasis is placed on a synthetic foundation that allows for systematic investigation into the fundamental chemistry that controls the applicable properties of the materials of interest. This dissertation is written in the "journals format" style—which is accepted by the Graduate School at Colorado State University—and is based on one peer-reviewed publication that has appeared in C*hemistry of Materials* as well as two manuscripts to be submitted, one to *The Journal of Physical Chemistry C*, and one to *ACS Applied Materials and Interfaces*. In order to create a context for these publications, Chapters 1 and 3 provide an overview of the motivations for the projects, and then continue to detail the initial synthetic investigations and considerations for the two projects.

In addition to recounting Mg nanocrystals synthetic refinement that was necessary for reproducible hydride kinetic analysis, Chapter 1 also briefly introduces some of the conventional models used for fitting of the hydriding kinetics data. Furthermore, initial investigations into the

use of these models for our system are presented. Chapter 2 is a paper to be submitted to the *The Journal of Physical Chemistry C* that describes the local and extended structure characterization of Mg nanocrystals (NCs) with a small amount of nickel added during synthesis. Ni has a dramatic effect on the de/hydriding kinetics of Mg NCs, and this chapter describes the use of a combination of multiple state-of-the-art characterization techniques to gain insight into the structural perturbations due to Ni inclusion in the Mg NCs. This insight is then used to establish the characteristics of Ni inclusion that results in the enhanced hydrogen absorption processes.

Chapter 3 introduces the many considerations needed to be taken into account during the development of a novel synthesis for copper zinc tin chalcogenide colloidal nanocrystals. In addition to introducing synthetic approaches to achieve this goal, Chapter 3 also describes essential characteristics that need to be considered for further investigation into the properties of films made from the nanocrystals. Chapter 4 is a publication that appeared in *Chemistry of Materials*, that describes an approach to tuning the surface and ligand chemistry of Cu_2ZnSnS_4 nanocrystals for use as an absorber layer in next generation photovoltaic devices. The publication describes ligand exchange chemistry achieved via layer-by-layer dip-casting of nanocrystal thin films, and the effects that this exchange chemistry has on the resulting films. It also details the fabrication of full photovoltaic (PV) devices to characterize the benefits of controlling the surface chemistry can have on PV performance. Chapter 5 is a paper—to be submitted to *ACS Applied Materials and Interfaces*—that describes the investigations into how varying the chalcogen ratio (i.e., S:Se) leads to changes in the physical and electrical properties of thin films made from $Cu_2ZnSn(S_{1-x}Se_x)_4$ (where $0 < x < 1$) NCs. It highlights the novel synthetic procedure (detailed in chapter 3) that was required for a systematic, deconvoluted evaluation of S:Se composition on the materials optical and electronic properties. Moreover, the characteristics of full PV devices based on thin films of

each stoichiometry (x=0 to x=1) are assessed to establish a relationship between composition and the materials performance.

TABLE OF CONTENTS

PART I: STRUCTURAL CHARACTERIZATION OF DOPED NANOSTRUCTURED MAGNESIUM: UNDERSTANDING DISORDER FOR ENHANCED HYDROGEN ABSORPTION KINETICS

CHAPTER 1: SYNTHESIS AND HYDRIDING KINETICS CHARACTERIZATION OF MAGNESIUM NANOPARTICLES FOR HYDROGEN STORAGE[1]

1.1 Nanostructured magnesium hydride for hydrogen storage

Hydrogen is a desirable fuel due to its earthly abundance, high energy density as molecular hydrogen (142 MJ/kg), and potential to lower harmful carbon emissions ($H_2 + O_2 \leftrightarrow H_2O$ + energy) if utilized.[1,2] One of the major challenges towards realizing a hydrogen fuel economy is the safe, practical storage of it. While the conventional stores (i.e., high pressure gas or liquid H_2 tanks) can be utilized for stationary storage, alternatives must be devised for transportation applications.

With a relatively high hydrogen content (7.6 wt %) magnesium hydride, offers an attractive alternative to the conventional storage techniques. Hydrogen storage in magnesium is founded on its reversible reaction with molecular hydrogen:

$$H_2(g) + Mg(s) \overset{\Delta}{\leftrightarrow} MgH_2\ (s) \qquad \Delta H\text{=-75 kJ/mol} \quad (1)$$

However, the high temperatures and extreme pressures required to overcome large kinetic and thermodynamic barriers associated with reaction (1), prevent its use as a practical hydrogen store.[1,2] One approach towards lowering these kinetic and thermodynamic barriers is the reduction of the magnesium or magnesium hydride crystallite size to the nanoscale.[3-6] While nanostructuring of the magnesium (hydride) has undoubtedly increased the kinetics of hydrogenation (dehydrogenation), it was recently calculated that modification of the thermodynamics of reaction

[1] The experimental content and writing of this chapter was done by Max B. Braun. Amy L. Prieto provided guidance and conceptual insight. The initial synthetic procedures leading to this work were performed by Timothy Arthur.

(1) does not occur until crystallite sizes below 5 nm.[7-9] In order to overcome these thermodynamic drawbacks, the addition of other metals and metal oxides to the magnesium hydride system has been calculated and experimentally verified to be effective in altering reaction (1)'s thermodynamics.[2,7,10-13] For the sake of developing a material that contains desirable kinetic and thermodynamic characteristics, a fundamental understanding and deconvolution of the mechanisms of enhancement due to size and catalyst addition must be achieved.

Historically, nanostructuring and catalyst addition has most often been achieved via top-down methods (e.g., ball-milling).[3] However, these methods tend to lead to little control over crystallite size, and can produce undesirable impurities that can convolute the effects of size and catalyst addition.[2,14] Alternatively, bottom-up methods provide a route towards greater control over crystallize size, while still allowing the ability for catalyst addition.[2,6,15,16] Of these methods, Norberg *et al.* reported on an adapted solution-based Reike method for the synthesis of magnesium nanocrystals allowed for the systematic investigation into the role of particle size on reaction's kinetics, (eq. 1).[4,17] Through the simple addition of a metal precursor of choice, this method also offers a path towards facile catalyst addition (Scheme 1.1):

Scheme 1.1. Synthesis of Mg and Mg(x%Ni) NCs

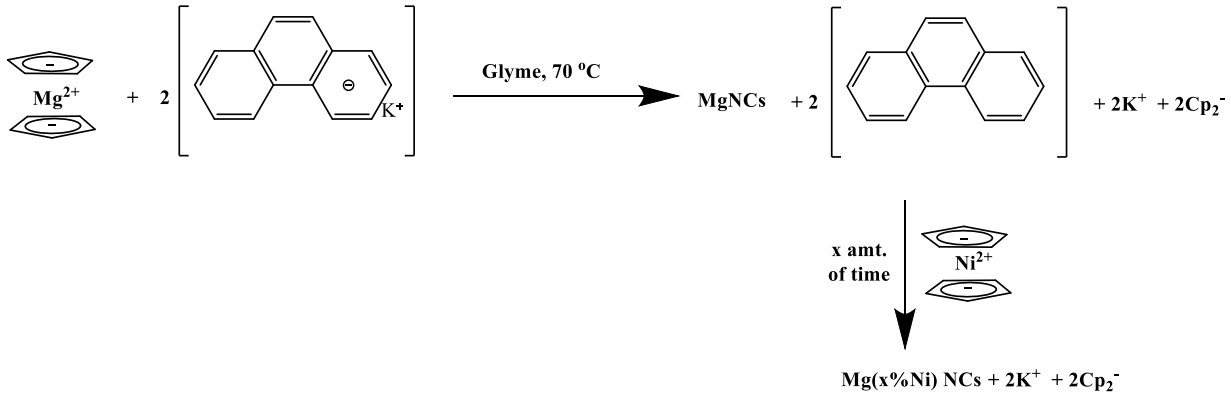

Ultimately, due to its control over crystallite size, this method allows for the systematic deconvolution of particle size, and the role of additive metals on the kinetics and thermodynamics of reaction (1).

To uncover the mechanism of hydrogenation/dehydrogenation in nanostructured magnesium with and without catalyst addition, different kinetic models, specifically single particle analysis (SPA) models have been investigated extensively in the literature.[13,18-20] Of these SPA models, the various forms of the Johnson-Mehl-Avrami (JMA) semi-empirical model (also encompassing the Kolmorogov-Johnson-Mehl-Avrami model) are used the most often in the evaluation and comparison of the mechanisms of hydrogenation and dehydrogenation for magnesium based hydrogen storage systems.[4,18,19,21-33] This model is based on the nucleation and growth of a new phase upon hydrogenation/dehydrogenation.[18,21-23,25] Alternatively, the contracting volume (CV) model is sometimes used to fit hydrogenation and dehydrogenation data. This model is based on instantaneous nucleation of a phase at the surface of a volume, followed by contraction (or migration inwards) of that volume towards the center of the volume.[19,20] Both of these semi-empirical models have often been applied in their basic linear forms shown in equations (2, JMA) and (3, CV):

$$[-\ln(1-\alpha)]^{1/n} = kt \quad (2)$$

$$1-[1-\alpha]^{1/n} = kt \quad (3)$$

where k is the kinetic rate parameter, t is time, and n is often referred to as the dimensionality of growth.[14,19,27] Successful fitting of the kinetics with these models would supposedly give a value for the rate parameter, as well as provide information about the rate limiting step in the reaction. However, the applicability of the JMA and CV models to chemical phase transitions of this nature

is questionable. This skepticism is in part due to the assumptions made in the application of the JMA model to these nanoparticulate systems, and in part due to the ability of these models to deliver physically and chemically relevant data.[18,24,25,33] The Finke-Watzky two step mechanism of nucleation and autocatalytic growth:

$$A \xrightarrow{k_1} B \quad (4)$$

$$A + B \xrightarrow{k_2} 2B \quad (5)$$

could also be applicable in fitting the kinetics, although it has not yet been applied to the Mg|H_2 system in the literature. In this model, the A phase would be the Mg (MgH_2) and the B phase would be the MgH_2 (Mg) for the hydrogenation (dehydrogenation).[34]

Herein, we describe the bottom-up synthesis of magnesium nanocrystals, with and without Ni additive. We also discuss and sensitivity of this synthesis, and the role that this sensitivity plays on the analysis of the hydrogen reaction kinetics. Furthermore, we present our initial investigations into the applicability of different kinetics models that are conventionally used to fit these reactions.

1.2 Experimental

1.2.1 Magnesocene synthesis

The synthesis of magnesocene ($Mg(cp)_2$) was performed following a procedure, developed in house, using di-*n*-butyl magnesium (1.0 M in heptane), or a literature procedure *n*-butyl-*sec*-butyl magnesium (0.7 M in heptane).[35] The other precursor, dicyclopentadiene (reagent grade), was purchased from Aldrich Chemical Co. and used as purchased. All of the procedures were performed using standard N_2 Schlenk line techniques, unless otherwise noted.

Inside a nitrogen glovebox, a 250 mL triple neck round-bottomed flask was charged with a Teflon stir bar 100 mL of di-*n*-butyl magnesium (1.0 M in heptane) or 143 mL *n*-butyl-*sec*-butyl magnesium (0.7 M in heptane). The flask was capped with septa and, outside the glovebox, introduced to N_2 pressure and stirred. Approximately 8.4 mL of freshly cracked cyclopentadiene (cp) was then added dropwise. When the Mg precursor was di-*n*-butyl magnesium, this addition was done over ice. Once the addition was completed, the reaction was allowed to stir for 30 minutes, yielding a white precipitate. The round-bottomed flask was then pumped into a N_2 glovebox for washing. The white precipitate was then washed multiple times with cold, dry hexanes over vacuum filtration, and allowed to dry. The product was originally used as is, or eventually was purified via sublimation before further use. The product purity was verified by ^{1}H nuclear magnetic resonance (NMR) spectroscopy on an Agilent Inova 400 MHz NMR in deuterated benzene or chloroform.

1.2.2 Undoped magnesium nanocrystal synthesis

The synthesis of the magnesium nanocrystals (Mg NCs) was performed as described previously, with potassium phenanthrene as the reducing agent.[4] In preparation for synthesis, 1,2-dimethoxy ethane (glyme, Sigma-Aldrich, anhydrous, 99.99%) was originally refluxed over sodium (Sigma-Aldrich 99.5%) and benzophenone (Sigma-Aldrich 99%) for ~1-2 hours and then collected via distillation. Alternatively, the glyme was refluxed over phenanthrene (Sigma-Aldrich 98%) and potassium (Sigma-Aldrich 99.95%) for >6 hours before distillation.

The following procedure was performed in a N_2 glovebox. In a typical undoped Mg nanocrystal (NC) reaction, a reducing solution of potassium (0.5 M), phenanthrene (0.5 M), and freshly distilled glyme were stirred for 2 hours to provide a dark green solution. This solution was then centrifuged for 10 minutes to remove any undissolved particulate. A separate solution

(0.05 M) of freshly distilled glyme and magnesocene (prepared in-house) was heated to 70 ºC under vigorous stirring, giving a clear solution. Once the reaction reached temperature, the reducing solution was rapidly added to the magnesocene solution, resulting in a dark green solution with dark grey precipitate. The resulting solution was then allowed to stir for 30 minutes to complete the reaction.

For nickel doping, nickelocene ($NiCp_2$, Strem Chemicals, 99%) and glyme were mixed to provide a turquoise solution (0.01 M) with the desired weight % Ni (1-20 %) compared to Mg. For ease of discussion and presentation, these samples are referred to by the amount of Ni (wt %) added (e.g., 5 wt % Ni added= Mg-5Ni). This solution was added dropwise 1 minute after the reducing solution was added to the magnesocene solution. As with the undoped particles, this solution was allowed to stir for 30 minutes to complete the reaction.

The resulting particles were collected via centrifugation, followed by a wash with 1-3 mL of distilled glyme. This solution was then centrifuged, and the supernatant discarded. The wash process was repeated at least three times, until the supernatant was clear. The precipitated powder was then dried under vacuum until dry. The product was stored in the N_2 glovebox until further use.

In order to verify the crystallinity of the as-made particles, powder X-ray diffraction (XRD) was performed on a Scintag X2 Advanced Diffraction system equipped with Cu Kα radiation (λ = 1.54 Å) using a zero background SiO2 sample holder. The elemental composition of the particles was measured via energy dispersive spectroscopy (EDS) in a JEOL JSM 6500F FE-scanning electron microscopy (SEM) equipped with an EDAX OCTANE SUPER silicon drift detector. The size and morphology of the NCs were analyzed via imaging on a JEOL JEM-1400 TEM at a working voltage of 100 kV. After hydrogenation, the particles were subjected to

the same characterization techniques. In addition to the characterization described above, the particles were subjected to further extended and local structure characterization described in Chapter 2.

1.2.3 Hydrogen cycling of the nanocrystals

The hydrogen cycling of the (doped and undoped) magnesium NCs was performed using a homebuilt Sieverts apparatus equipped with both a high pressure (0-35000 Torr) and low pressure (0-1500 Torr) gauge. The pressure of the system was recorded digitally every 0.5 to 1 seconds. For a typical measurement, the sample holder was charged with 10-30 mg of product in a N_2 glovebox. The sample holder was then attached to the Sieverts apparatus, which was then pumped and purged with H_2 at least 3 times. The sample was then exposed to vacuum and heated to the desired reaction temperature (250 to 300 °C). Hydrogenations were performed by exposure of the particles to H_2 pressures ranging from 7600-7900 Torr. Dehydrogenations were executed at H_2 pressures ranging ~360-500 Torr, at temperatures ranging from 325 to 375 °C.

By measuring the change in pressure over time in the Sieverts apparatus, the molar amount of hydrogen (n) adsorbed or desorbed by the material can be calculated using the ideal gas law. [36] From here, a percent hydrogenation can be determined according to equation (2):

$$\%\ Hydrogenation = \frac{mass\ H_2}{mass\ Mg + mass\ H_2} \tag{6}$$

which can then be used to calculate the converted fraction of material, α, where:

$$\alpha = \frac{H_2 weight\ \%}{Maximum\ H_2 weight\ \%} \tag{7}$$

α can then be plotted vs. time and fit to compare the kinetics of hydrogenation and dehydrogenation. Furthermore, these plots can be used for the fitting of the different kinetic

models that are used in kinetic analysis. The non-linear kinetics fitting was performed using Origin 9.1 with the Levenberg-Marquardt algorithm performing the iterations.

1.3 Generating reproducible hydrogen cycling kinetics: an investigation of the synthetic procedures

1.3.1 Variability in hydrogen cycling capabilities

Initial investigation into the hydrogen cycling kinetics of the magnesium NCs with Ni resulted in dramatic sample to sample variation in both performance, and hydrogen capacity (Figure 1.1). The samples, although hydrogenated at different temperatures (250 to 300 °C), were absorbing anywhere from 2.5 to 6.1 wt% H_2. However, each sample was able to desorb close to the same amount that it had adsorbed (~2.5-6.1 wt %). For these initial samples, there seemed to be no trend with hydrogenation/dehydrogenation temperature, which led us to question the variability due to the synthesis. Furthermore, even when temperature was not varied, there was still considerable variability in the dehydrogenation kinetics (Figure 1.1). Figure 1.1 also displays the ability of the Mg-5Ni samples to desorb hydrogen at a significantly improved rate (at 350 °C). To investigate this observation more thoroughly, it was necessary to reduce the sample to sample deviation (Figure 1.1b). This lead us to reinvestigate the synthetic procedure developed by Norberg *et al.*[4]

1.3.2 Magnesocene synthesis and glyme distillation

During the synthesis of Mg NCs, the $Mg(cp)_2$ dissolved in glyme would occasionally turn yellow upon heating. Most often, however, this solution would remain clear. In order to avoid this variability, we investigated the quality of these two chemicals, that is, the $Mg(cp)_2$ and the distilled glyme. $Mg(cp)_2$ was the first area of synthetic refinement we investigated. Originally, the

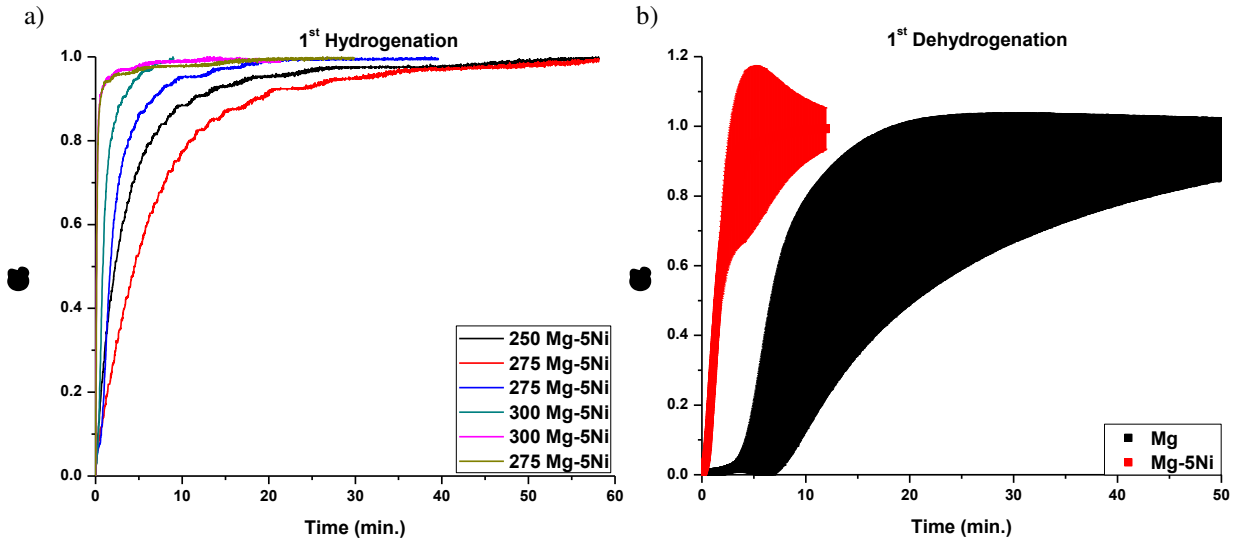

Figure 1.1. (a) Kinetics of hydrogenation of Mg (5 wt % Ni added) at different temperatures. The number (250 – 300) in the legend corresponds to the temperature (°C) of hydrogenation. (b) The averaged kinetics of dehydrogenation (350 °C) for Mg and Mg (5 wt % Ni added). The standard deviation from sample to sample is exhibited as the width of the line.

synthesis of $Mg(cp)_2$ was performed using 1.0 M di-*n*-butyl-magnesium in heptane (see section 1.2.1). Although the product that precipitated when cyclopentadiene was added to the magnesium precursor was usually crystalline in appearance, there was occasionally a viscous white residue that also precipitated. The identity of this secondary product was difficult to analyze, due to its insolubility in the available NMR solvents. Nonetheless, we chose to investigate alternative synthetic routes for the magnesocene.

In the book, *Organomagnesium methods in organic synthesis*, a procedure is described that uses *n*-butyl-*sec*-butyl magnesium (0.7 M in heptanes) as the precursor for a magnesocene synthesis. Due to the difference in the stability of the carbocation formed when the cp takes place of *sec*-butyl on the magnesium, *n*-butyl-*sec*-butyl is a more reactive precursor. This could potentially lead to a more complete reaction. Nonetheless, having an established literature procedure to follow led to a more crystalline product, without any evidence for the viscous residue. Furthermore, the literature-based synthetic procedure called for sublimation (at 50 °C) of the

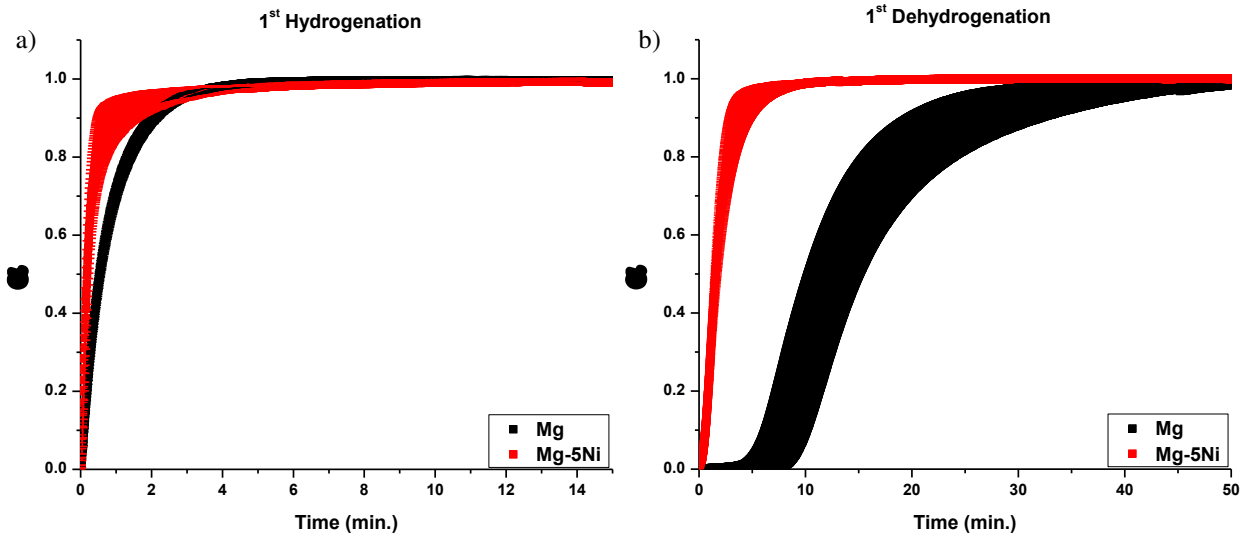

Figure 1.2. Averaged kinetics of (a) hydrogenation at 300 °C and (b) dehydrogenation at 350 °C for multiple Mg and Mg (5 wt % Ni added) samples. The width of the lines represents the standard deviation.

precipitate after washing with cold hexanes. This lead to highly crystalline product that was verified to be 99% pure (δ=5.97 ppm) by NMR in C_6D_6 (small additional peak at ~δ=2.6 ppm).

The second issue of concern was the purity of the glyme. In order to minimize the number of chemicals introduced into the system, we chose to change our distillation procedure. We began distilling the glyme over potassium and phenanthrene, the same chemicals used in the reduction of the magnesocene. Similar to the indigo color of fully reduced benzophenone, reduced phenanthrene also produces a deep-green color when dissolved in a dry solvent. In this way, phenanthrene functioned as an indicator that our glyme was done refluxing, and ready for distillation. The use of freshly distilled glyme (i.e., within the same day as distillation), was found to be imperative for the glyme-$Mg(cp)_2$ solutions color to remain clear. If the glyme was exposed to the N_2 glovebox atmosphere and left to age, the solution would turn yellow. This suggests that even the small amount ([H_2O],[O_2] <0.1ppm) of water/oxygen/or other organic impurities in the glovebox can affect this reaction. This lead us to establish a protocol that involved purging the box

Table 1.1. Kinetic equations used for fitting experimental sorption data Ref. [19]

Model Equation(F(α))	Description
$[-\ln(1-\alpha)]^{1/3} = kt$	JMA3: nucleation and growth; three-dimensional growth of existing nuclei with constant interface velocity. *n*=3
$[-\ln(1-\alpha)]^{1/2} = kt$	JMA2: nucleation and growth; two-dimensional growth of existing nuclei with constant interface velocity. *n*=2
$1-(1-\alpha)^{1/3} = kt$	CV3: contracting volume; three-dimensional growth with constant interface velocity that determines kinetics. *n*=3
$1-(1-\alpha)^{1/2} = kt$	CV2: contracting volume; two-dimensional growth with constant interface velocity that determines kinetics. *n*=2
$1-\left(\frac{2\alpha}{3}\right)-(1-\alpha)^{2/3} = kt$	CVd: contracting volume; three-dimensional growth with decreasing interface velocity that determines kinetics. *n*=3

with fresh N_2 before exposure of the glyme to the glovebox's N_2 atmosphere.

The observation of the sensitivity of the glyme-$Mg(cp)_2$ to small amounts of impurity led us to realize the sensitivity of our reaction to minute changes. This led us to establish a protocol that described the discrete steps and timing of the synthesis of the Mg NCs (see section 1.2.2). This led to much less sample to sample variation in dehydrogenation kinetics, as is exhibited in Figure 1.2. These samples also exhibited much more reproducible hydrogen capacities of 6.60 ± 0.25 and 6.38 ± 0.33 wt % H_2 for the Mg and Mg-5Ni composite, respectively.

As was suggested in Figure 1.1, Figure 1.2 verifies the ability for the Mg-5Ni NCs to adsorb and desorb hydrogen faster than the pure Mg counterpart. In the next section, we describe our initial investigations of fitting to different kinetics models and their ability/inability to uncover the mechanism of enhancement due to Ni incorporation.

1.4 Modelling of hydrogenation and dehydrogenation kinetics

As mentioned in section 1.1, the linear versions of the CV and JMA models have most often been used in the determination of a reactions kinetics. As such, our initial attempts at fitting with the kinetics models was done using these forms (Figure 1.3). First, this involves the

acquisition of kinetics data (i.e., α vs. t), followed by the input of this data into one of the various linear forms (Table 1.1) of these model equations, F(α). The plot of F(α) versus time can then be fit to generate kinetics data. As is evident in Figure 1.3, plotting the linear forms of these equations with the hydrogenation data of a Mg-5Ni sample data did not yield a line for any of the different model functions.

Consequently, we investigated fitting the kinetic data (α vs. t) to the equations directly (Figure 1.3). Rearranging equations 2 and 3 for α yields the non-linear forms of the JMA (eq. 8) and CV (eq. 9) equations:

$$\alpha = 1 - e^{-(kt)^n} \tag{8}$$

$$\alpha = 1 - (1 - kt)^n \tag{9}$$

Where the values for *k* and *n* can be derived upon successful fitting of the data. Additionally, we also attempted to fit the data with a derived form (equation 10) of the integrated rate equation from the Finke-Watzky mechanism (equations 4 and 5).

$$\alpha = 1 - \frac{k_1 + k_2'}{k_2' + k_1 \exp[(k_1 + k_2')t]} \tag{10}$$

As is displayed in Figure 1.3, the abilities of these equations to fit the hydrogenation of a Mg-5Ni sample are acceptable (R^2 >0.95 for all but the CV). However, fitting of the hydrogenations of both the Mg-5Ni, and a pure Mg sample is qualitatively less than adequate at capturing the transitions that occur in these systems. For all samples, the CV equation failed to fit almost entirely.

The inability for the JMA and CV models to adequately fit the hydrogenation and dehydrogenation data for our system is likely due to the assumptions made by these SPA models.

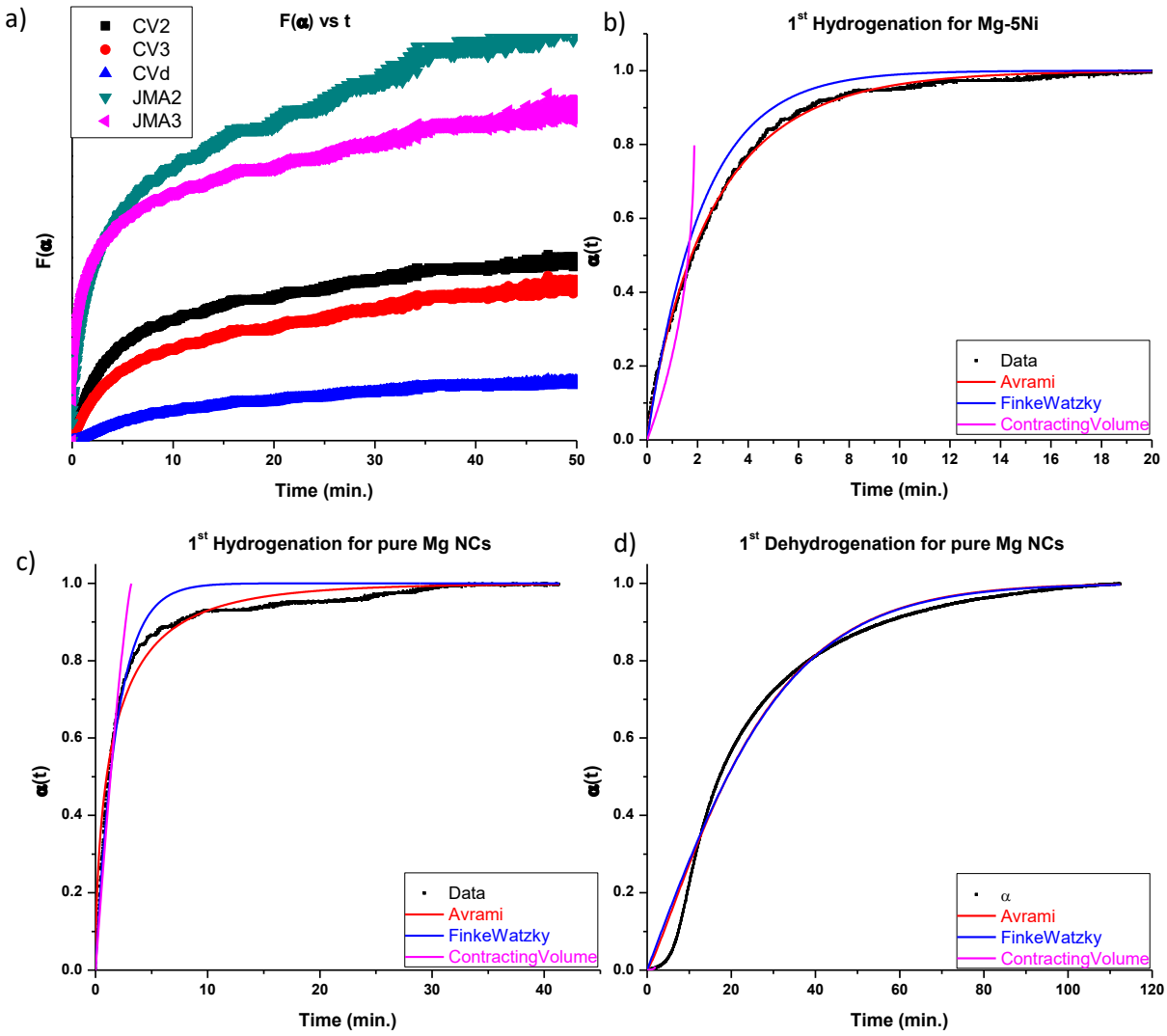

Figure 1.3. (a) Plots of F(α) vs. t for hydrogenation data for a typical Mg NC sample, where F(α) is derived from the linear forms of the kinetics equations in Table 1.1 Kinetics equation fitting of hydrogenation data for the 1st hydrogenation of a typical (b) Mg-Ni sample, (c) Mg NC sample, and the 1st dehydrogenation of a typical Mg NC sample.

Specifically, Mintz *et al*. states that these models assume that particle size and shape are irrelevant in the SPA modeling. However, for this to be an appropriate assumption, the initial thickness, X_0, of a hydrogenation (dehydrogenation) reaction must be much smaller than the total thickness of a particle, D. This does not necessarily hold true for nanoparticles and thus may be the cause of inconsistencies in modeling.[18] More recently, Dill *et al.* performed a series of crystal growth

simulations that address some of the assumptions the Kolmogorov-JMA model makes, and ways to derive physically relevant parameters from the model.[37] Similar to Mintz *et al.*, they discuss problems with assumptions made about particle size and shape, and suggest making corrections for the various characteristics (like anisotropy) in order to calculate a velocity of the phase boundary (which would give information about the rate limiting step).

Even with the successful fitting of the data with the JMA or CV model, the chemical meaning of the fit is still debatable. Without a minimal chemical mechanism to describe the different steps of the reaction, the understanding derived from the "kinetic rate parameter" is potentially minimal. This discussion is covered in detail by Finke *et al.* in their evaluation of the application of the Avrami based equations (termed the Erofe'ev-Avrami treatment) to various solid state systems. Essentially, attempts to fit reactions with the Finke-Watzky mechanisms integrated rate equation, as opposed to the JMA equation, requires the generation of two elementary chemical equations (equations 4 and 5) that would provide more chemical meaning to the kinetic rate parameter.[33] Nonetheless, from our initial attempts at fitting, the Finke-Watzky integrated rate equation still fails to adequately describe the data. The reason for this might be due to the complexity of the system at the nanoscale. With a large number of nucleation sites (due to high surface area) and numerous potential rate limiting steps (e.g, physisorption, chemisorption, diffusion, and bulk phase nucleation and growth) the model might require more steps than can described by equations (4) and (5).

1.5 Summary

Although magnesium hydride is a potential candidate for the solid-state storage of hydrogen fuel, it suffers from slow kinetics and large thermodynamic barriers for hydrogen input and uptake. The synthesis of magnesium nanoparticles from our bottom-up solution bases

synthesis provides a cheap, facile route towards elucidating the roles of particle size and catalyst addition on the hydrogenation and dehydrogenation reactions. Initially, however, the synthetic variability led to sample to sample variation in performance (kinetic and hydrogen capacity). Consequently, the synthesis was refined and the ability of Ni to enhance the kinetics of hydrogenation and dehydrogenation in Mg NCs was verified. While there exist multiple models to aid in describing the different mechanisms of hydrogenation and dehydrogenation of nanocrystals, initial attempts at fitting kinetic data with these existing solid-state kinetic models was unfortunately inadequate. As such, the mechanism of kinetic enhancement due to Ni inclusion requires further characterization. The successful fitting of the hydrogen sorption data may require alteration of the existing kinetic models, or perhaps the development of a new model all together. In order to gain insight into the role Ni plays in enhancing the kinetics of Mg NCs de/hydriding, local and extended structure characterizations are presented in the next chapter.

REFERENCES

(1) Aguey-Zinsou, K.-F.; Ares-Fernandez, J.-R. *Energy & Environmental Science* **2010**, *3*, 526.
(2) Shissler, D. J.; Fredrick, S. J.; Braun, M. B.; Prieto, A. L. In *Low-Cost Nanomaterials*; Lin, Z., Wang, J., Eds. 2014, p 297.
(3) Berube, V.; Radtke, G.; Dresselhaus, M.; Chen, G. *Int J Energ Res* **2007**, *31*, 637.
(4) Norberg, N. S.; Arthur, T. S.; Fredrick, S. J.; Prieto, A. L. *Journal of the American Chemical Society* **2011**, *133*, 10679.
(5) Bardhan, R.; Hedges, L. O.; Pint, C. L.; Javey, A.; Whitelam, S.; Urban, J. J. *Nat Mater* **2013**, *12*, 905.
(6) Liu, W.; Aguey-Zinsou, K.-F. *Journal of Materials Chemistry A* **2014**, *2*, 9718.
(7) Shevlin, S. A.; Guo, Z. X. *J Phys Chem C* **2013**, *117*, 10883.
(8) Vajeeston, P.; Ravindran, P.; Fichtner, M.; Fjellvåg, H. *The Journal of Physical Chemistry C* **2012**, *116*, 18965.
(9) Buckley, A. C.; Carter, D. J.; Sheppard, D. A.; Buckley, C. E. *The Journal of Physical Chemistry C* **2012**, *116*, 17985.
(10) Liang, G.; Huot, J.; Boily, S.; Van Neste, A.; Schulz, R. *J. Alloy. Compd.* **1999**, *292*, 247.
(11) Hanada, N.; Ichikawa, T.; Fujii, H. *The journal of physical chemistry. B* **2005**, *109*, 7188.
(12) Hanada, N.; Ichikawa, T.; Isobe, S.; Nakagawa, T.; Tokoyoda, K.; Honma, T.; Fujii, H.; Kojima, Y. *J Phys Chem C* **2009**, *113*, 13450.
(13) Korablov, D.; Nielsen, T. K.; Besenbacher, F.; Jensen, T. R. *Powder Diffraction* **2015**, *30*, S9.
(14) Ares-Fernández, J.-R.; Aguey-Zinsou, K.-F. *Catalysts* **2012**, *2*, 330.
(15) Shen, C.; Aguey-Zinsou, K.-F. *Journal of Materials Chemistry A* **2017**, *5*, 8644.
(16) Liu, T.; Qin, C. G.; Zhang, T. W.; Cao, Y. R.; Zhu, M.; Li, X. G. *J Mater Chem* **2012**, *22*, 19831.
(17) Rieke, R. D.; Li, P. T.-J.; Burns, T. P.; Uhm, S. T. *J. Org. Chem.* **1981**, *46*, 4323.
(18) Mintz, M. H.; Zeiri, Y. *J. Alloy. Compd.* **1995**, *216*, 159.
(19) Barkhordarian, G.; Klassen, T.; Bormann, R. *The journal of physical chemistry. B* **2006**, *110*, 11020.
(20) Tomkins, P. W. M. J. a. F. C. *Chemistry of the Solid State*; Butterworths: London, 1955.
(21) Avrami, M. *J Chem Phys* **1939**, *7*, 1103.
(22) Avrami, M. *The Journal of Chemical Physics* **1940**, *8*, 212.
(23) Avrami, M. *J Chem Phys* **1941**, *9*, 177.
(24) Malek, J.; Mitsuhashi, T. *J Am Ceram Soc* **2000**, *83*, 2103.
(25) Zhdanov, V. P. *Surf Rev Lett* **2008**, *15*, 605.
(26) Chung, C. J.; Nivargi, C.; Clemens, B. *Physical chemistry chemical physics : PCCP* **2015**, *17*, 28977.
(27) Fernandez, J. F.; Sanchez, C. R. *J. Alloy. Compd.* **2002**, *340*, 189.
(28) Barkhordarian, G.; Klassen, T.; Bormann, R. *Scripta Mater* **2003**, *49*, 213.
(29) Barkhordarian, G.; Klassen, T.; Bormann, R. *J. Alloy. Compd.* **2006**, *407*, 249.
(30) Li, W.; Li, C.; Ma, H.; Chen, J. *Journal of the American Chemical Society* **2007**, *129*, 6710.

(31) Liu, Y.; Zou, J.; Zeng, X.; Ding, W. *RSC Advances* **2015**, *5*, 7687.
(32) Zhou, C.; Fang, Z. Z.; Bowman, R. C. *The Journal of Physical Chemistry C* **2015**, *119*, 22261.
(33) Finney, E. E.; Finke, R. G. *Chemistry of Materials* **2009**, *21*, 4692.
(34) Watzky, M. A.; Finke, R. G. *Journal of the American Chemical Society* **1997**, *119*, 10382.
(35) Wakefield, B. J. In *Organomagnesium Methods in Organic Synthesis*; Academic Press: London, 1995, 21.
(36) Blach, T. P.; Gray, E. M. *Journal of Alloys and Compounds* **2007**, *446*, 692.
(37) Dill, E. D.; Folmer, J. C. W.; Martin, J. D. *Chemistry of Materials* **2013**, *25*, 3941.

CHAPTER 2: ACCESSING METASTABLE STRUCTURES UNDER MILD CONDITIONS: LOCAL AND EXTENDED STRUCTURE CHARACTERIZATION OF NANOCRYSTALLINE MAGNESIUM AND ITS HYDROGENATION KINETICS[2]

2.1 Overview

The kinetics of adsorption and desorption of hydrogen from magnesium hydride can be significantly enhanced via nanostructuring and catalyst addition. However, deconvolution of the mechanisms of enhancement due to these treatments remains elusive. Bottom-up solution synthesis of magnesium provides a facile route towards controlled nanostructuring and metal addition to the magnesium-based hydrogen storage system. In this work, we investigate perturbations in the local and extended structure of MgH_2 due to the addition of Ni. We find that the semi-reversible formation of metastable γ-MgH_2 is possible even with a minute amount Ni inclusion (<1.6 at. %) into the Mg NCs. This is correlated to dramatically enhanced hydrogen cycling capabilities for the Mg Ni composite. Furthermore, the presence of the Ni was found to result in a ~43% and ~21% decrease in the activation energy for desorption of hydrogen with respect to bulk MgH_2 and pure Mg NCs, respectively. In order to form a better understanding of the reasons for this enhancement, we use synchrotron radiation X-ray diffraction, X-ray absorption

[2] This chapter has been adapted by Max B. Braun from a manuscript to be submitted to the *Journal of Physical Chemistry C* with assistance in editing and direction provided by Amy L. Prieto. The XAFS studies were performed with the help of Steve Conradson, and the analysis of the experiments was adapted from the dissertation of Mary B. Martucci. Acquisition and analysis of the synchrotron X-ray data acquired at the Advanced Photon Source (APS) was performed by Max B. Braun, with the help of Joshua Kurzman and James Neilson. The SS NMR experiments were done at Revolution NMR, LLC, Fort Collins, CO by Matthew Nethercott. All other experiments and analyses, unless otherwise noted, were performed by Max B. Braun.

spectroscopy, solid-state nuclear magnetic resonance spectroscopy, and *in situ* pair distribution function analysis to fully characterize the local and extended structure of the Ni-doped nanocrystalline magnesium (hydride) system.

2.2. Introduction

Hydrogen is an attractive candidate as an alternative mobile fuel source due to its high-energy density, 153 kJ/mol H_2, approximately three times that of gasoline. Additionally, if hydrogen is sourced from water, then it has the potential for a clean, closed-loop production and consumption cycle.[1] With relatively high pressures (200 bar) or low temperature (-252 ºC) required for gaseous or liquefied hydrogen storage, one of the main challenges in hydrogen's implementation as a mobile energy carrier is its storage. Metal hydrides have been proposed as a potential solution, with magnesium hydride (7.6 wt %) presenting itself as a promising candidate that is light-weight, nontoxic, and earth-abundant. However, bulk magnesium hydride, following the reversible reaction:

$$\mathrm{Mg(s) + H_2(g) \leftrightarrows MgH_2(s)} \quad (1)$$

suffers from slow hydrogenation and dehydrogenation kinetics, and the reaction thermodynamics require high temperature (>400 °C) for hydrogen extraction and insertion.[2-7]

Compared to their bulk counterparts, nanostructured metal hydrides have dramatically improved hydrogenation and dehydrogenation reaction kinetics, even at lower temperatures.[3,4,8] However, theoretical calculations have suggested that significant alterations in the thermodynamics and binding environments of the magnesium hydride system only occur at particle sizes below ~5 nm.[9-11] Consequently, the effects that nanostructuring and particle size reduction have on magnesium hydride cycling behavior have received considerable investigation.

[9,12-19] Magnesium hydride usually takes on the rutile crystal structure, conventionally named β-MgH_2 (space group $P4_2/mnm$); however, it has recently been proposed that γ-MgH_2 (space group Pbcn), may be the reason for the increased kinetics of Mg hydrogen cycling.[20-23] The γ-MgH_2 phase is a metastable phase that has been observed to form in nanocrystalline MgH_2, usually under high temperature and pressure conditions.[23] The activation energy for desorption of hydrogen from the γ-MgH_2 phase has been both calculated and observed to be lower than that for β-MgH_2, which has been proposed to be the main reason for the increased dehydrogenation kinetics.[22,24,25] Unfortunately, γ-MgH_2 has never been made in excess of 30% (compared to β-MgH_2) , and fails to regenerate after a few hydrogenation/dehydrogenation cycles.[20]

Historically, producing nanocrystalline MgH_2 is most often achieved utilizing top-down methods (e.g., ball-milling).[2,5,6,17,26] Alternatively, bottom-up syntheses (e.g., solution-phase, arc-plasma reduction, electrochemical) of magnesium and magnesium hydride exhibit greater control over particle and crystallite size, which then allows for systematic evaluation of particle size effects on the hydrogen reaction kinetics and thermodynamics.[12,14,15,17,19,20,23,26-30] Of these methods, an adapted Rieke method for the solution phase synthesis of Mg nanoparticles provides a cheap, facile route towards understanding the role of size, catalyst addition, and encapsulation of reactive magnesium nanoparticles.[15,28-32]

Previously, we reported on the effects of particle size on the hydrogenation reaction kinetics of magnesium nanoparticles synthesized via an adapted Rieke method. We observed smaller particles reacting with hydrogen at increased rates, with the smallest particles (~25 nm) achieving 95% of the maximum hydrogen capacity within 60 s at 300 °C.[15] Additionally, Liu *et al.* have reported their initial investigation on magnesium nanocomposites synthesized via a similar adapted Rieke method with Co, Fe, Ni, Ti, or V as a dopant metal.[28,29,32] These reports, as well as

others, find that the addition of many secondary metals (e.g Ce, Co, Cu, Cr, Fe, Mn, Nb, Ni, Ti, V) and occasionally their oxides, can be a means to enhance the reaction (eq. 1) kinetics and/or thermodynamics.[5,6,9,26,33-45]

Importantly, Fernandez *et al.* found that the addition of MgO to MgH_2 during ball milling has also shown kinetic enhancement in the hydrogenation reaction.[18] This result seems counterintuitive, as oxygen exposure to the magnesium hydride creates a passivating layer that inhibits and can even halt the hydrogenation reactions. However, the authors suggest that the introduction of MgO during ball milling introduces a tribological effect that allows for a larger degree of crystallite size reduction, producing a MgH_2 material that has kinetics comparable to that of one of the leading "catalyzed" systems, MgH_2 with Nb_2O_5.[18] This further confirms the dramatic role that crystallite size has on the hydrogenation kinetics, and exemplifies the importance of maintaining control over crystallite size when attempting to elucidate the role of secondary metal addition on reaction (1).

While varying levels of kinetic and thermodynamic improvement have been observed for the different additives and synthetic approaches, an outstandingly superior composite system that meets all hydrogen storage goals has yet to be designed.[5] Theoretical calculations suggest that the enhancement capabilities of the added species are heavily dependent on the local electronic and coordination structure within the composite system.[9,16,44,46-50] However, systematic experimental investigations into the perturbations on the local structures within these systems are limited.[12,38,41,50] In order to effectively design materials with exceptional kinetic and thermodynamic properties towards the de/hydrogenation reactions, it is necessary to understand these local structure perturbations, in addition to extended structure alterations, that occur with the addition of secondary metals.[50,51]

Of the secondary metal additives that have been investigated thus far, Ni is a promising candidate that not only improves the kinetic properties of the magnesium hydride reactions, but has also been suggested to improve the thermodynamic properties.[26,29,52,53] Due to its promising characteristics, it is an ideal candidate for the systematic investigation of its role and effects in the de/hydrogenation reactions. Herein, we report the use of multiple local and extended structure characterization techniques to investigate a Mg-Ni nanocomposite synthesized by an adapted Rieke method. Using the combination of high energy X-ray diffraction (XRD), X-ray absorption near-edge spectroscopy (XANES), extended X-ray absorption fine structure spectroscopy (EXAFS), magical angle spinning (MAS) ^{2}H solid-state nuclear magnetic resonance spectroscopy (SS-NMR) we attempt to uncover the subtle perturbations introduced by the Ni additive that lead to dramatically enhanced dehydrogenation kinetics in the nanoscale magnesium hydride system.

2.3 Experimental

2.3.1 Synthesis of Nanoparticles

All syntheses and instrument preparation steps were done in nitrogen glovebox or using Schlenk technique to limit oxidation of samples. Oxygen and water levels were kept below 0.1ppm. The magnesium precursor, magnesocene ($MgCp_2$), was synthesized by the slow addition of freshly cracked cyclopentadiene to a stoichiometric amount of *n*-butyl-*sec*-butyl magnesium (0.7 M in heptane Sigma-Aldrich) under stirring, according to previous literature procedure.[54] The resulting white/yellow powder was washed with cold hexanes, and then purified by sublimation giving a white, crystalline powder.

In preparation for the magnesium particle synthesis, 1,2-dimethoxy ethane (glyme, Sigma-Aldrich, anhydrous, 99.99%) was refluxed over phenanthrene (Sigma-Aldrich 98%) and

potassium (Sigma-Aldrich 99.5%) for >6 hours before distillation. From here, a reducing solution of potassium (0.5 M), phenanthrene (0.5 mM), and freshly distilled glyme were stirred for two hours to provide a dark green solution. A separate solution of freshly distilled glyme and magnesocene (0.05 M) was heated to 70 ºC under vigorous stirring, resulting in a clear to light tan/yellow solution. The reducing solution was rapidly added to the magnesocene solution, resulting in a dark green/black suspension that was allowed to stir for 30 minutes.

The resulting particles were collected via centrifugation, followed by a wash with 3 mL of distilled glyme. This solution was then centrifuged and the green supernatant was discarded. This process was repeated at least 3 times or until the supernatant was clear. The resulting particles were then dried by vacuum for at least 3 hours producing a black-greyish powder.

For nickel doping, nickelocene ($NiCp_2$, Strem Chemicals, 99%) and glyme were mixed to provide a turquoise solution (0.01 M) with 1, 5, and 10 wt % Ni compared to Mg. This solution was added dropwise ~1 minute after the reducing solution was added to the magnesocene solution. The resulting solution was then allowed to stir for 30 minutes after complete addition of the nickelocene. The Ni doped particles were then subjected to the same washing and drying procedure as the pure Mg particles. For ease of discussion and presentation, we refer to these samples by the amount added during synthesis (e.g., Mg-5Ni is 5 wt.% Ni added).

2.3.2 Characterization

In-house XRD was performed with a Bruker D-8 DaVinci diffractometer installed with Cu Kα X-ray source (λ = 1.5418Å) at 40kV and 40mA. Samples were covered with either polyimide tape or mineral oil to prevent oxidation during measurements. The elemental composition of the as-synthesized particles was measured with energy dispersive X-ray spectroscopy (EDS) on a

JEOL JSM-6500F field-emission scanning electron microscope (FESEM) equipped with an X-max 80 from Oxford Instruments. The particle morphology and size was analyzed by imaging with both a JEOL JEM-2100F 200 kV transmission electron microscope (TEM) and JEOL JEM-1400 120 kV TEM. Scanning transmission electron microscopy (STEM)-EDS mapping was also performed to map the location of the Ni using the JEOL JEM-2100F TEM equipped with an X-Max^N 80 T. Thermogravimetric analysis (TGA) was performed under N_2 flow on a TA TGA Q500 Thermogravimetric analyzer.

X-ray absorption near-edge spectroscopy (XANES) and extended X-ray absorption fine structure (EXAFS) data was taken at the Stanford Synchrotron Radiation Lightsource (SSRL). Three samples were prepared for X-ray absorption measurements: the first was 1 wt % Ni-doped Mg (sample 125); the second was 5 wt % Ni-doped Mg (sample 127); and the third was 10 wt % Ni-doped Mg (sample 151). All three samples were hydrogenated and dehydrogenated once prior to analysis. Then, half of each sample was separated out and hydrogenated again, to create three additional hydride samples for analysis: 125h, 127h and 151h, respectively. X-ray measurements were performed and the data analyzed by previously reported procedures.[55]

Synchrotron radiation *ex situ* powder XRD (SR-XRD), as well as *ex situ* and *in situ* X-ray total scattering (for pair distribution function (PDF) analysis) was performed at the Advanced Photon Source (APS), beamline 11-ID-B (λ = 0.2114Å) located at Argonne national lab. Samples were sealed under argon in quartz capillary tubes post-synthesis to prevent oxidation. *Ex situ* samples were flame-sealed on both ends and patterns were collected for 5-20min. The crystallite size of as-synthesized and hydride particles was calculated using the Scherrer equation on peaks corresponding to the (110), (101), and (200) planes for β-MgH_2, and (100), (002), and (101) planes for Mg.[56] *In situ* total scattering samples were loaded into 1mm quartz flow tubes packed with

glass wool on either side of sample. The flow cell with thermocouple was assembled and sealed inside a nitrogen glove box with water and oxygen levels below 1ppm.[51] Resistive heaters with ceramic furnaces connected to a thermocouple inside the flow cell were used for temperature control of the samples. This flow cell was mounted in the beamline for electron total scattering measurements taken every two minutes. The temperature for these samples was ramped between 5 ºC/min and 10 ºC/min to a final temperature of 270-350 ºC. All diffraction images collected from APS was converted into 1D patterns using Fit2D software. PDF analysis was done with PDFgetX3, and fitting was performed with PDFGUI. All full profile Rietveld refinements were done with GSAS and EXPGUI.

Hydrogen (deuterium) cycling was performed in-house with a home built pressure-composition-temperature (PCT) Sievert-type apparatus. The as-synthesized particles were hydrogenated at 9.0-9.5 bar hydrogen pressure at 300 ºC for 15-30 minutes. The samples were dehydrogenated at 0.5-1.3 bar and 350 ºC for 45-60 minutes.

MAS ^{2}H SSNMR experiments were performed on Ni doped (5 and 10 wt.%) and un-doped Mg samples that were deuterated at 300 ºC. The experiments were carried out on a Bruker Advance I spectrometer (Bruker, Billerica, MA) operating at 61.35 MHz for ^{2}H, 100.51 MHz for ^{13}C, and 399.67 MHz for ^{1}H running the Topspin 2.1® software package from Bruker. An HX probe (Revolution NMR, LLC, Fort Collins, CO) equipped with a 4 mm Kel-F spinning module (Revolution NMR, LLC, Fort Collins, CO) was used to acquire the ^{2}H spectra. Each sample was packed into a 4 mm zirconia rotor inside a glovebox under N_2 atmosphere. The rotors were sealed

using Kel-F endcaps with grooves for o-rings (Revolution NMR, LLC, Fort Collins, CO) and Vespel^{TM} drive tips.

The probe was setup and optimized in carbon mode first using 3-methylglutaric acid, confirming the probe was operational, and the magic angle was properly set. The methyl peak of the ^{13}C spectrum was referenced to 18.84 ppm.[57] The probe tuning was changed to observe ^{2}H, and the probe was setup and optimized using (3-TMS Proponoic Acid sodium salt – d4). ^{2}H chemical shifts are reported relative to (3-TMS Proponoic Acid sodium salt – d4), which was set to 0 ppm. Magic angle spinning speeds were typically 8 – 15 kHz for isotropic shift and spinning sideband identification. The shifts are reported with an accuracy of ±0.4 ppm. The ^{2}H T_1 relaxation times were measured using the saturation recovery experiment, and initially determined in the Topspin 2.1 "t1guide" macro. The pulse sequence is: $(\pi/2) - \tau - (\pi/2)$ – acquisition – pulse delay, and τ is the variable delay. Four scans per t1 point were acquired. For ^{2}H spectra, a one-pulse sequence was used: $(\pi/2)$ – acquire – pulse delay. The $(\pi/2)$ pulse was ~100 kHz, spectral width was ~100 kHz (~1630 ppm), pulse delay was typically 1.3 – 2x the ^{2}H T_1 value, 3994 points (~20 ms acquisition time) and the spectra are the result of ~12 hours of signal averaging. The ^{2}H transmitter was set at ~21 ppm. The data was processed with 50 Hz of line broadening, phased, and baseline corrected. Spectral fitting was performed on Topspin 2.1, using the QuadALL model to derive the quadrupole coupling constant and quadrupole asymmetry parameters.

2.4 Results and Discussion:

2.4.1 Microstructural Characterization and Hydrogen Absorption Kinetics:

The as-synthesized magnesium nanoparticles (with and without nickel additive) were confirmed to be crystalline via characterization by synchrotron radiation X-ray diffraction (SR-

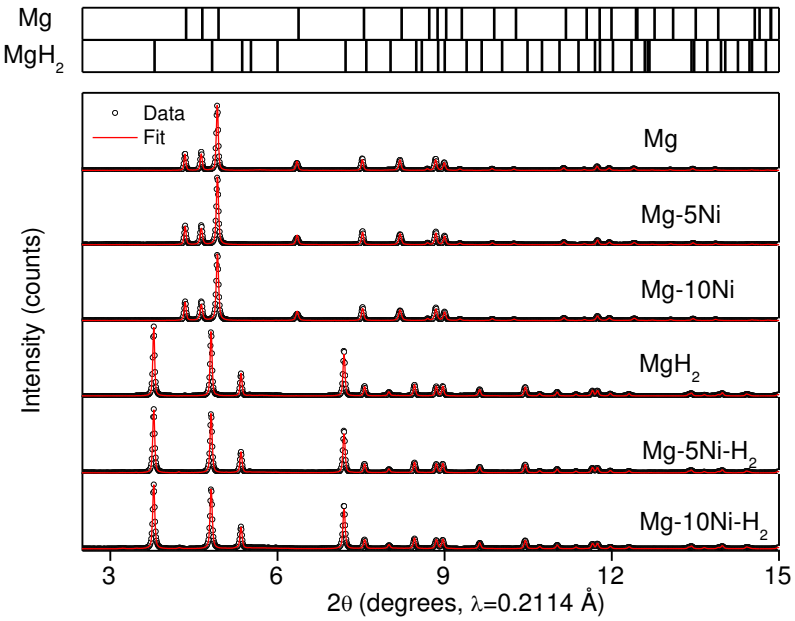

Figure 2.1. SR-PXRD patterns and Rietveld refinements for the as-made particles, and the resulting particles after hydrogenation at 300°C

XRD, Figure 2.1). The major phase in the diffraction data fit well to hcp magnesium (space group $P6_3/mmc$) with $a=b=3.2218(3)$ Å and $c=5.2301(1)$ Å for the as-prepared magnesium nanoparticles. This is slightly larger than the lattice parameters for the Mg particles with Ni addition, which refined to $a=b=3.22006(4)$ Å and $c=5.2290(1)$ Å, and $a=b=3.21994(5)$ Å and c=5.2285(2) Å for Mg-5Ni and Mg-10Ni, respectively. This small reduction in lattice spacing could be due to the substitution of Ni, which is slightly smaller than Mg, into the lattice of Mg. Interestingly, this is in contrast to the results obtained by Liu *et al.*, where they found a slight increase (~0.8%) in unit cell volume with the addition of Ni. They suggest that the Ni incorporation (7.8 wt % by EDS), or perhaps Ni nucleation sites during the co-precipitation synthesis, may have led to their observed decrease in crystallite size (27.9%).[29] In contrast, Ni is added after the initial precipitation of the Mg in our syntheses, and the small difference in lattice volume (~0.1%) did not lead much of a difference in crystallite size, as the Scherrer equation indicated crystallite size

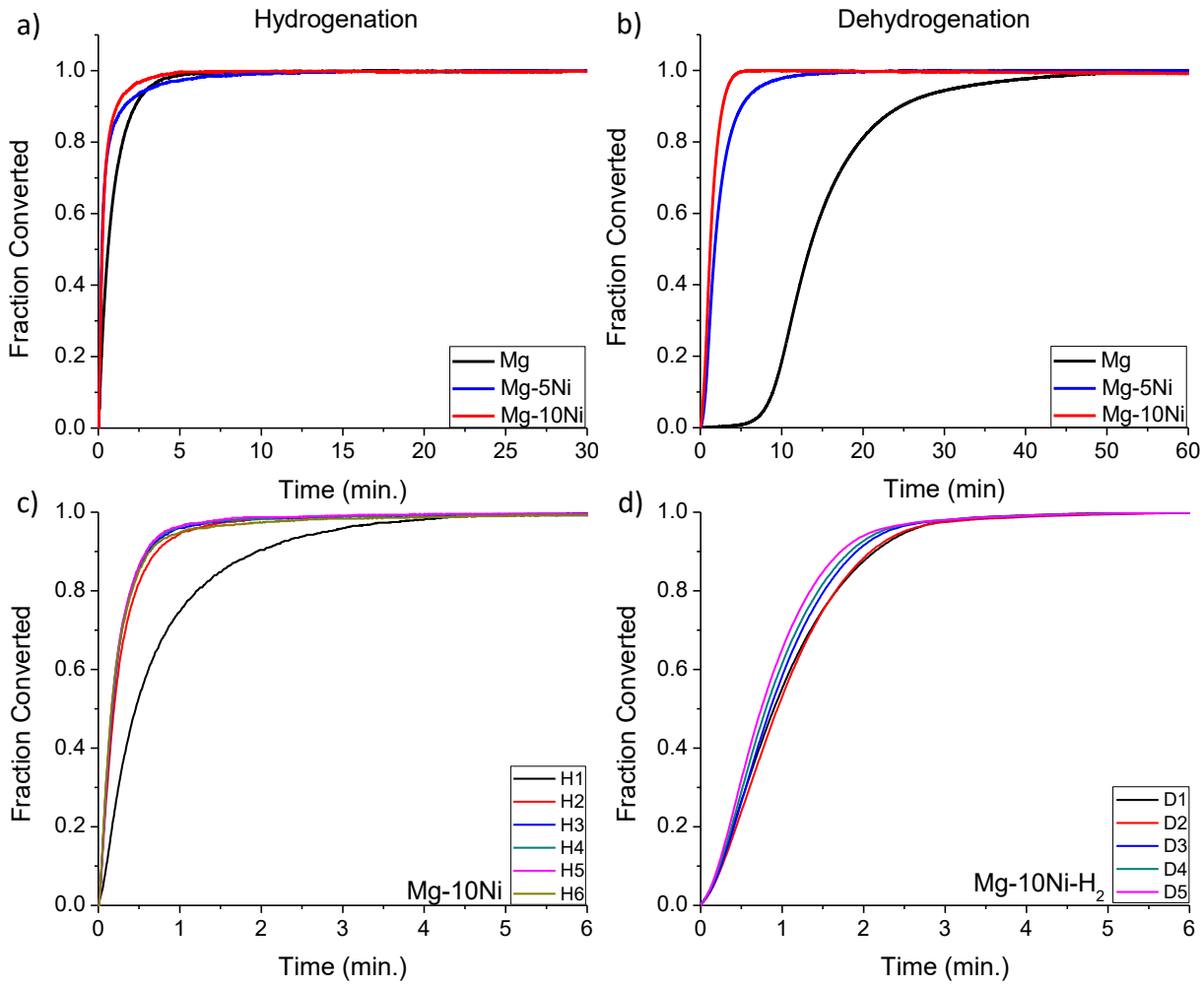

Figure 2.2. (a) Calculated fraction of magnesium converted to the hydride at 300 °C vs. time for typical as-synthesized Mg, Mg-5Ni, and Mg-10Ni samples. (b) Calculated fraction of magnesium hydride converted to magnesium at 350 °C vs. time for the hydrogenated forms of the same samples. Additional (c) hydrogenation and (d) dehydrogenation cycles for the Mg-10Ni sample. The fraction converted was calculated using the ideal gas law based on the pressure drop (increase) during hydrogenation (dehydrogenation).

of ~25-27 nm for all of the as-made particles. This size assignment was tentatively verified by TEM (Figure S2.1); however, the particles are agglomerated and some are heavily oxidized from loading to the TEM, leaving the actual particle and crystallite size difficult to discern.

Figure 2.2a displays that at 300 °C the as-synthesized pure Mg particles hydrogenate at a comparable rate with respect to the Mg-5Ni and Mg-10Ni samples. However, it is worth noting

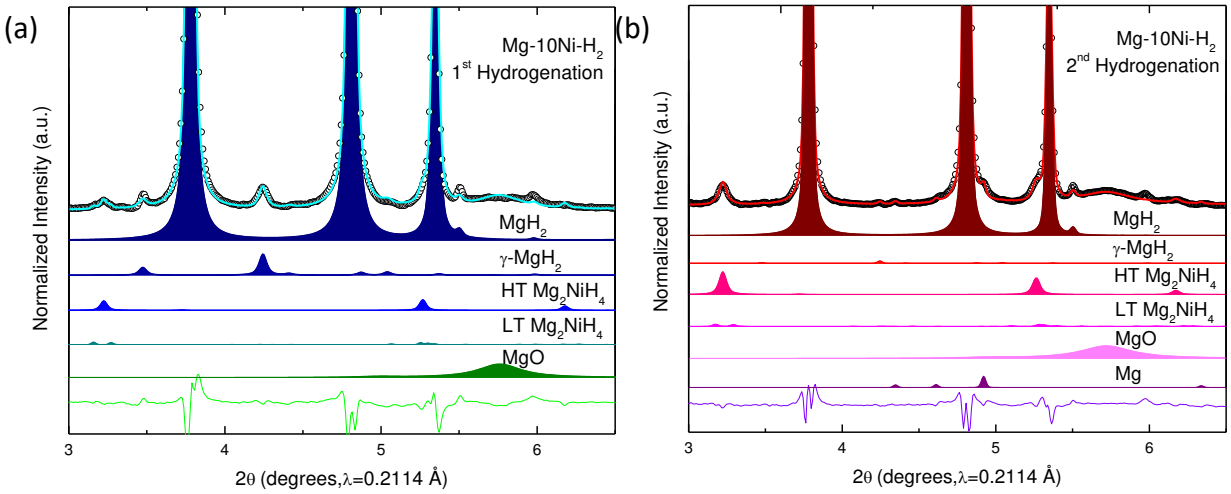

Figure 2.3. Phase-decomposed contributions to fittings from Rietveld refinement of the *ex situ* SR-XRD patterns for the (a) first and (b) second hydrogenation (performed at 300 °C) of a Mg-10Ni sample.

that the doped samples are able to absorb 80% of their total hydrogen capacity in ~1/3 of the time. The Mg, Mg-5Ni, and Mg-10Ni samples are able to absorb ~6.6(2), 6.4(3), and 6.2(2) wt.% H_2, respectively. After hydrogenation, the major phase present for the converted un-doped particles fits well to β-MgH_2 with a=b=4.53145(5) and c=3.03009(5). Similarly, the Mg-5Ni and Mg-10Ni also convert to β-MgH_2 with a=b=4.53173(5) and c=3.02995(5), and a=b=4.53136(6) and c=3.02943(6), respectively (Figure 2.1). This corresponds to only a few hundredths of a percent difference in unit cell volume, suggesting a lack of unit cell size effect due to Ni in the periodic extended structure of the doped β-MgH_2. Interestingly, however, the Ni-doped samples have the ability to desorb hydrogen in around a 10^{th} of the time that it takes the pure Mg sample to dehydrogenate. Moreover, the kinetics of de/hydrogenation for the Mg-10-Ni samples increase after successive cycles (Figure 2.2c-d), and the capacity is mostly retained (decreasing by only ~4% in 5 cycles). In contrast, the pure Mg particles degrade in both hydrogen capacity (desorbing ~26% less) performance after 3 cycles (Figure S2.2). In order to understand these dramatic differences in de/hydrogenation kinetics, we further investigated the SR-XRD results.

Evidently, there are additional low intensity peaks that are exhibited upon hydrogenation of the Mg-5Ni and Mg-10Ni samples. In Figure 2.3, the decomposed refined contributions from the secondary phases are plotted at low 2θ (where the reflections are most significant) for the Mg-10Ni sample after both the first, and second hydrogenation at 300 °C. Furthermore, similar plots for a partially dehydrogenated Mg-10Ni sample (after second hydrogenation), fully hydrogenated Mg-5Ni sample (cycles one and two), and a partially dehydrogenated Mg-5Ni sample can be found in Figures S2.3, S2.4. The weight percentages of the different secondary phases are summarized in Table 2.1, and unfortunately, magnesium oxide appears to be one of the major secondary phases that is exhibited. This is probably due to adventitious oxidation during sample preparation.

However, as indicated in Table 2.1, there are other secondary phases, including γ-MgH_2, that likely contribute to the observed improvement in de/hydrogenation kinetics (Figure 2.2b).

As mentioned in the introduction, the role of γ-MgH_2 in the cycling abilities of nanostructured magnesium hydride has recently been investigated via both theoretical and experimental studies.[20,22-25] Due to the slightly larger Mg-H bond lengths that occur in γ-MgH_2, the MgH_6 octahedra are much more distorted than those in β-MgH_2.[24,25] This distorted structure leads to a lower (calculated and observed) activation energy for hydrogen desorption.[20,23,24] The existence of this metastable γ-MgH_2 phase in our hydrogenated Mg-5Ni and Mg-10Ni samples, likely contributes to the increased desorption kinetics we observe for these samples (Figure 2.2).

Also of significance, is the presence of γ-MgH_2 in our samples after a second hydrogenation at 300 °C. Previously, it has been suggested that successive hydrogenation at 300 °C would result

Table 2.1: Phase-structure contributions of Mg based nanocomposites from Rietveld refinements of *ex situ* SR-XRD data at various hydrogen cycling stages

	1st Hydrogenation	2nd Hydrogenation	Partial Dehydrogenation

Material	Phase	Space group		Abundance (wt %)	
Mg-5Ni: Hydrogenations at 300°C; dehydrogenations at 350°C; Partial dehydrogenation after second hydrogenation	β-MgH_2	*$P4_2/mnm$*	92.01(1)	83.59(2)	77.37(4)
	γ-MgH_2	*Pbcn*	0.7(1)	0.9(3)	2.47(2)
	HT-Mg_2NiH_4	*$Fm\bar{3}m$*	0.10(4)	0.25(6)	0.23(5)
	LT-Mg_2NiH_4	*C12/c1*	0.02(9)	0.1(1)	0.1(1)
	$Mg_2NiH_{0.3}$	*P6222*	-	-	0.38(5)
	MgO	*$Fm\bar{3}m$*	7.1(3)	14.5(3)	12.0(3)
	Mg	*$P6_3/mmc$*	-	0.65(8)	7.35(9)
Mg-10Ni: Hydrogenations at 300°C; dehydrogenations at 350°C; Partial dehydrogenation after second hydrogenation	β-MgH_2	*$P4_2/mnm$*	87.85(1)	86.14(2)	66.38(4)
	γ-MgH_2	*Pbcn*	5.4(5)	0.1(1)	0.2(1)
	HT-Mg_2NiH_4	*$Fm\bar{3}m$*	0.44(6)	2.5(2)	0.61(8)
	LT-Mg_2NiH_4	*C12/c1*	0.13(8)	0.1(1)	0.13(9)
	$Mg_2NiH_{0.3}$	*P6222*	-	-	0.37(5)
	MgO	*$Fm\bar{3}m$*	6.1(3)	10.5(3)	16.3(3)
	Mg	*$P6_3/mmc$*	-	0.55(8)	16.00(7)

in the disappearance of the metastable γ-MgH_2 due to the higher temperatures annealing any defects and strain that caused the MgH_2 to take on this distorted crystal structure.[23] In our samples however, the γ-MgH_2 persists through the second hydrogenation. Furthermore, in the partially dehydrogenated Mg-5Ni sample, we see the reappearance of the γ-MgH_2 phase, in even greater amount than that in the fully hydrogenated sample (Table 2.1). The increase in wt % γ-MgH_2 could be due to a necessity for structural rearrangement or distortion in order to relieve strain or disorder upon pausing of the desorption reaction. In contrast, for the partially dehydrogenated Mg-10-Ni sample, the reappearance of the γ-MgH_2 is not necessarily to the same extent, perhaps because the desorption reaction was further along when this sample was made. Nevertheless, this formation and regeneration of γ-MgH_2 after hydrogen cycling has only been observed by Shen *et al.*, who synthesized nanoscale Mg via an electrosynthesis with Ni as a sacrificial electrode.[20] They found that upon hydrogen cycling, the γ-MgH_2 was reformed for up to 5 successive cycles (desorption at 200 °C, adsorption at 100 °C), after which it is no longer exhibited. They hypothesize that under successive structural reorganizations during hydrogen cycling, the nanocrystals begin to anneal and release defects and strain, which ultimately leads to

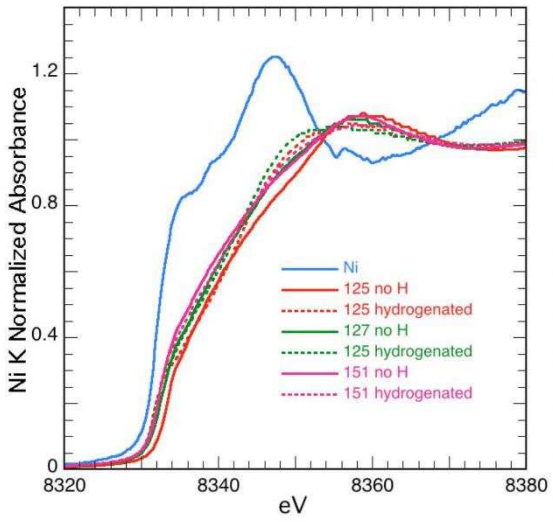

Figure 2.4. Ni K edge XANES spectra for both the hydrogenated and dehydrogenated forms of a Mg-1Ni (125), Mg-5Ni (127), and a Mg-10Ni (151) sample.

a lack of γ-MgH_2 reformation.[20] Nonetheless, the ability to stabilize and regenerate γ-MgH_2 is noteworthy. This capability is evidently also displayed in our system, and it is likely due to the similarities in syntheses (low-temperature, bottom-up synthesis of Mg with Ni presence). Low temperature syntheses are more likely to lead to defects, which could result in a strained lattice that facilitates the distorted γ-MgH_2 phase formation. Furthermore, the presence of the additional metal, Ni, could also contribute to a strained or distorted lattice.[15,29] Although Shen *et al*. propose that there is little or no Ni-Mg alloying that occurs in their system, they do concede that it likely has an effect on the hydrogenation kinetics. In contrast, the results from our Rietveld refinements (Table 2.1) indicate that there is noticeable Mg-Ni alloying occurring in our system.

Of the different Mg-Ni-H structures present in our samples, the high temperature Mg_2NiH_4 (HT-Mg_2NiH_4) phase exists in the largest abundance. The transition from the cubic high temperature phase to the monoclinic low temperature phase occurs at ~235 °C. The calculated abundance of the LT-Mg_2NiH_4 is nearing statistical insignificance; however, seeing that the diffraction was taken at room temperature, and the data is qualitatively fit better it was worth

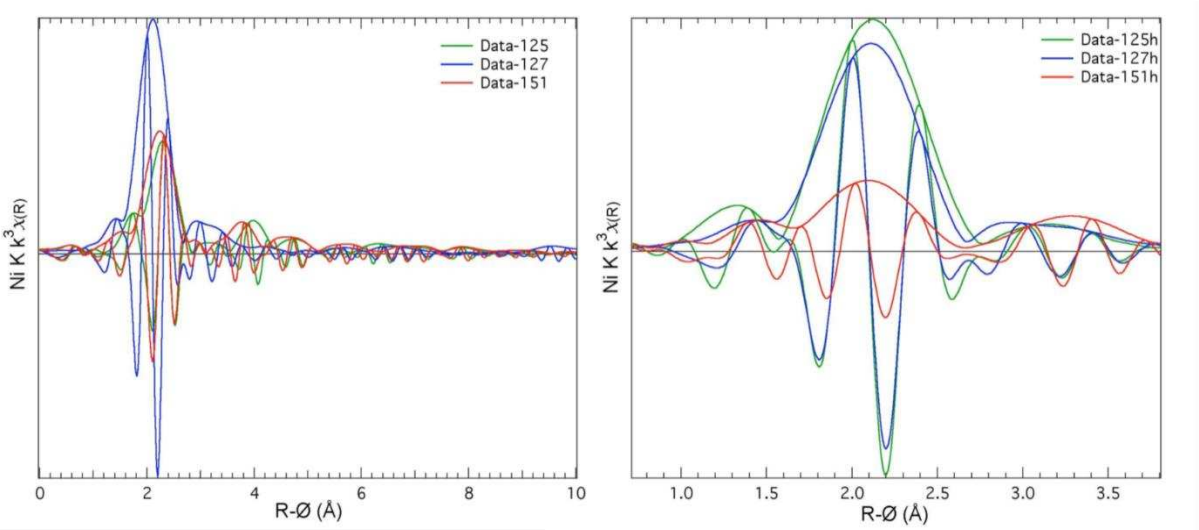

Figure 2.5. Ni EXAFS spectra and Fourier transform for the (a) hydrogenated and (b) dehydrogenated forms of Mg-1Ni (125), Mg-5Ni (127), and Mg-10Ni (151) samples.

considering it in our analyses (Figure S2.3). Nonetheless, it has been well established that both the low and high temperature Mg_2NiH_4 phases have comparatively better hydrogen adsorption/desorption kinetics and thermodynamics with respect to MgH_2.[58-60] Consequently, when investigated as secondary phases in MgH_2, these phases can act as nucleation catalysts for hydrogen desorption.[21,29,61] Denys *et al.* showed that the HT-Mg_2NiH_4 decomposed into $Mg_2NiH_{0.3}$ at temperatures as low as 100 °C under vacuum.[21] Similarly, in the diffraction patterns of our partially dehydrogenated samples (Figure S2.3 and S2.4), low intensity reflections corresponding to $Mg_2NiH_{0.3}$ are present. This result supports the assignment of the HT-Mg_2NiH_4 in our fully hydrogenated samples.

2.4.2 Local Structure Characterization:

In our SR-XRD studies, the wt % Ni from these phases (Table S2.1) still does not fully account for the weight % Ni given in the compositional analysis via SEM-EDS (~2.5 and 3.5 wt % Ni for Mg-5Ni and Mg-10Ni, respectively). Furthermore, elemental mapping done while performing scanning transmission electron microscopy (STEM) does not indicate noticeable

heterogeneous, agglomeration of Ni (Figure S2.5). The Ni appears to be randomly dispersed throughout both the metallic and hydrogenated samples. In order to investigate the structure of the Ni that is not represented in the extended structure analysis (i.e., SR-XRD), we chose to utilize X-ray absorption spectroscopy (XAS) which is an element specific technique that can provide valuable details on the local structure of dopant metals and metal oxides in metal hydrides. [38,41,62,63]

The Ni K edge X-ray absorption near edge spectra (XANES) for the hydrogenated and dehydrogenated configurations of a Mg-1Ni (125), Mg-5Ni (127), and a Mg-10Ni (151) sample are displayed in Figure 2.4. Compared to a Ni metal standard the absorption edges of each of the samples (both hydrogenated and dehydrogenated) are shifted towards higher energy, signifying a lower valence of the metal in the samples. Additionally, the spectra for both the hydrogenated and dehydrogenated samples are broad and lacking any distinct features, suggesting a disordered structure. The Ni K-edge extended X-ray absorption fine structure (EXAFS, $\chi(R)*k^3$) spectra for the dehydrogenated samples also indicate a disordered environment around the Ni dopant (Figure 2.5a). The most obvious indication of the disordered structures surrounding Ni in the dehydrogenated samples is the difference in the extended (i.e., R>2.5 Å) spectra from sample to sample. Furthermore, the real component of the primary nearest neighbor for samples 125 and 151 is the peak around R=2.26-2.29 Å, just past the modulus peak. This is in contrast to metallic Ni, which has the real component of the nearest neighbor around 2.15 Å, just before the modulus peak.[64] This suggests that the nearest neighbor is not just Ni. Indeed, this is further supported in the fitting of the EXAFS data for each sample (Figures S2.6-S2.8), and the results of the fitting of the individual spectra are summarized in Table S2.2. As with the direct comparison of the spectra

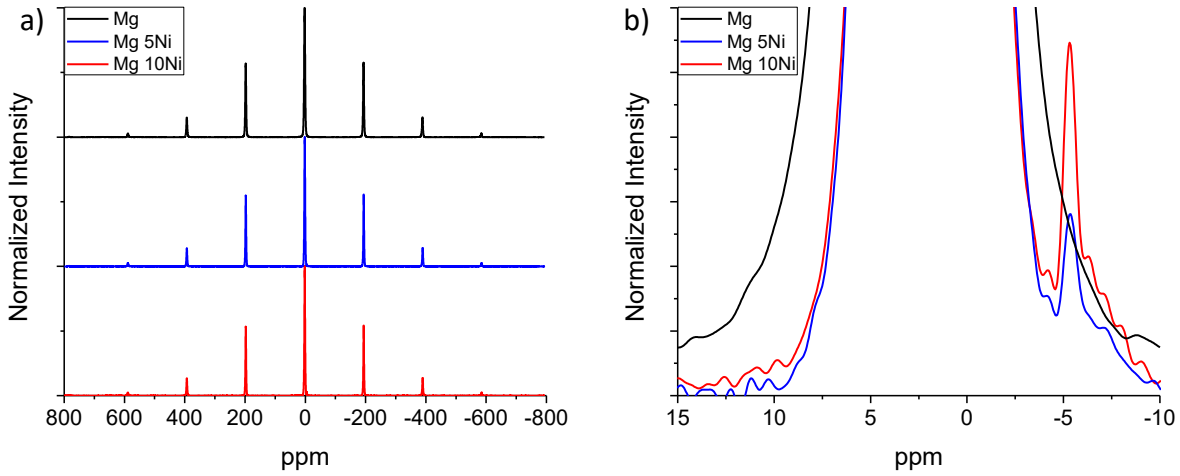

Figure 2.6. (a) Full and (b) zoomed in spectrum of ^{2}H NMR for the deuterated form of Mg, Mg-5Ni, and Mg-10Ni.

(Figure 2.5a), the fitted data indicate that not only is the nearest neighbor likely Mg (and not Ni), the medium-range order (i.e., R>2.5 Å) is fit significantly different for each sample. This leads us to the conclusion that altering the Ni metal loading on a sample has a dramatic effect on the metal's local, apparently complicated, environment. Moreover, as mentioned in the methods section, these samples were hydrogen cycled once prior to EXAFS analysis. This result is especially important in the light of our SR-XRD results. The retention or reformation of the structural disorder around the Ni, even post activation (i.e., after the first hydrogen cycle), could contribute to the observed reformation of the γ-MgH_2 during cycling.[29] It is also possible that the disordered Ni environment catalyzes the adsorption of hydrogen, and if this disorder is persisting through many cycles, could be the reason for the enhanced reaction kinetics after multiple hydrogenation cycles.[65]

Interestingly, upon hydrogenation of all three samples, the real component of the nearest neighbor is just below the modulus peak, suggesting a nearest neighbor of Ni (Figure 2.5b). This conclusion is supported by the fitted data for each of the samples (Figures S2.9-2.11). As summarized in Table S2.2, the nearest Ni neighbor in the hydrogenated samples is fit well with Ni

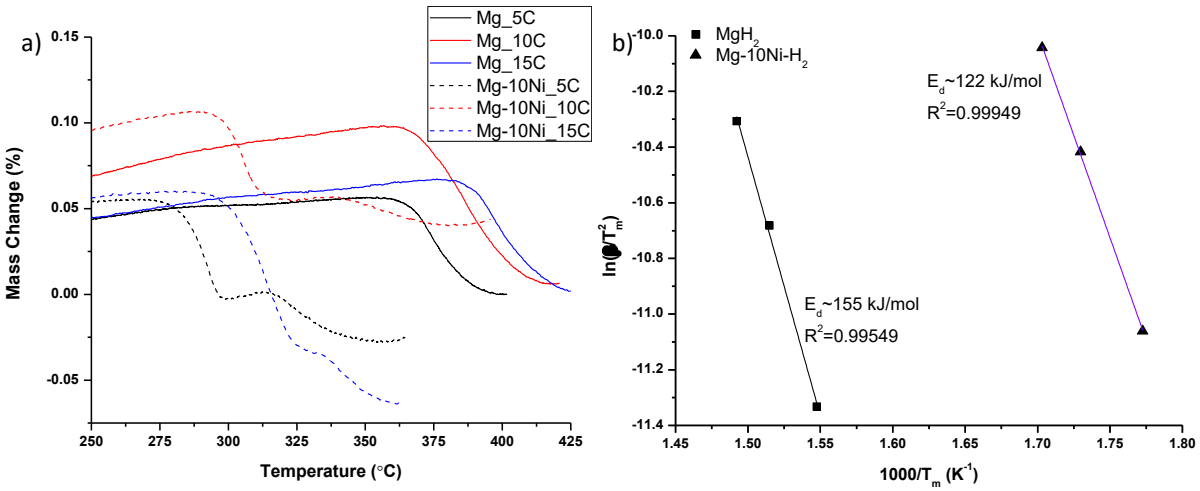

Figure 2.7. (a) TGA profile for hydrogenated Mg (solid traces) and Mg-10Ni (dashed traces) at 3 different ramp rates (5, 10, and 15 °C/min) (b) Kissinger plot for pure MgH_2

at around 2.47 Å. This suggests the existence of Ni-Ni metal bonds (generally around 2.492 Å) in the hydrogenated samples. Due to the lack of Ni metal reflections in the SR-XRD patterns, and the lack of continuous Ni-Ni order beyond 2.47 Å (in these EXAFS spectra), the formation of these Ni-Ni bonds is highly aperiodic, unsaturated, and most likely consists of very few atoms. Again, when comparing the extended local structure with varying Ni loadings, there are still significant differences in both the distance and identification of neighbors (Figure 2.5b, Table S2.2). For the case of the hydrogenated samples, the extended local structure of the Ni in the highest percent loading Mg-10Ni-H_2 (151h) deviates significantly from the other samples (Figure S2.11). Overall, the EXAFS of both the hydrogenated and dehydrogenated samples with various Ni loadings support the conclusion that the majority of the Ni in these samples has an extended local structure that is highly disordered. Again, due to the fact that these samples were cycled once prior to analysis, the Ni is likely migrating between environments that drive it to preferably bond with other Ni atoms, to those that drive bonds with Mg. Although this migration in between disordered

local environments is seemingly reversible, our SR-XRD results suggest that the some of the Ni will occasionally relax into more periodic environments (e.g., Mg_2NiH_4).

To get an idea of how these numerous and evidently variable Ni environments are affecting the local structure of the hydrogen, we used magic angle spinning solid-state nuclear magnetic resonance (MAS SS NMR). SS NMR is a powerful, element-specific tool that can provide insight into perturbations on the bulk behavior and mobility of the element of interest. Recently, SS NMR has been heavily utilized as a complementary structural characterization tool in metal hydride systems.[12,33,50,66-73] We chose to perform ^2H NMR because deuterium does not have the dipolar coupling exhibited in hydrogen, and thus can more easily afford higher resolution spectra.[33] The ^2H NMR spectra for the deuterated samples are displayed in Figure 2.6.

At first glance, the full spectra for the doped samples are almost identical to that in pure MgD_2 (Figure 2.6a). The spinning side band pattern for the ^2H NMR spectra of magnesium deuteride can be described by a quadrupole coupling constant of 37 kHz and a quadrupole asymmetry parameter η=0.8. In comparison, the spinning side band pattern for the doped samples can be well described with a quadrupole coupling constant of 36 kHz, and quadrupole asymmetry parameters of η=0.85 and η=0.83 for the Mg-5Ni-D_2 and Mg-10Ni-D_2, respectively. The small decrease as in the quadrupole coupling constant, and in the height of the spinning side bands (~4 and 6% for the Mg-5Ni-D_2 and Mg-10Ni-D_2, respectively), suggests that the deuterium has a coordination geometry that would result in smaller electric field gradient. This has been observed for other titanium and scandium containing magnesium deuterides.[33,50,70,74] Moreover, the spectra of the doped samples exhibit a small additional peak centered around -5.3 ppm. This peak's integrated intensity grows when comparing the Mg-5Ni sample to the Mg-10Ni sample, from a ratio of 100:0.34 to 100:0.66 relative to the center peak. This suggests that the peak's appearance

is related to the introduction of Ni. The negative shift of this peak, about 7.26 ppm more negative than the bulk peak, is consistent with the chemical shift that has been observed for nickel containing Mg hydride/deuteride species.[33,72]

Another key difference in the spectra lies in their spin-lattice relaxation parameter, T_1. The T_1 of the main peak was found to be 310.7 ± 8.2 seconds for the pure MgD_2. In comparison, the T_1 values were found to be 99.6 ± 4.5 seconds and 93.6 ± 4.1 seconds for the Mg-5Ni-D_2 and Mg-10Ni-D_2, respectively. The Ni-doped samples have an altered spin lattice relaxation mechanism. This difference is likely due to the disorder introduced with the addition of Ni (as concluded above), as well as increased dynamics of the deuterium within the lattice.[74] Alternatively, the shorter T_1 can be the result of the presence of paramagnetic impurities (e.g., Ni) within the sample.[68] Regardless, the change in T_1 for this main peak leads us to conclude that the introduction of Ni is clearly altering the local environment of the deuterium in the bulk of the sample, which is reflected in the kinetics data. Furthermore, the T_1's of the secondary peaks (centered around -5 ppm), were found to be 4 orders of magnitude shorter, 8.0 ± 1.6 and 5.8 ± 1.4 milliseconds for the Mg-5Ni-D_2 and Mg-10Ni-D_2 samples, respectively. This is consistent with the T_1's for deuterium in near a paramagnetic element.[68] These sites could serve as initiators for hydrogen/deuterium vacancy formation, which would result in increased deuterium/hydrogen diffusion and a decreased activation energy for desorption.[24,49,75] This conclusion gives insight into the dramatically increased desorption kinetics exhibited in our Ni doped samples.

The interpretation of the ^2H NMR data was supported by the determination of the activation energy for desorption via thermogravimetric analysis (TGA) of the hydrogenated Mg and Mg-10Ni NCs. In addition to the TGA profiles for the samples, Figure 2.7 shows the Kissinger plots

derived from the TGA data. The Kissinger plots can be used to derive an activation energy (E_d, kJ mol^{-1}) for the desorption via the Kissinger equation:

$$-\ln\left(\frac{\beta}{T_m^2}\right) = \frac{E_d}{RT_m} - \ln\left(\frac{AR}{E_d}\right) \quad (2)$$

where β is the heating rate (°C min^{-1}), T_m is the temperature at which the most rapid decomposition takes place (K), R is the gas constant and A is the pre-exponential factor.[76] Using the slope of the Kissinger plots, E_d was calculated to be 155 ± 16 and 122 ± 2 kJ/mol for the pure Mg and Mg-10Ni NCs, respectively. These values are in good agreement with the values obtained by Liu *et al.* for their pure Mg NC samples (147.4 kJ/mol) and Mg-Ni nanocomposite (139.1 kJ/mol).[29] The desorption activation energy for the Mg-10Ni NCs corresponds to a ~43% and ~21% decrease with respect to bulk MgH_2 (213 ± 6 kJ/mol) and the pure Mg NCs, respectively.[23] The 27% decrease in the pure Mg NCs desorption activation energy (compared to bulk) can be attributed to the increased surface area due to nanostructuring, and also the potential for defects, strain, and vacancies from the low temperature synthesis.[15,29] These inherent defects due to the synthesis allow for an initially lowered activation barrier, but after a few cycles at higher temperature, the hydrogen desorption properties degrade (Figure S2.2).[24,49,77,78]

Interestingly, the TGA profiles for our hydrogenated Mg-10Ni NCs show two decomposition slopes. The first onset of mass loss is likely due to the desorption initiated at either a Mg_2NiH_4 or γ-MgH_2 site. As described earlier, both of these phases desorb hydrogen at lower temperatures than β-MgH_2.[20,22-24,65] Importantly, the amount of these secondary phases (Table 2.1) is in a much smaller percentage than can be contributed to this mass loss, suggesting these sites with the lowered activation energy act as a gateway for H_2 desorption from a portion of the bulk of the sample.[29,39] The identity of the initiating site is difficult to discern, however Ni has been

recognized to assist in the recombination of H atoms, giving Mg_2NiH_4 an ideal characteristic to act as a gateway for desorption.[65] However, Xiao *et al.* found that their ball-milled MgH_2 sample without any Ni catalyst addition decreased the activation energy for desorption by 46% with respect to the bulk (similar to our 41% reduction). They attribute this to the presence of γ-MgH_2 in their sample.[23] The existence of the second onset signifies inhomogeneity in the hydrogenated Mg-10Ni sample, which is expected due to the small percentages of secondary phases. We surmise that this second portion of the sample does not have access to these gateways, and thus has its own activation barrier of the inherent bulk β-MgH_2. Nonetheless, the temperature at which this second onset occurs is still lower than the onset for the pure MgH_2 sample, suggesting that the nucleation barrier is even lowered for the remainder of the sample. At the temperature of this second onset (>270 °C), the small amount of Mg_2NiH_4 and γ-MgH_2 would have already desorbed hydrogen, and thus the creation of a second "gateway" due to one of these phases dehydriding is improbable.[20,65] Thus, this lowered (second) desorption temperature is due to a lowered activation barrier for the bulk β-MgH_2. One possibility for this decrease is the lack of a Mg nucleation barrier, but the temperature difference for the second onset is 30-50°C lower than the desorption onset for the pure MgH_2 NCs. Although decreased temperature for desorption has been observed for partially hydrogenated MgH_2 (i.e., where the Mg phase is present), this only results in a decrease of up to 20°C.[65] Therefore, we suggest that this decrease could be due to non-crystalline phase Ni inclusion in this portion of the sample, which would align with the EXAFS data suggesting that the majority of the Ni inclusion is disordered. This is further corroborated with the NMR data, that suggests the bulk of the hydrogen is influenced by Ni inclusion.

To study the local structure of the samples during desorption, we collected X-ray total scattering data on the hydrogenated forms (2nd cycle, 300 °C) of the Mg and Mg-10Ni NC samples

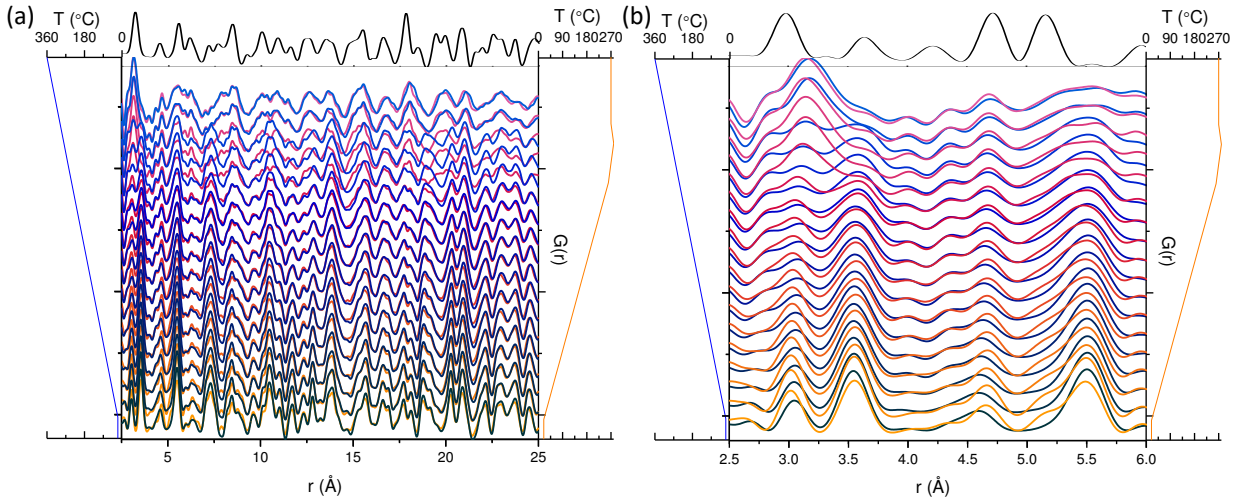

Figure 2.8. Overlaid *in situ* PDF analysis (*G(r)* vs. *r*) for (a) all and (b) smaller values of r for the dehydrogenation (under dynamic vacuum) of MgH_2 (blue traces) and Mg-10Ni (orange-red traces). The black traces correspond to the calculated *G(r)* vs. *r* for (a) Mg and (b) MgO. The *in-situ* temperature profile for the Mg (Mg-10Ni) sample is displayed on the left (right) side of the PDF data in blue (orange).

while being heated under vacuum. From this data, *in-situ* pair distribution function analysis can be performed (Figure 2.8). The function extracted from the total scattering data, *G(r)*, defines the probability of finding atoms at a distance *r* with the integrated intensity being dependent on the multiplicity of the atoms, and the coherence scattering lengths of the elements participating.[51,79] By taking into account the full range of collected X-ray scattering data, the PDF provides both local atomic structure and long range order of all elements (with substantial X-ray scattering ability) during the desorption of the samples.

In Figure 2.8, the *in situ G(r)* are displayed for the desorption of MgH_2 and Mg-10Ni-H_2 NCs. Looking at the longer-range *G(r)* (i.e., $2.5<r<25$), the samples appear very similar at room temperature and fit well to β-MgH_2 (Figure 2.8a and S2.12). As the temperature increases, the transition from β-MgH_2 to Mg takes place in the Mg-10Ni sample about 30 °C (~260-270 °C) earlier than for the pure Mg sample (Figure S2.13). This decrease in temperature for desorption is in agreement with the TGA data (Figure 2.7). Additionally, fitting of the data in Figure 2.8 at

various steps confirms that β-MgH_2 is the dominant structure that exists for both samples during temperature ramping. Unfortunately, taking a closer look at the low *r* for these samples, it is evident that a MgO impurity exists in the Mg-10Ni sample (Figure 2.8b, Figure S2.13). This is likely due to oxidation during sample preparation. Consequently, the signal from the MgO appears to be the main contribution to differences in the pure and Ni added samples. As such, it is difficult to make any dramatic conclusions due to subtle differences between the samples. Nonetheless, these high intensity features display the similarity in the short-range order of these samples during desorption. Although it takes place at different temperature, the transition is marked by a subtle and gradual shift in the integrated intensity from the nearest neighbor from ~3.0 Å to ~3.2 Å. This is accompanied by a decrease in intensity for the peak at ~3.6 Å (a major MgH_2 peak). Importantly, this data confirms the persistence of characteristic peaks due to the major phase (i.e. β-MgH_2) during transition, as was suggested by the TGA data. To reiterate, this *in situ* data suggests that the nucleation of the Mg phase in both Ni doped and pure MgH_2 NCs occurs without any dramatic rearrangement of the local geometry prior to transition.

2.5 Conclusions:

Mg and Mg/Ni NCs that is, with and without the addition of Ni, were successfully synthesized through a solution-based method. The introduction of Ni into the synthesis was found to have no significant effect on the size of the resulting Mg NCs. Upon hydrogenation of Mg NCs with only 1.6 at. % Ni, *ex situ* SR-XRD verified the formation of β-MgH_2 with a small amount of metastable γ-MgH_2, as well as cubic and monoclinic Mg_2NiH_4. Furthermore, Ni K-edge X-ray absorption spectroscopy indicated a highly disordered local structure for the majority of the Ni in the NCs. Both the existence of the minority secondary phases, as well as the disordered nature of the Ni inclusion allowed for increased cycling efficiency, and dramatically decreased hydrogen

adsorption (~1/3) and desorption (~1/10) times for the Ni doped Mg NC system (with respect to the pure Mg NC system). Deuterium local structure behavior observed in the Ni doped samples by SS NMR spectroscopy was indicative of perturbations to the bulk hydrogen environment leading to a decreased activation energy for hydrogen desorption (~122 kJ/mol) compared to the pure MgH_2 (~155 kJ/mol). Finally, the *in-situ* PDF data acquired during desorption of the hydrogenation of the hydrogenated NCs support this conclusion. The local geometry and short/long range order in the hydrogenated samples is dominated by the β-MgH_2 phase, without any obvious transition to another phase required for desorption. Nonetheless, the SR-XRD of the Mg-Ni samples after a full hydrogen adsorption cycle at 300 °C/350 °C still exhibit the γ-MgH_2 phase. The reformation of this metastable phase after cycling at these temperatures is reportedly improbable, but is proposed to be due to the disordered nature of the Ni treated sample observed via the comprehensive structural characterization.

REFERENCES

(1) Schlapbach, L.; Zuttel, A. *Nature* **2001**, *414*, 353.
(2) Aguey-Zinsou, K.-F.; Ares-Fernandez, J.-R. *Energy & Environmental Science* **2010**, *3*, 526.
(3) Berube, V.; Radtke, G.; Dresselhaus, M.; Chen, G. *Int J Energ Res* **2007**, *31*, 637.
(4) Zaluska, A.; Zaluski, L.; Strom-Olsen, J. O. *Appl. Phys. A* **2001**, *72*, 157.
(5) Crivello, J. C.; Dam, B.; Denys, R. V.; Dornheim, M.; Grant, D. M.; Huot, J.; Jensen, T. R.; de Jongh, P.; Latroche, M.; Milanese, C.; Milčius, D.; Walker, G. S.; Webb, C. J.; Zlotea, C.; Yartys, V. A. *Applied Physics A* **2016**, *122*.
(6) Crivello, J. C.; Denys, R. V.; Dornheim, M.; Felderhoff, M.; Grant, D. M.; Huot, J.; Jensen, T. R.; de Jongh, P.; Latroche, M.; Walker, G. S.; Webb, C. J.; Yartys, V. A. *Applied Physics A* **2016**, *122*.
(7) Shissler, D. J.; Fredrick, S. J.; Braun, M. B.; Prieto, A. L. In *Low-Cost Nanomaterials*; Lin, Z., Wang, J., Eds. 2014, p 297.
(8) Bardhan, R.; Hedges, L. O.; Pint, C. L.; Javey, A.; Whitelam, S.; Urban, J. J. *Nat Mater* **2013**, *12*, 905.
(9) Shevlin, S. A.; Guo, Z. X. *J Phys Chem C* **2013**, *117*, 10883.
(10) Vajeeston, P.; Ravindran, P.; Fichtner, M.; Fjellvåg, H. *The Journal of Physical Chemistry C* **2012**, *116*, 18965.
(11) Buckley, A. C.; Carter, D. J.; Sheppard, D. A.; Buckley, C. E. *The Journal of Physical Chemistry C* **2012**, *116*, 17985.
(12) Au, Y. S.; Obbink, M. K.; Srinivasan, S.; Magusin, P. C. M. M.; de Jong, K. P.; de Jongh, P. E. *Advanced Functional Materials* **2014**, *24*, 3604.
(13) Chung, C. J.; Nivargi, C.; Clemens, B. *Physical chemistry chemical physics : PCCP* **2015**, *17*, 28977.
(14) Liu, W.; Aguey-Zinsou, K.-F. *Journal of Materials Chemistry A* **2014**, *2*, 9718.
(15) Norberg, N. S.; Arthur, T. S.; Fredrick, S. J.; Prieto, A. L. *Journal of the American Chemical Society* **2011**, *133*, 10679.
(16) Reich, J. M.; Wang, L.-L.; Johnson, D. D. *The Journal of Physical Chemistry C* **2012**, *116*, 20315.
(17) Yu, Q.; Qi, L.; Mishra, R. K.; Zeng, X.; Minor, A. M. *Applied Physics Letters* **2015**, *106*, 261903.
(18) Ares-Fernández, J.-R.; Aguey-Zinsou, K.-F. *Catalysts* **2012**, *2*, 330.
(19) Zhao-Karger, Z.; Hu, J.; Roth, A.; Wang, D.; Kubel, C.; Lohstroh, W.; Fichtner, M. *Chemical communications* **2010**, *46*, 8353.
(20) Shen, C.; Aguey-Zinsou, K.-F. *Journal of Materials Chemistry A* **2017**, *5*, 8644.
(21) Denys, R. V.; Riabov, A. B.; Maehlen, J. P.; Lototsky, M. V.; Solberg, J. K.; Yartys, V. A. *Acta Materialia* **2009**, *57*, 3989.
(22) Zhou, S.; Zhang, Q.; Chen, H.; Zang, X.; Zhou, X.; Wang, R.; Jiang, X.; Yang, B.; Jiang, R. *Int J Hydrogen Energ* **2015**, *40*, 11484.
(23) Xiao, X.; Liu, Z.; Saremi-Yarahmadi, S.; Gregory, D. H. *Physical chemistry chemical physics : PCCP* **2016**, *18*, 10492.

(24) Sander, J. M.; Ismer, L.; Van de Walle, C. G. *Int J Hydrogen Energ* **2016**, *41*, 5688.
(25) Tao, S. X.; Kalisvaart, W. P.; Danaie, M.; Mitlin, D.; Notten, P. H. L.; van Santen, R. A.; Jansen, A. P. J. *Int J Hydrogen Energ* **2011**, *36*, 11802.
(26) Shang, C. X.; Bououdina, M.; Song, Y.; Guo, Z. X. *Int J Hydrogen Energ* **2004**, *29*, 73.
(27) Liu, T.; Qin, C. G.; Zhang, T. W.; Cao, Y. R.; Zhu, M.; Li, X. G. *J Mater Chem* **2012**, *22*, 19831.
(28) Liu, Y.; Zou, J.; Zeng, X.; Ding, W. *RSC Advances* **2014**, *4*, 42764.
(29) Liu, Y.; Zou, J.; Zeng, X.; Wu, X.; Li, D.; Ding, W. *The Journal of Physical Chemistry C* **2014**, *118*, 18401.
(30) Jeon, K. J.; Moon, H. R.; Ruminski, A. M.; Jiang, B.; Kisielowski, C.; Bardhan, R.; Urban, J. J. *Nature Materials* **2011**, *10*, 286.
(31) Rieke, R. D.; Li, P. T.-J.; Burns, T. P.; Uhm, S. T. *J. Org. Chem.* **1981**, *46*, 4323.
(32) Liu, Y.; Zou, J.; Zeng, X.; Ding, W. *RSC Advances* **2015**, *5*, 7687.
(33) Manivasagam, T. G.; Magusin, P. C. M. M.; Iliksu, M.; Notten, P. H. L. *The Journal of Physical Chemistry C* **2014**, *118*, 10606.
(34) Barkhordarian, G.; Klassen, T.; Bormann, R. *J. Alloy. Compd.* **2006**, *407*, 249.
(35) Barkhordarian, G.; Klassen, T.; Bormann, R. *The journal of physical chemistry. B* **2006**, *110*, 11020.
(36) Barkhordarian, G.; Klassen, T.; Bormann, R. *Scripta Mater* **2003**, *49*, 213.
(37) da Conceição, M. O. T.; Brum, M. C.; dos Santos, D. S.; Dias, M. L. *J. Alloy. Compd.* **2013**, *550*, 179.
(38) Hanada, N.; Ichikawa, T.; Isobe, S.; Nakagawa, T.; Tokoyoda, K.; Honma, T.; Fujii, H.; Kojima, Y. *J Phys Chem C* **2009**, *113*, 13450.
(39) Ma, T.; Isobe, S.; Wang, Y. M.; Hashimoto, N.; Ohnuki, S. *J Phys Chem C* **2013**, *117*, 10302.
(40) Ma, X.; Xie, X.; Liu, P.; Xu, L.; Liu, T. *Progress in Natural Science: Materials International* **2017**.
(41) Maurizio, C.; Checchetto, R.; Trapananti, A.; Rizzo, A.; D'Acapito, F.; Miotello, A. *The Journal of Physical Chemistry C* **2015**, *119*, 7765.
(42) Liang, G.; Huot, J.; Boily, S.; Van Neste, A.; Schulz, R. *J. Alloy. Compd.* **1999**, *292*, 247.
(43) Shahi, R. R.; Tiwari, A. P.; Shaz, M. A.; Srivastava, O. N. *Int J Hydrogen Energ* **2013**, *38*, 2778.
(44) Zeng, X. Q.; Cheng, L. F.; Zou, J. X.; Ding, W. J.; Tian, H. Y.; Buckley, C. *Journal of Applied Physics* **2012**, *111*.
(45) Mustafa, N. S.; Ismail, M. *J. Alloy. Compd.* **2017**, *695*, 2532.
(46) Reich, J. M.; Wang, L.-L.; Johnson, D. D. *The Journal of Physical Chemistry C* **2014**, *118*, 6641.
(47) Wang, H.-C.; Wu, D.-H.; Wei, L.-T.; Tang, B.-Y. *The Journal of Physical Chemistry C* **2014**, *118*, 13607.
(48) Du, A. J.; Smith, S. C.; Yao, X. D.; Lu, G. Q. *The Journal of Physical Chemistry B* **2005**, *109*, 18037.
(49) Han, Z.; Chen, H.; Zhou, S. *Applied Surface Science* **2017**, *394*, 371.
(50) Srinivasan, S.; Magusin, P. C. M. M.; Kalisvaart, W. P.; Notten, P. H. L.; Cuevas, F.; Latroche, M.; van Santen, R. A. *Physical Review B* **2010**, *81*.
(51) Chupas, P. J.; Chapman, K. W.; Chen, H.; Grey, C. P. *Catalysis Today* **2009**, *145*, 213.

(52) Song, M. Y.; Kwak, Y. J.; Kwon, S. N.; Park, H. R. *Korean Journal of Metals and Materials* **2014**, *52*, 829.
(53) Tan, Y.; Mao, Q.; Su, W.; Zhu, Y.; Li, L. *RSC Adv.* **2015**, *5*, 63202.
(54) Wakefield, B. J. In *Organomagnesium Methods in Organic Synthesis*; Academic Press: London, 1995, p 21.
(55) Conradson, S. D.; Manara, D.; Wastin, F.; Clark, D. L.; Lander, G. H.; Morales, L. A.; Rebizant, J.; Rondinella, V. V. *Inorganic Chemistry* **2004**, *43*, 6922.
(56) Scherrer, P. *Nachr. Ges. Wiss. Gottingen* **1918**, *26*, 98.
(57) Barich, D. H.; Gorman, E. M.; Zell, M. T.; Munson, E. J. *Solid State Nuclear Magnetic Resonance* **2006**, *30*, 125.
(58) Zaluski, L.; Zaluska, A.; Stromolsen, J. O. *J. Alloy. Compd.* **1995**, *217*, 245.
(59) Shao, H. Y.; Xu, H. R.; Wang, Y. T.; Li, X. G. *Nanotechnology* **2004**, *15*, 269.
(60) Martínez-Coronado, R.; Retuerto, M.; Torres, B.; Martínez-Lope, M. J.; Fernández-Díaz, M. T.; Alonso, J. A. *Int J Hydrogen Energ* **2013**, *38*, 5738.
(61) Tran, X. Q.; McDonald, S. D.; Gu, Q. F.; Nogita, K. *J. Alloy. Compd.* **2015**, *636*, 249.
(62) Karimi, F.; Pranzas, P. K.; Pistidda, C.; Puszkiel, J. A.; Milanese, C.; Vainio, U.; Paskevicius, M.; Emmler, T.; Santoru, A.; Utke, R.; Tolkiehn, M.; Minella, C. B.; Chaudhary, A. L.; Boerries, S.; Buckley, C. E.; Enzo, S.; Schreyer, A.; Klassen, T.; Dornheim, M. *Physical chemistry chemical physics : PCCP* **2015**, *17*, 27328.
(63) Fernández, A.; Deprez, E.; Friedrichs, O. *Int J Hydrogen Energ* **2011**, *36*, 3932.
(64) Shirai, M.; Murakami, K.; Nishiyama, Y. *Energy & Fuels* **1997**, *11*, 1012.
(65) Xie, L.; Li, J.; Zhang, T.; Kou, H. *Int J Hydrogen Energ* **2016**, *41*, 5716.
(66) Shinde, S. S.; Kim, D.-H.; Yu, J.-Y.; Lee, J.-H. *Nanoscale* **2017**, *9*, 7094.
(67) Zlotea, C.; Oumellal, Y.; Hwang, S.-J.; Ghimbeu, C. M.; de Jongh, P. E.; Latroche, M. *The Journal of Physical Chemistry C* **2015**, *119*, 18091.
(68) Lang, J.; Eagles, M.; Conradi, M. S.; Huot, J. *J. Alloy. Compd.* **2014**, *583*, 116.
(69) Corey, R. L.; Ivancic, T. M.; Shane, D. T.; Carl, E. A.; Bowman, R. C.; Bellosta von Colbe, J. M.; Dornheim, M.; Bormann, R.; Huot, J.; Zidan, R.; Stowe, A. C.; Conradi, M. S. *The Journal of Physical Chemistry C* **2008**, *112*, 19784.
(70) Magusin, P. C. M. M.; Kalisvaart, W. P.; Notten, P. H. L.; van Santen, R. A. *Chemical Physics Letters* **2008**, *456*, 55.
(71) Conradi, M. S.; Mendenhall, M. P.; Ivancic, T. M.; Carl, E. A.; Browning, C. D.; Notten, P. H. L.; Kalisvaart, W. P.; Magusin, P. C. M. M.; Bowman, R. C.; Hwang, S.-J.; Adolphi, N. L. *J. Alloy. Compd.* **2007**, *446-447*, 499.
(72) Hayashi, S.; Orimo, S.-i.; Fujii, H. *J. Alloy. Compd.* **1997**, *261*, 145.
(73) Hayashi, S.; Nowak, B.; Orimo, S.-i.; Fujii, H. *J. Alloy. Compd.* **1997**, *256*, 159.
(74) Manivasagam, T. G.; Magusin, P. C. M. M.; Srinivasan, S.; Krishnan, G.; Kooi, B. J.; Notten, P. H. L. *Advanced Energy Materials* **2014**, *4*, 1300590.
(75) Grbović Novaković, J.; Matović, L.; Drvendžija, M.; Novaković, N.; Rajnović, D.; Šiljegović, M.; Kačarević Popović, Z.; Milovanović, S.; Ivanović, N. *Int J Hydrogen Energ* **2008**, *33*, 1876.
(76) Cho, Y.-S.; Shim, M.-J.; Kim, S.-W. *Materials Chemistry and Physics* **1998**, *52*, 94.
(77) Tanveer, H.; Abir De, S.; Tuhina Adit, M.; Weiwei, S.; Rajeev, A. *EPL (Europhysics Letters)* **2013**, *101*, 27006.
(78) Zhang, J.; Mao, C.; Chen, J.; Long, C. G.; Tang, K.; Zhang, M. J.; Peng, P. *Computational Materials Science* **2015**, *105*, 71.

(79) Nguyen-Phan, T.-D.; Liu, Z.; Luo, S.; Gamalski, A. D.; Vovchok, D.; Xu, W.; Stach, E. A.; Polyansky, D. E.; Fujita, E.; Rodriguez, J. A.; Senanayake, S. D. *The Journal of Physical Chemistry C* **2016**, *120*, 3472.

APPENDIX I

SUPPORTING INFORMATION FOR CHAPTER 2: ACCESSING METASTABLE STRUCTURES UNDER MILD CONDITIONS: LOCAL AND EXTENDED STRUCTURE CHARACTERIZATION OF NANOCRYSTALLINE MAGNESIUM AND ITS HYDROGENATION KINETICS

Max B. Braun, Amy L. Prieto

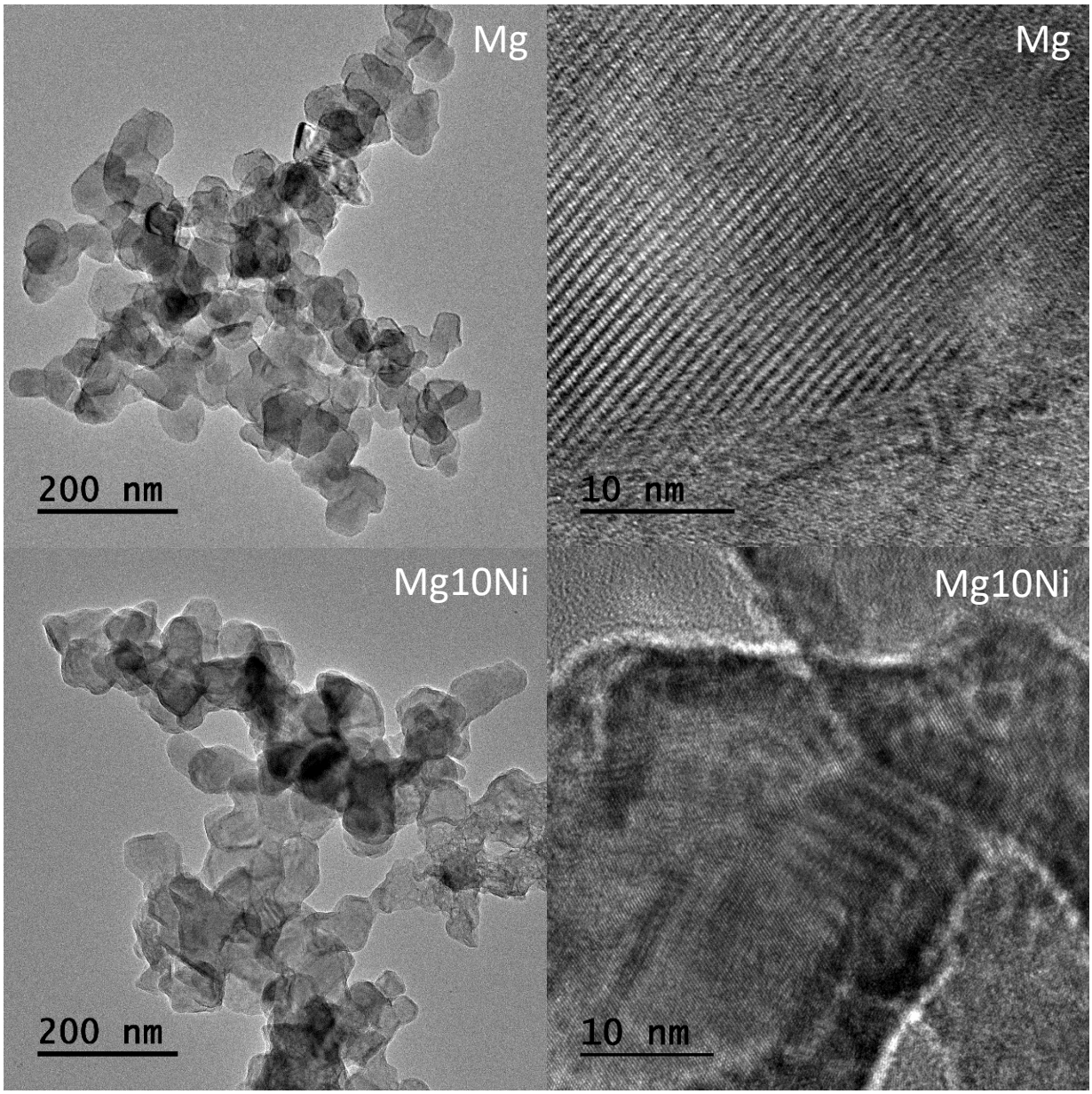

Figure S2.1. TEM and HR TEM images of the as-made Mg and Mg-10Ni samples

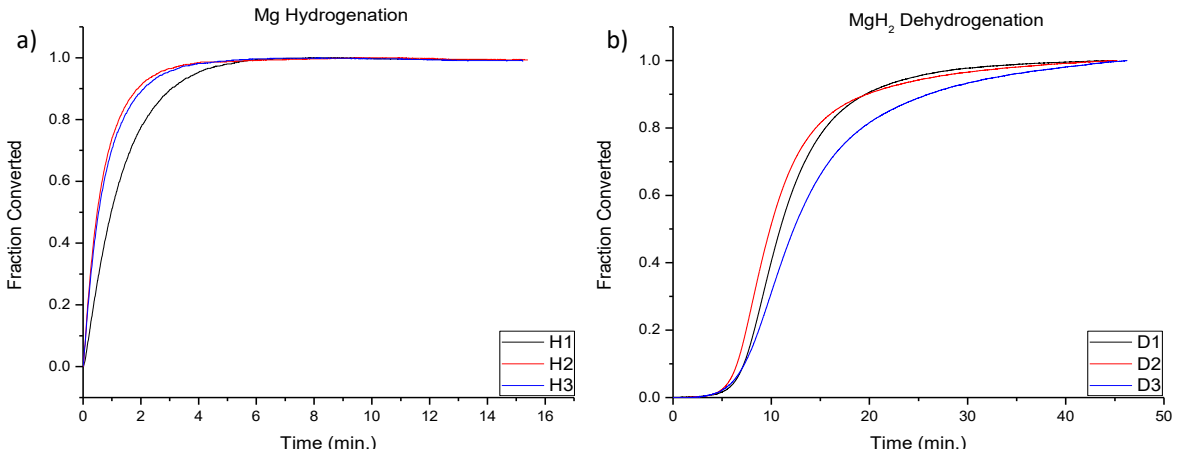

Figure S2.2. Extended cycling at 300 °C and 350 °C for pure Mg samples. A significant decrease is seen in the kinetics for the third dehydrogenation. The total amount of hydrogen adsorbed (desorbed) decreased by 9% (26%) from cycles 1 to 3.

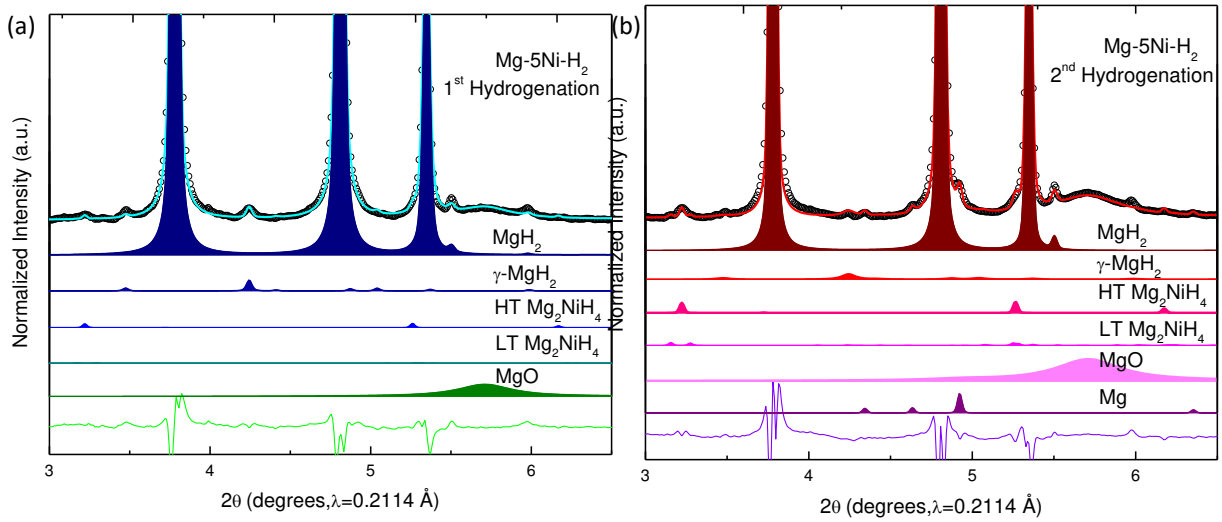

Figure S2.3. Phase-decomposed contributions to fittings from Rietveld refinement of the *ex situ* SR-XRD pattern s for the (a) first and (b) second hydrogenation (performed at 300 °C) of a Mg-5Ni sample.

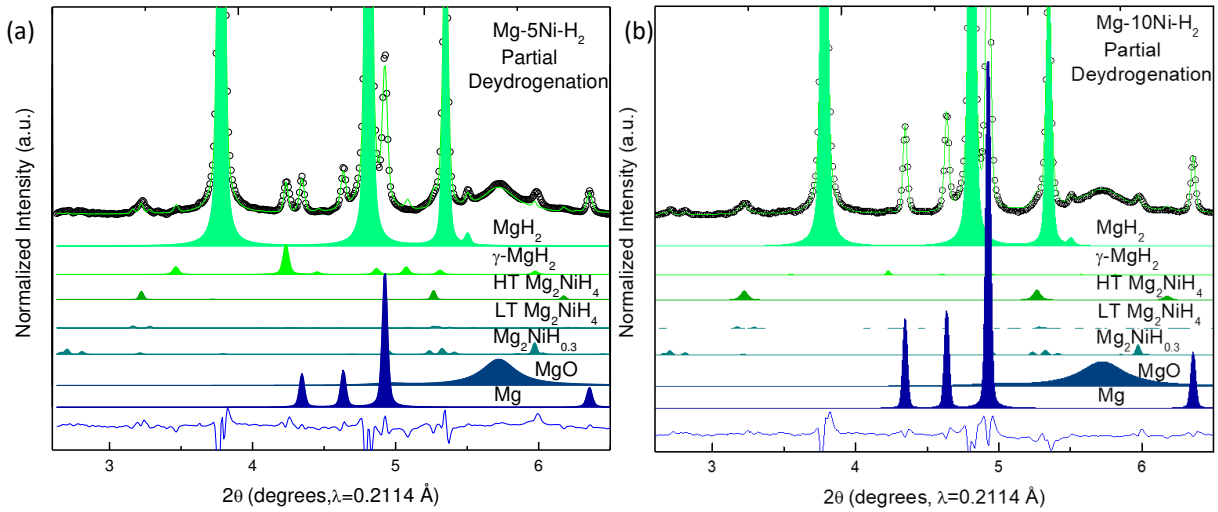

Figure S2.4. Phase-decomposed contributions to fittings from Rietveld refinement of the ex situ SR-XRD patterns for a partially dehydrogenated (after the second hydrogenation) (a) Mg-5Ni and (b) Mg-10Ni sample.

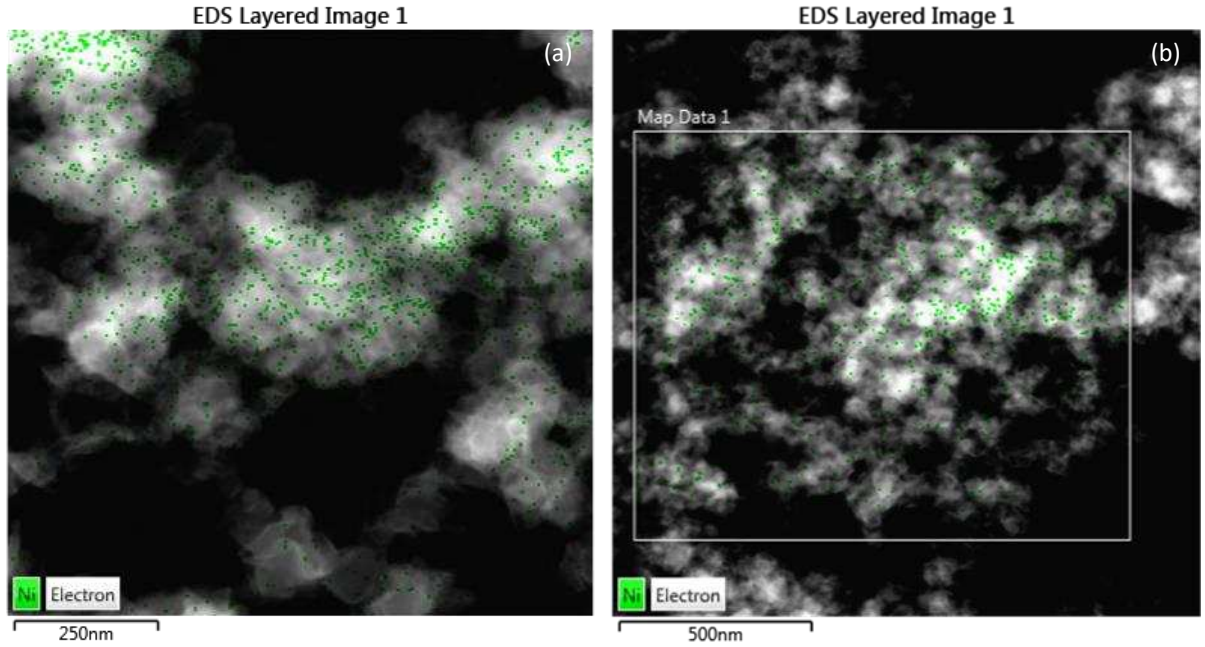

Figure S2.5. STEM-EDS maps of the (a) raw and (b) hydrogenated configurations of a Mg-10Ni sample.

Table S2.1: Ni wt % contributions in each nanocomposite from Rietveld refinements of *ex situ* SR-XRD data at various hydrogen cycling stages

		1st Hydrogenation	2nd Hydrogenation	Partial Dehydrogenation
Material	**Phase**	**Ni Abundance (wt %)**		
Mg-5Ni: Hydrogenations at 300℃, dehydrogenations at 350℃Partial hydrogenation after second hydrogenation	HT Mg_2NiH_4	0.05	0.13	0.12
	LT Mg_2NiH_4	0.01	0.07	0.06
	$Mg_2NiH_{0.3}$	-	-	0.21
	Total	0.06	0.20	0.39
Mg-10Ni: Hydrogenations at 300℃, dehydrogenations at 350; Partial hydrogenation after second hydrogenation	HT Mg_2NiH_4	0.23	1.33	0.32
	LT Mg_2NiH_4	0.07	0.06	0.07
	$Mg_2NiH_{0.3}$	-	-	0.20
	Total	0.30	1.39	0.39

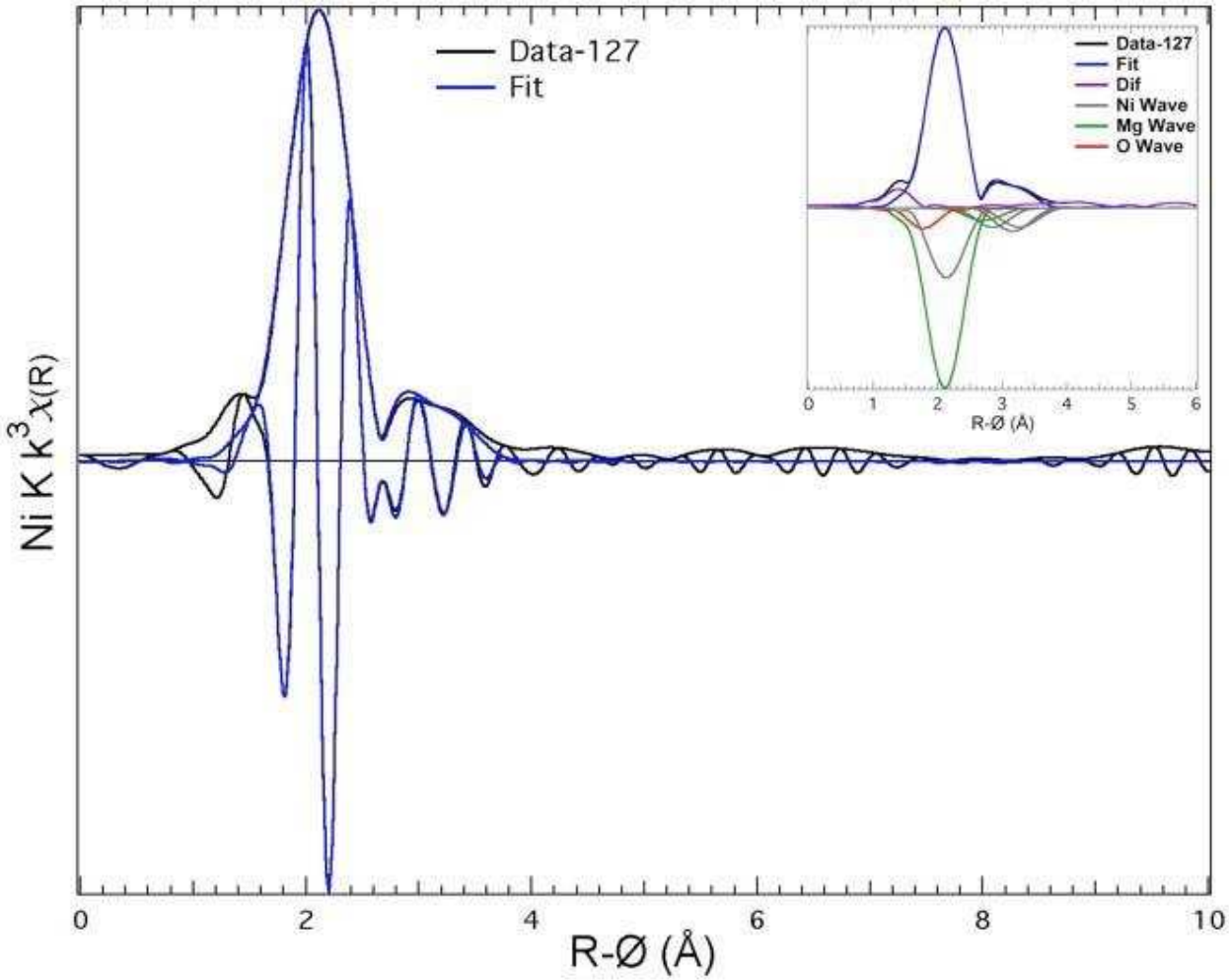

Figure S2.6. Fitting of EXAFS data for sample 127. The inset shows the difference (purple) in the data and fit as well as the individual Ni, Mg, and O waves.

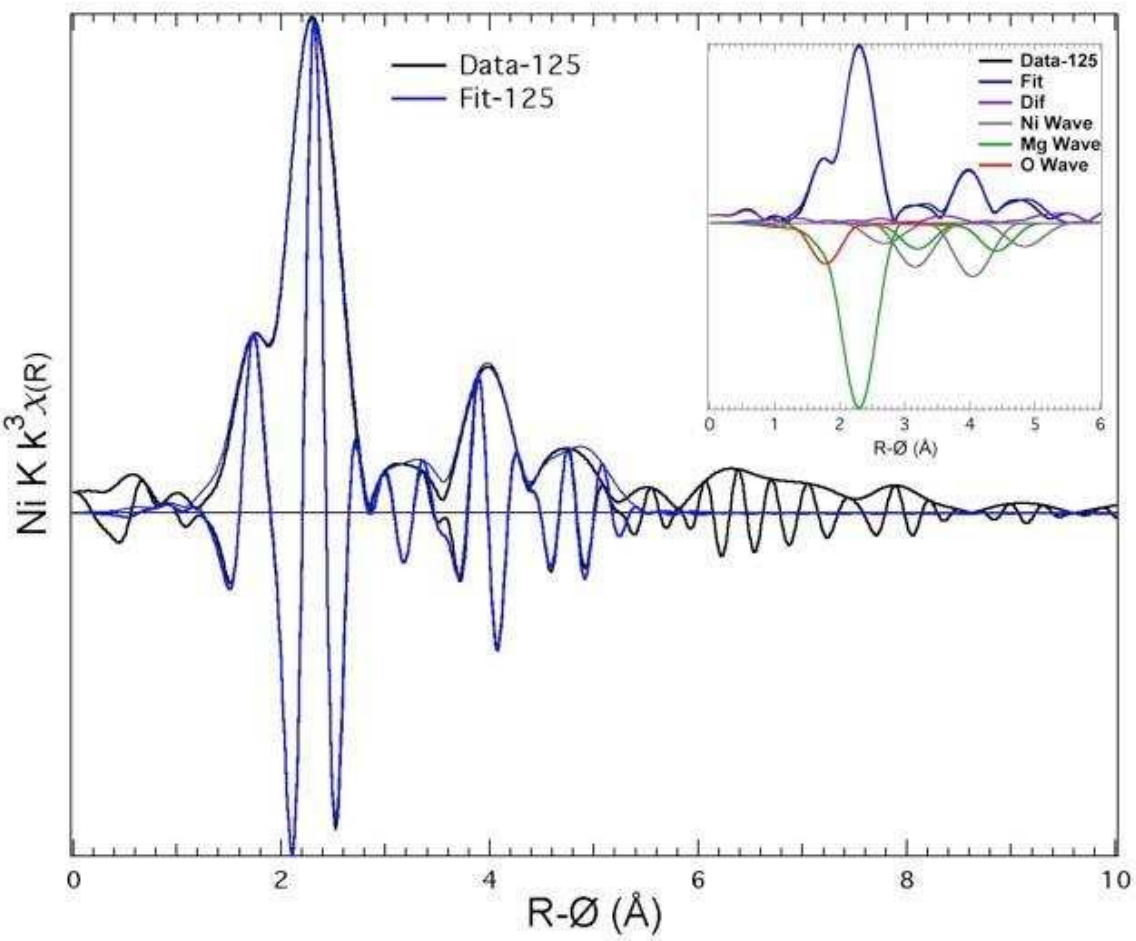

Figure S2.7. Fitting of EXAFS data for sample 125. The inset shows the difference (purple) in the data and fit as well as the individual Ni, Mg, and O waves.

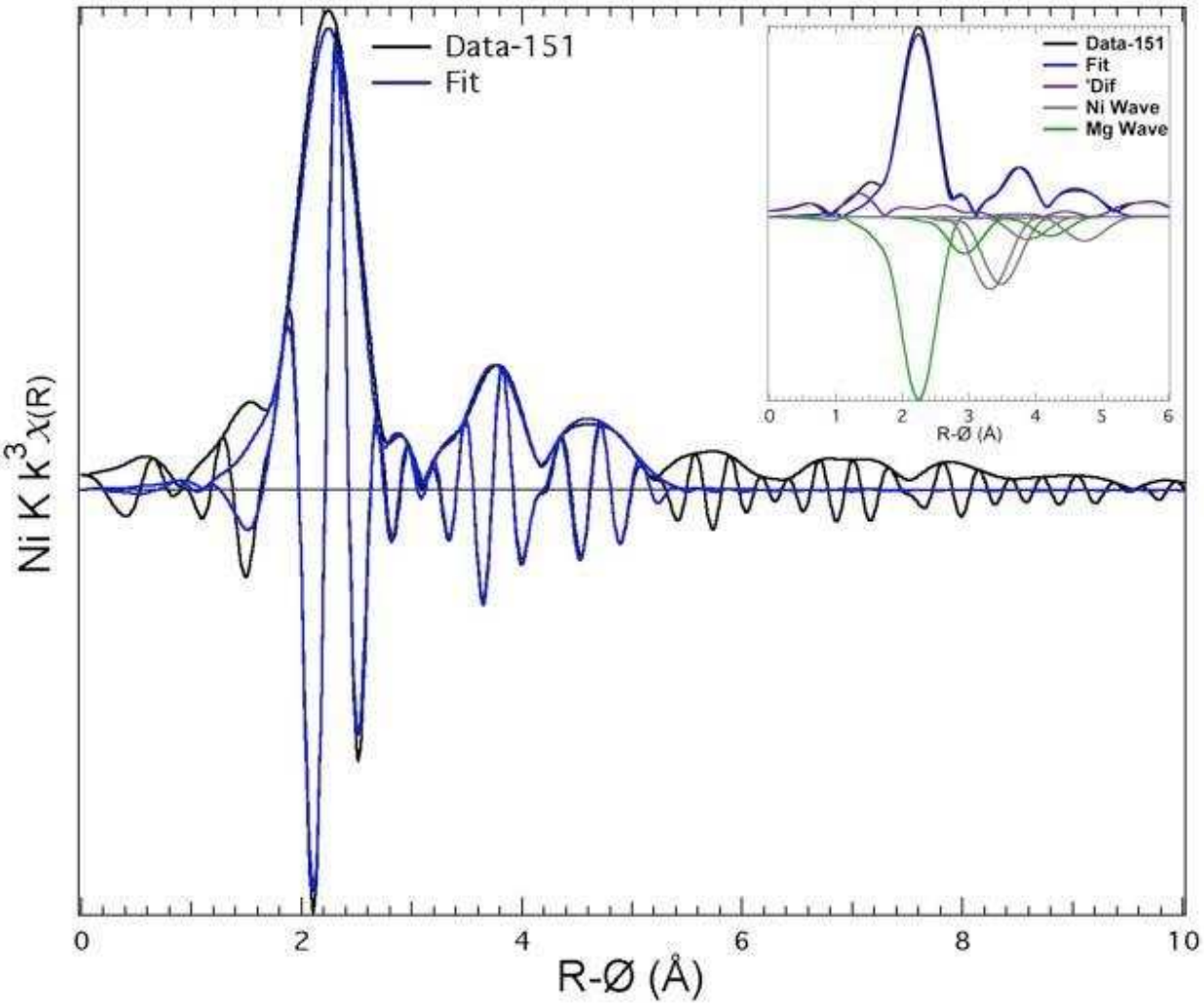

Figure S2.8. Fitting of EXAFS data for sample 151. The inset shows the difference (purple) in the data and fit as well as the individual Ni and Mg waves.

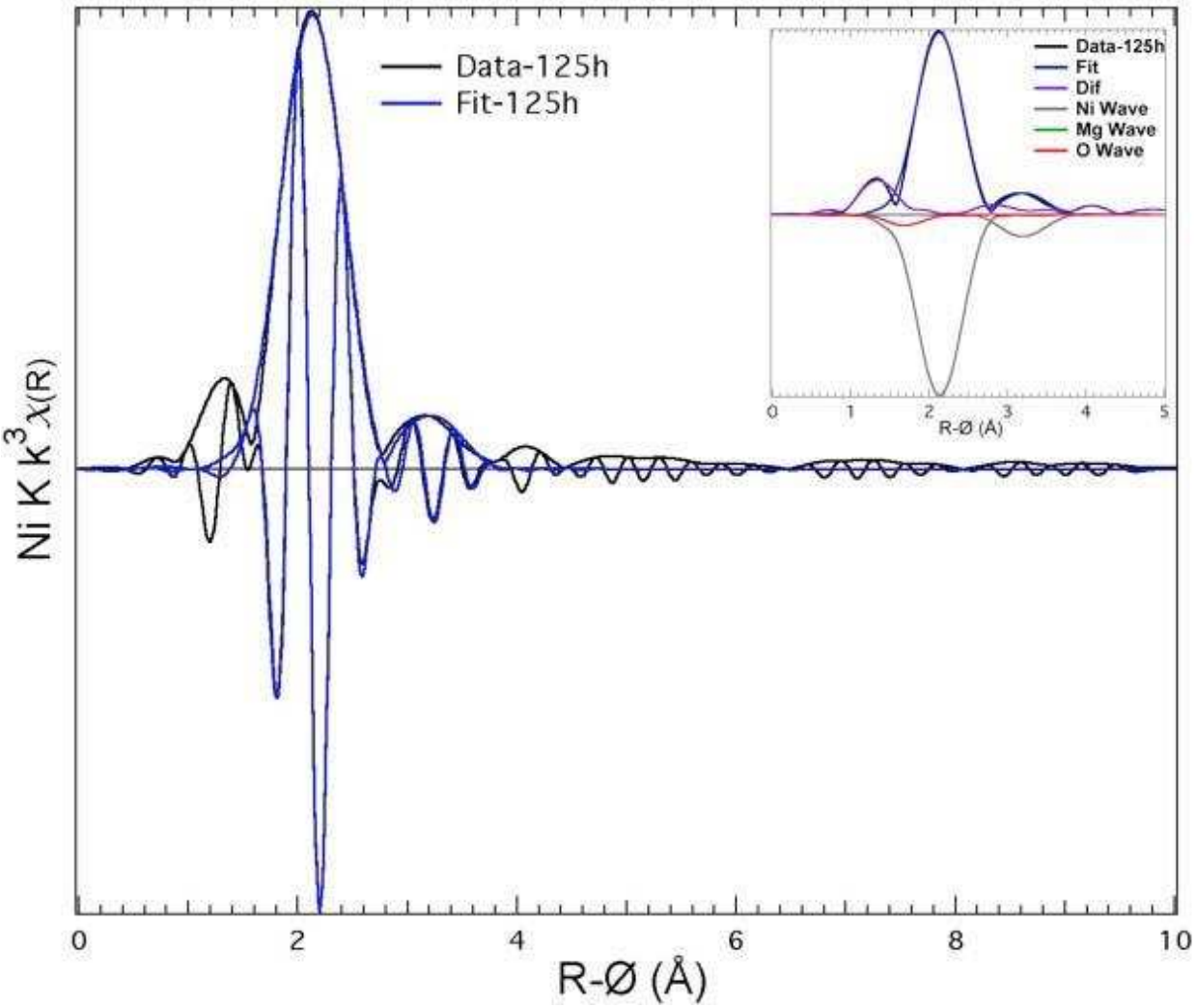

Figure S2.9. Fitting of EXAFS data for sample 125h. The inset shows the difference (purple) in the data and fit as well as the individual Ni, Mg and O waves.

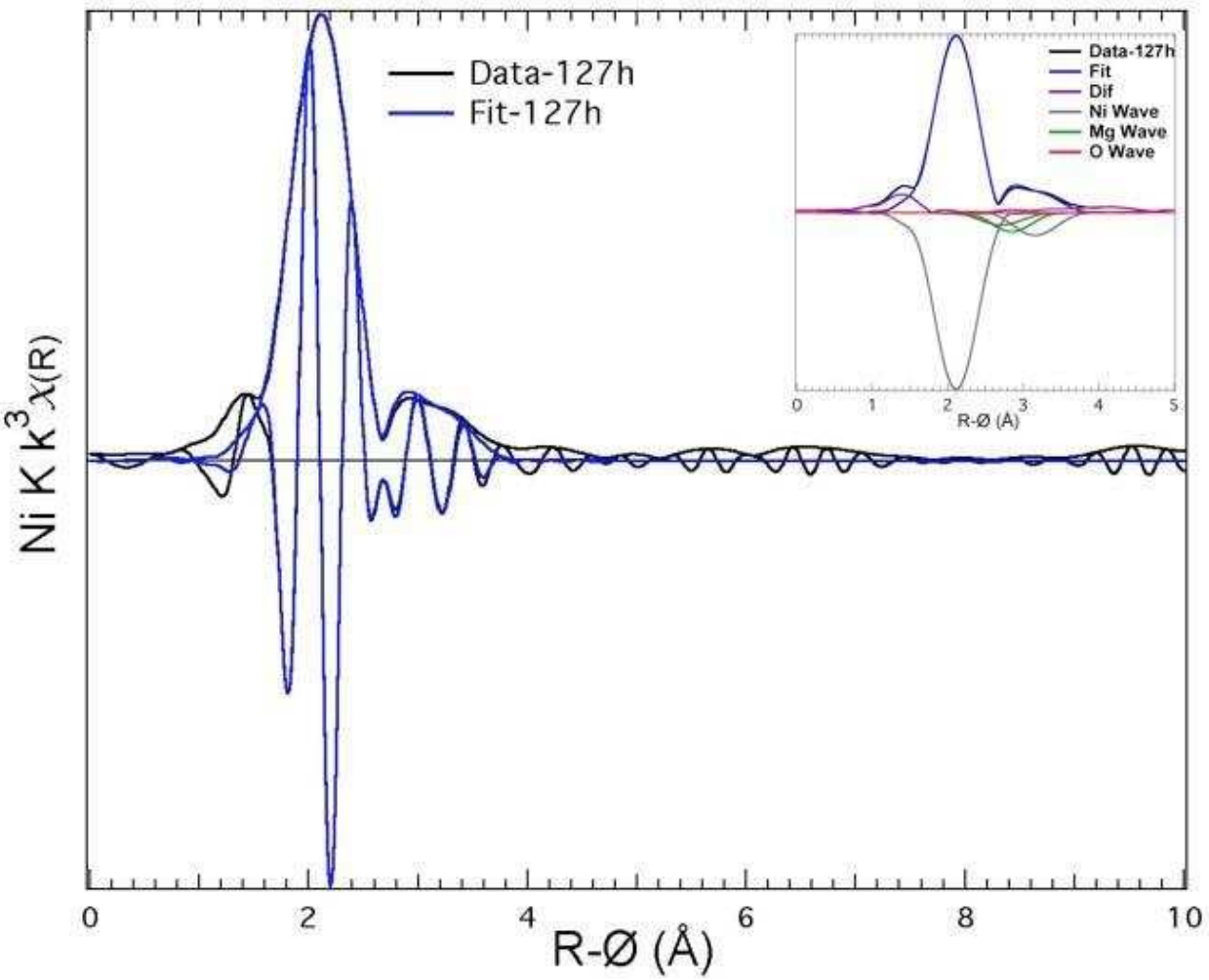

Figure S2.10. Fitting of EXAFS data for sample 127h. The inset shows the difference (purple) in the data and fit as well as the individual Ni, Mg and O waves.

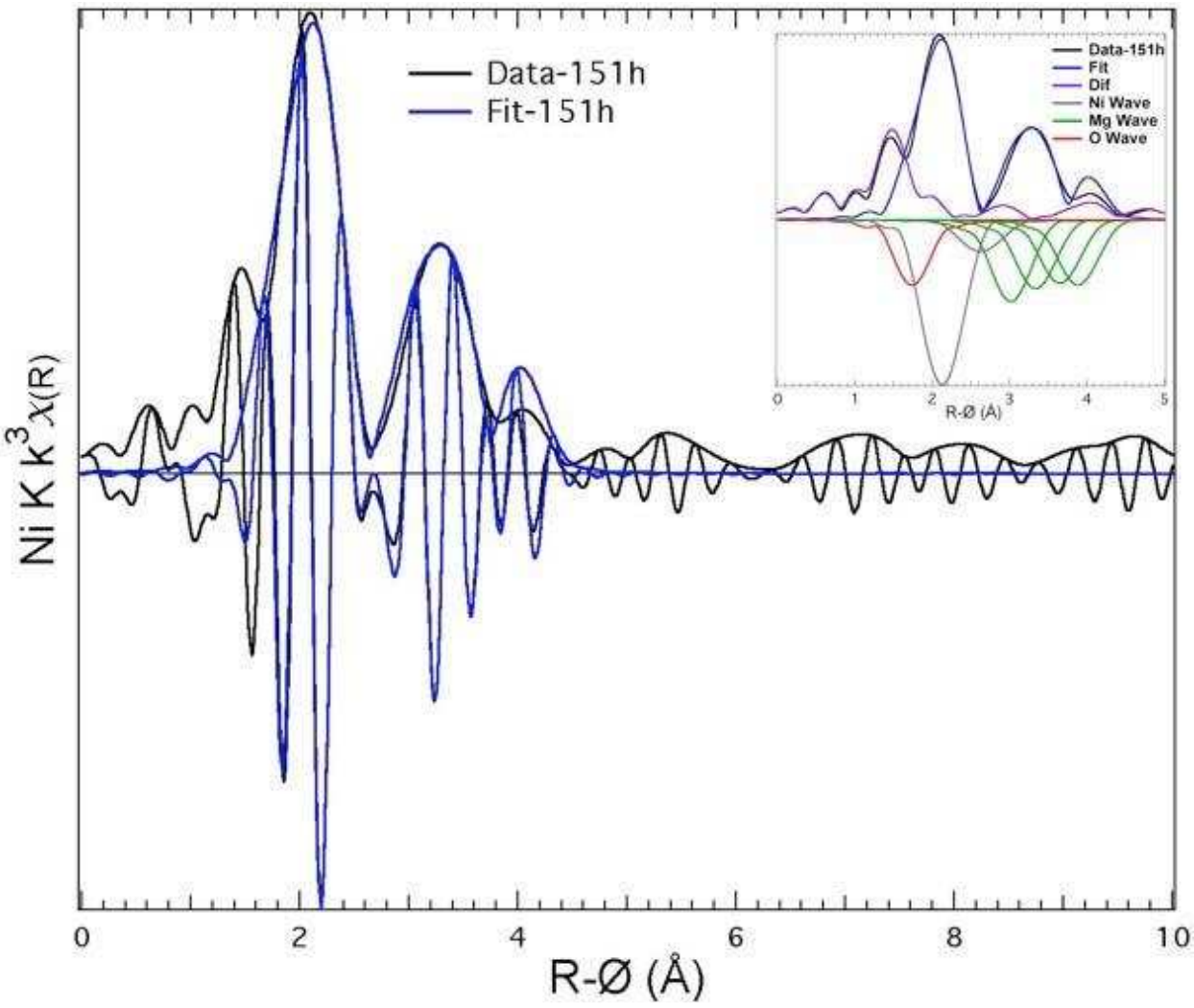

Figures S2.11. Fitting of EXAFS data for sample 151h. The inset shows the difference (purple) in the data and fit as well as the individual Ni, Mg and O waves.

Table S2: Ni K-Edge EXAFS curve-fitting parameters for de/hydrogenated Mg-1Ni, Mg-5Ni, and Mg-10Ni samples

Sample	Shell	Neighbor Atom	Distance	Coordination Number	σ (Å)	Δ*E* (eV)
Mg-1Ni	6	O	2.17	0.2	0.050	2.59
(125)	1	Mg	2.68	1.8	0.089	1.59
	3	Ni	2.99	0.1	0.070	3.59
	8	Ni	3.48	0.3	0.070	0.59
	7	Mg	3.58	0.4	0.070	2.59
	2	Ni	4.36	1.2	0.070	2.59
	4	Mg	4.80	0.8	0.070	1.59
	5	Ni	5.18	0.4	0.070	-0.41
Mg-1Ni-H_2	5	O	2.09	0.1	0.030	-1.96
(125h)	1	Ni	2.48	2.1	0.098	-0.96
	4	Ni	3.10	0.0	0.060	-1.96
	3	Mg	3.22	0.0	0.060	-0.96
	2	Ni	3.52	0.3	0.060	0.04
Mg-5Ni	6	O	2.17	0.2	0.025	0.48
(127)	8	Ni	2.46	0.3	0.060	0.48
	1	Mg	2.73	0.9	0.065	1.48
	3	Ni	3.03	0.2	0.070	2.87
	7	Ni	3.58	0.3	0.070	2.48
	2	Ni	4.34	1.6	0.070	0.48
	4	Mg	4.73	1.3	0.070	1.48
	5	Ni	5.18	0.5	0.070	-0.52
Mg-5Ni-H_2	5	O	1.00	0.0	0.040	-2.84
(127h)	1	Ni	2.47	1.7	0.092	-3.84
	4	Ni	3.06	0.1	0.060	-4.84
	3	Mg	3.26	0.4	0.060	-2.37
	2	Ni	3.51	0.3	0.060	-2.84
Mg-10Ni	1	Mg	2.65	1.8	0.087	-3.53
(151)	6	Mg	3.34	0.5	0.070	-2.53
	7	Ni	3.67	0.5	0.070	-2.53
	3	Ni	3.86	0.6	0.070	-5.53
	2	Ni	4.25	0.5	0.070	-2.53
	4	Mg	4.66	0.6	0.070	-3.53
	5	Ni	5.13	0.4	0.070	-5.53
Mg-10Ni-H_2	8	O	2.13	0.2	0.000	-1.16
(151h)	7	Mg	2.42	0.0	0.050	-1.16
	1	Ni	2.47	0.3	0.066	-2.16
	4	Ni	2.96	0.1	0.070	-1.16
	3	Mg	3.42	0.8	0.070	-0.28
	2	Mg	3.75	0.8	0.070	-1.16
	6	Mg	4.06	1.0	0.070	-1.16
	5	Mg	4.30	1.1	0.070	-1.16

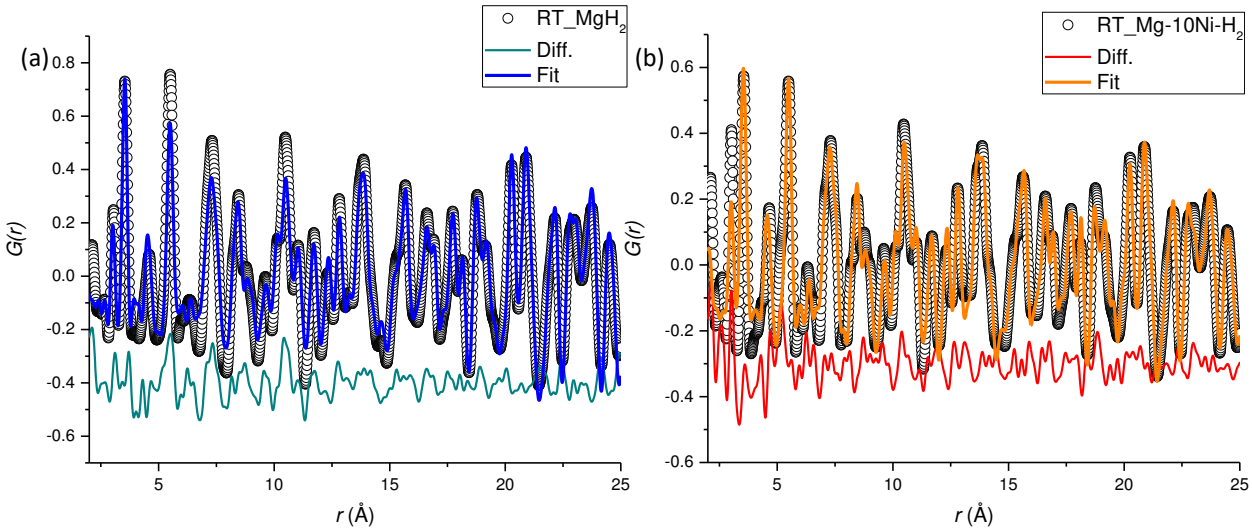

Figure S2.12. Fitting of PDF data for room temperature (a) MgH_2 and (b) Mg-10Ni-H_2 samples with the β-MgH_2 phase.

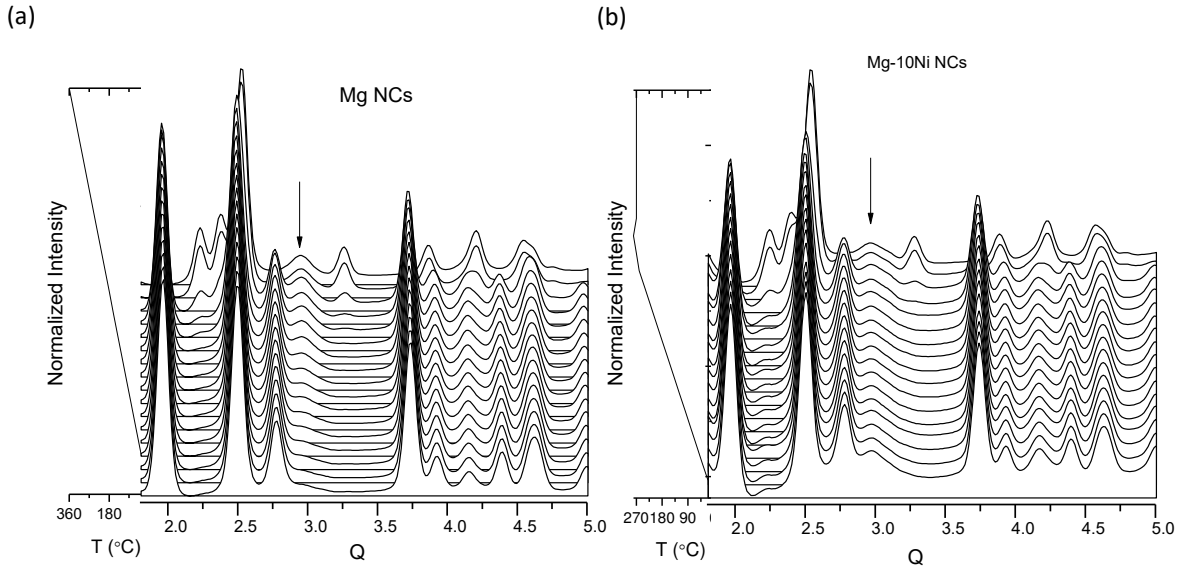

Figure S2.13. *In-situ* I(Q) vs Q for the total scattering data obtained for the hydrogenated forms of Mg and Mg-10Ni NCs heated to 360 °C and 270 °C under dynamic vacuum. The arrow indicates peaks that belong MgO.

PART II: SYNTHESIS, FILM DEPOSITION, AND CHARACTERIZATION OF QUATERNARY METAL CHALCOGENIDE NANOCRYSTALS FOR PHOTOVOLTAIC APPLICATIONS

CHAPTER 3: INTRODUCTION TO SYNTHETIC DEVELOPMENT OF NANOCRYSTALS OF COPPER ZINC TIN CHALCOGENIDE[3]

3.1 Nanoscale copper zinc tin chalcogenides for photovoltaic applications

Inspired by the highly-researched $CuIn_yGa_{1-y}(S_{1-x}Se_x)_2$ (CIGS) system that is at the forefront of thin film PV technologies, research into $Cu_2ZnSn(S_{1-x}Se_x)_4$ (CZTSSe) for photovoltaics has received considerable attention in the last decade.[1-3] With a desirable band gap range (E_g = 1.0-1.5 eV) and reaching conversion efficiencies up to 12.6%, thin-film photovoltaic devices based on a kesterite/stannite (CZTS/CZTSe) absorber layer are attractive due to the constituents being earth abundant, relatively non-toxic alternatives to the CIGS system.[4] However, the champion cells were fabricated using a hydrazine based process, hydrazine being an explosive toxin. Alternatively, the colloidal synthesis of CZTSSe nanocrystals (NCs) offers a route toward low-cost, solution-based processing of the absorber layer.[5-10] However, PV devices based on the selenization of CZTS NCs have only reached a champion efficiency of 9.0%.[11] Importantly, the selenization step used in these champion cells (i.e., both the hydrazine-based and NC-based) leads to cation rearrangement throughout the absorber layer.[11-14] It is well established that the composition, especially with respect to the cations, has dramatic effects on a CZTSSe films physical and electrical properties.[6,15-22] While the use of the selenization step has produced the best performing devices (based on CZTSSe), the consequences of such the high temperature chemical treatment makes it difficult to understand CZTSSe's fundamental chemistry and its effects on the

[3] This chapter has been written by Max B. Braun with assistance in editing and direction provided by Amy L. Prieto.

CZTSSe materials physical properties.[9,14] One of the severe detriments to CZTSSe-based devices lies in the large (>600 mV) open circuit voltage deficit ($V_{oc,def} = \frac{Eg}{q} - V_{oc}$) exhibited in these devices. Improvement in device efficiency has not been reported since 2014.[23] The reasons for the large $V_{oc,def}$ are poorly understood, and still the topic of current research.[4,6,9,23-25] In order for continued progress of the CZTSSe material and its application in photovoltaic devices, it is necessary to understand the role of the various elements on the resulting characteristics exhibited in films/devices made from the material, especially at the nanoscale.[14,22,26]

It is well established that CZTSSe films with a zinc rich, copper poor concentration results in better photoelectrical transport properties, and ultimately increased photovoltaic performance. While there have been multiple reports on varying cationic (i.e., Cu, Zn, and Sn) ratios effects on the properties of CZTSSe films, systematic investigations into the role of chalcogen ratio (i.e., S/Se) on film properties are lacking.[15-19,21,23,26-32] Nonetheless, champion $Cu_2ZnSn(S_{1-x}Se_x)_4$ devices have all had comparatively heavy selenium content, with band gaps centered around ~1.15 eV.[4] Previously, Tai *et al*. reported on CZTSSe film characteristics made via the hydrazine-based process (i.e., selenization of molecular precursors in the presence of hydrazine), and found that with increasing selenium content, the carrier density decreased.[25] In contrast, Duan *et al.* concluded that the carrier concentration increased with increasing selenium content.[32] This discrepancy is likely due to complications introduced during the high-temperature selenization step, which can dramatically change film properties depending on selenization time, and temperature.[11-13,26,33] Alternatively, films made from un-annealed CZTSSe NCs offer a route towards fundamental investigations on the CZTSSe material, without the complication of the selenization step.[9] Syntheses of nanomaterials, specifically those based on colloidal synthetic procedures, offer the ability to tune not only composition, but also surface chemistry, and bulk electrical, optical, and

magnetic properties.[6,9,34,35] Additionally, NCs that can then easily suspended in solution can then be used in the formation of a "nanoink", which allows for low cost roll-to-roll processing of PV devices.[6,7,34,35] However, film deposition methods for unannealed, unselenized CZTSSe NCs are largely unexplored. As such, the next chapter (Chapter 4) focuses on the development of surface-ligand exchange strategies to deposit films that allow for a fundamental understanding of the role that NC composition and surface chemistry play in CZTSSe NC film properties and PV device performance.

However, in the present chapter we discuss the search and development of a synthetic route for CZTSSe nanocrystals with control over all constituent elements. Albeit there being multiple routes that have been developed for the synthesis of the full chalcogen range (x=0 to x=1) of $Cu_2ZnSn(S_{1-x}Se_x)_4$ NCs, these methods either produce NCs with undesirable cation ratios (i.e., $Cu/(Zn+Sn)>0.8$, $Zn/Sn<1.35$) or the particles do not suspend in solution, thereby preventing film deposition and consequent study. Specifically, syntheses of NCs of the selenium rich analog (CZTSe) were often reported to result in zinc-deficient (<12.5% Zn) particles.[6,29,35-39] For these reasons, a new synthetic approach is necessary.

Herein we will highlight some of the notable previous attempts and approaches to the syntheses of the full range of S to Se, CZTSSe NCs. This is not intended to be a comprehensive review of the different approaches and attempts, but rather an introduction to the various considerations we took in our own synthetic development of zinc rich CZTSe, and consequently, CZTSSe NCs. During the synthetic development, specific attention was paid to maintaining desirable cationic ratios for all compositions of the CZTSSe without sacrificing particle size, morphology, and ability to suspend.

3.2 Experimental

During the CZTSSe NC synthetic development multiple metal precursors, solvents, surfactants, and experimental techniques were screened. For these investigative reactions, the metal precursors tin(IV) chloride ($SnCl_4$, 99%), tin(iv) chloride pentahydrate ($SnCl_4 \cdot 5H_2O$, 98%), zinc(II) acetate ($Zn(OAc)_2$, 99.99%), copper(II) acetylacetonate ($Cu(acac)_2$, 99.99%), and copper(I) chloride (CuCl, 99.995%) as well as trioctylphosphine (TOP, technical grade, 90%), octadecene (ODE, technical grade, 90%), trioctylphosphine oxide (TOPO, 99%), technical grade oleylamine (OLA, 70%) glycerol (>99.5%), and oleic acid (OA, technical grade, 90%) were all purchased from Aldrich Chemical Co., Inc. The metal precursors tin(IV) acetate ($Sn(OAc)_4$), Zinc(II) chloride ($ZnCl_2$, 98%) as well as the solvents hexanes (99.9%), and toluene (99.9%) were purchased from Thermo Fisher Scientific Inc. Oleylamine (OLA, 80-90%) was purchased from Acros Organics. Copper(II) chloride ($CuCl_2$, 98%) and tin(II) chloride dihydrate ($SnCl_2 \cdot 2H_2O$) were bought from Alfa Aesar. Finally, methanol was purchased from Malinchrodt Chemical Inc. The reagent chemicals listed above were stored in an inert N_2 glove box. The solvents and surfactants used in the glove box, e.g. TOP, TOPO, ODE, and OLA were purged with N_2 for a minimum of 3 hours and/or run through cycles of freeze, pump, and thawing before being used in the glove box.

For the case study to be presented in section 3.3.3, the syntheses of CZTSSe NCs were performed following a novel synthetic protocol synthetic protocol. In an N_2 glovebox, 1.8 mmol of Cu(I)Ac, 1.2 mmol $ZnAc_2$, 1.0 mmol $SnCl_4 \cdot 5H_2O$, and 4 total mmol of Se and S was added to a 100mL round-bottomed flask with a stirbar. Outside the glovebox, 30 mL of oleylamine (OLA) and 5-10 g of glycerol were charged into the round-bottomed. After isolating the reaction from the atmosphere with rubber septa, the solution was heated to 115 ℃ while stirring under N_2 flow. The

solution was then heated to 260-270 °C and allowed to stir for 45 minutes to 1 hour under N_2 overpressure. The heat was removed and the reaction was allowed to cool to room temperature. The precipitate was collected by the addition of ethanol and centrifugation at 5800 RPM. The supernatant was discarded and the precipitate was then re-suspended in chloroform and centrifuged for 5 minutes at 5800 RPM. The supernatant was transferred to new centrifuge tubes and precipitated by the addition of ethanol and centrifugation at 5800 RPM for 5 minutes. This washing process of suspension and precipitation was performed once more and the final product was kept for analysis in a nitrogen glovebox. It is worth noting the "discarded" precipitate was occasionally kept and analyzed in order to better understand the reaction. Nonetheless, the suspended product was the product of primary interest, and so synthetic direction was usually founded on the characteristics of this product.

During the synthetic development of the CZTSSe nanocrystals, the elemental composition was analyzed by energy dispersive spectroscopy (EDS) in a JEOL JSM 7000F FE-scanning electron microscopy (SEM) equipped with an EDAX OCTANE SUPER silicon drift detector. The crystalline phase(s) of the as-made NCs was identified via powder X-ray diffraction (XRD) performed on a Scintag X-2 Advanced Diffraction system equipped with Cu Kα radiation (λ = 1.54 Å) using a zero background SiO_2 sample holder. The NCs size and morphology were imaged on a JEOL JEM-1400 TEM at a working voltage of 100 kV.

3.3 Developing the synthesis of zinc rich CZTSSe NCs

3.3.1 Brief introduction to hot injection vs heat up synthesis of colloidal NCs

One of the most common routes toward CZTSSe nanocrystal syntheses is via the hot injection method.[7] This method is based on the concepts of nucleation and growth, and involves

the rapid injection of "cold" metal precursor solutions into a hot surfactant. [6,7,40,41] Upon injection into the surfactant, the metal cationic and anionic precursors combine to form monomers. These monomers rapidly combine to precipitate in the form of nanoscale nuclei. From here, growth proceeds via additional deposition reactions taking place at the surface of the nuclei. As growth proceeds, Ostwald ripening can occur, where smaller nuclei re-dissolve in solution, and eventually add to larger particles. In order to maintain control over growth and crystallite size, the number of monomers formed must be considered, and is most easily adjusted via changing the metal to surfactant ratio (i.e.,concentration). [7,40,41]

Importantly, the use of surfactant has multiple purposes in colloidal NC syntheses. First, it prevents the uncontrolled growth of the crystals by sterically and kinetically hindering the deposition of more reactants onto the surface. Second, the surfactant (also often referred to as the ligand) caps the NCs and allows for continued suspension in solution. Importantly, the electron withdrawing/donating nature of the ligand can influence how well it binds to the NC surface. Whether it is x-type (both metal and ligand donating one electron), l-type (donates two electrons to metal), or z-type (accepts two electrons from metal), affects how strongly and to which metal site a ligand will attach.[42,43] Although there are numerous surfactants (ligands), some of the most common surfactants (ligands) used in colloidal NC synthesis are trioctylphosphine oxide (TOPO), trioctylphosphine (TOP), octylphosphonic acid (OPA), dodecanethiol (DDT), hexadecylamine (HAD), oleylamine (OLA), and finally oleic acid (OA).[35,40] Phosphines, phosphine oxides, and amines are examples of L-type ligands, while long chain acids and thiolates are examples of X-type ligands.[40,43] This characteristic of the ligand was extremely important when the developing deposition procedures (Chapter 4, *vide infra*). Nonetheless, each of the surfactants has its own advantages and disadvantages; however, due to the toxicity and price of the phosphine-based

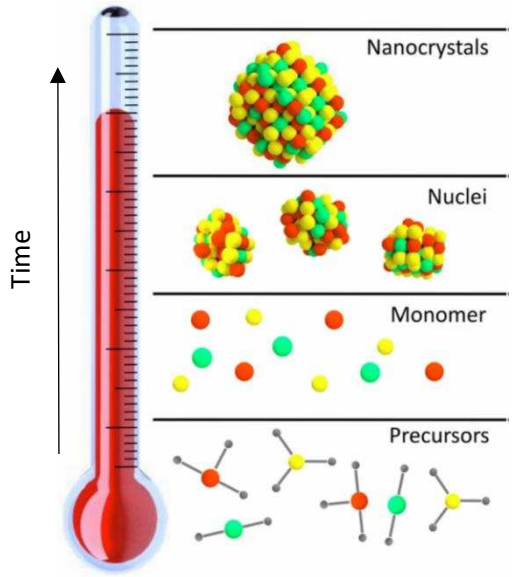

Figure 3.1 The steps of nanocrystal formation during the "heat-up"[35] synthetic method. As the temperature is increased over time, the precursors form monomers that react and form small nuclei, which grow into larger NCs. Adapted from Reference [35].

ligands, the colloidal synthesis field has pushed for the preferential use of the amines and thiols.[7,36,44,45] As such, one of our initial goals was to devise a synthesis that did not require the expensive and toxic phosphine precursors.

In addition to the identity of the surfactant, there are many factors that affect the nucleation and growth of the CZTSSe NCs. These include the temperature (of both the surfactant and metal precursor solutions), the identity and concentration of the precursors, and time. In a complicated system, such as the quinary CZTSSe system, differences in the synthetic parameters can result in drastic changes in NC characteristics (i.e., morphology, size, crystalline phase, composition, and surface chemistry).[7,34] Although these factors allow for a considerable amount of synthetic control and alteration, they-especially temperature-also make it increasing the scale of the synthesis, and render reproducibility challenging.[35]

Alternatively, the aptly named “heat-up” synthesis of colloidal NCs involves the combining of all reactants and solvents into a single pot which is then heated while stirring (Figure

3.1). This approach is attractive due to its scalability and ease of reproducibility, without sacrificing too much synthetic control or ability to produce high quality NCs.[35] Recently, van Embden *et al.* reviewed the synthetic parameters that can be controlled and utilized when performing heat-up syntheses of colloidal NCs.[35] Similar to hot-injection syntheses, heat-up synthesis is also founded on the concepts of nucleation, agglomeration, and growth. Thus, the temperature (more specifically the heating rate), surfactant (termed stabilizer) identity, as well as precursor concentration and identity all influence monomer and nuclei formation, and ultimately the quality of the NC product. However, these parameters-again, especially temperature- are much more easily reproduced batch-to-batch compared to the hot-injection method. Finally, through the systematic evaluation of the species existing at various stages of reaction, the authors conclude that precursor identity and surfactant have the largest effect on monomer and nuclei identity and size.[35] However, with careful parameter (i.e., time, heating rate, and temperature) refinement, plus knowledgeable selection of precursor and surfactant, high-quality NCs can be obtained. Ultimately, the heat-up method for NC syntheses was chosen in our synthetic pursuit due to its inherent advantages in scalability, ease of synthesis, and batch to batch reproducibility over the hot-injection method.

3.3.2 Synthesis of zinc rich $CZTS_{1-x}Se_x$: Se dissolution

One of the main considerations that must be taken into account for the synthesis of CZTSe is the selenium precursor reactivity and its dissolution. Compared to sulfur, selenium has a lower electron affinity, which makes it more difficult to form Se_x^{n-} anions (required for dissolution). Additionally, due to the anionic radius of the Se being larger than that of S, the negative charge is more easily delocalized, resulting in a lower reactivity.[29] Consequently, the lability and the strength of the interaction of the ligand or surfactant with the Se can alter the anion's reactivity.[41,44]

Historically, methods to dissolve selenium involve highly reducing conditions, either by means of adding reducing agents, or by Se addition into relatively reducing solvents (e.g., phosphines) and consequent dissolution at high temperatures.[29,36,44-46] For example, Riha *et al.* report the addition of $NaBH_4$ with Se in oleylamine (OLA) to provide the Se precursor for their TOPO-based hot injection synthesis of CZTSSe particles. Although the resulting particles had near stoichiometric levels of zinc (close to 12.5 at. %), the use of $NaBH_4$ and TOPO can lead to particle etching (large particle size dispersion), and makes the approach more costly and less environmentally benign.[16] Alternatively, Liu *et al*. report on the use of alkylthiol to aid in the dissolution of Se in OLA for their phosphine-free hot-injection CZTSSe NC syntheses. Although this approach is cheaper and more environmentally friendly, sulfur is inevitably incorporated in the resulting CZTSe particles, making the synthesis of the pure Se analog unattainable.[36]

As an alternative, phosphine-free route for Se dissolution, Bullen *et al*. report on their investigations of an octadecene (ODE) selenium precursor by the heating of selenium in ODE at different temperatures.[44] The authors found that when the ODE-Se solution was heated for different amounts of time at various temperatures, it changed both in color and reactivity. They found that heating at 180 °C for 5 hours gave the most reactive ODE-Se precursor solution (0.1 M). As such, some of our initial CZTSe synthetic investigations were performed using a stock solution of ODE-Se (0.1 M) that was made following their procedure (discussed in the next section).[44] However, although these CZTSe synthetic attempts resulted in particles that were pure CZTSe by XRD, the zinc content was always below 10 at. % by EDS. Similarly, a hot-injection synthetic procedure developed by Ou *et al.* uses a similar ODE-Se (0.2 M) precursor for their synthesis of $Cu_2ZnSn(S_{1-x}Se_x)_4$ with (x=0, 0.3, 0.5, 0.7, and 1). Unfortunately, with respect to the

other compositions, the pure selenium analog (x=1) was found to be undesirably zinc deficient, and rich in tin.[37]

Finally, and most notably, a few recent reports use only elemental Se (i.e., no prior dissolution) in their heat-up syntheses with polyetheramine, or OLA/glycerol as the solvents.[38,47] Previously, the use of elemental Se precursor had not been reported for a phosphine-free synthesis of CZTSe. During the development of our synthetic approach, the use of glycerol as an additional reagent was reported by Ji *et al.* in the synthesis of high quality $CZTS_{1-x}Se_x$ NCs. Although their synthetic procedure produced particles with near stoichiometric CZTSe (Zn ~12 at. %), upon the repetition of their synthetic protocol, the particles did not suspend well enough for film deposition. Additionally, their protocol involved the injection of $SnCl_4$, which was undesirable. Nonetheless, as will be discussed in the next section, the use of glycerol in our synthesis eventually led to the successful incorporation of zinc into our CZTSe NCs.

3.3.3 Synthesis of zinc rich $CZTS_{1-x}Se_x$: Zinc incorporation

The main synthetic challenge, and the primary characteristic necessitating the development of alternative syntheses, is maintaining the cationic ratios for the full range of S to Se (i.e. x=0 to 1). On this topic, Rath *et al.* report the role that cationic precursor reactivity has on the final stoichiometry of CZTS(Se) nanocrystals synthesized via hot injection. The authors report that by increasing the reactivity of a metallic precursor, for example, changing $ZnCl_2$ to ZnI_2, the amount of zinc expressed in the product went from 1.1 to 4.6 atomic %. Furthermore, by suppressing the reactivity of the other cation (e.g., CuI to CuOAc, SnI_4 to $SnOAc_4$) the zinc will be further expressed in the product (4.6 to 10.6 at.% Zn). Relative reactivity of the precursors was based on the strength of the cation/anion interaction suggested by hard-soft acid-base theory (HSAB). The importance of the metal precursor choice in heat up syntheses is also demonstrated in the review

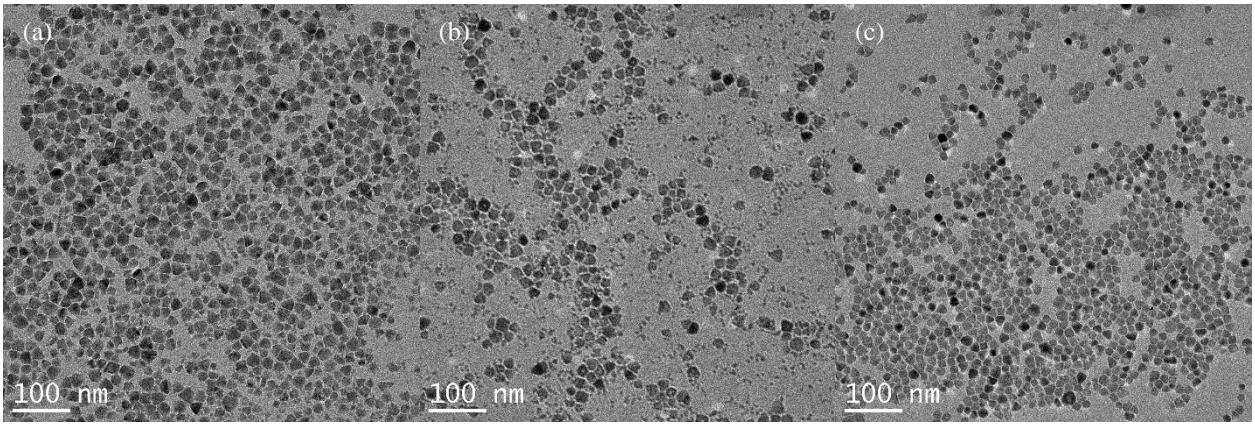

Figure 3.2. TEM images of CZTSe made with: (a) $Cu(OAc)$, $Zn(OAc)_2$, $SnCl_4 \cdot 5H_2O$ in OLA with glycerol (b) $Cu(acac)_2$, $Zn(OAc)_2$, $SnCl_2 \cdot 2H_2O$ in OLA without glycerol (c) $Cu(acac)_2$, $Zn(OAc)_2$, $SnCl_2 \cdot 2H_2O$ in OLA with glycerol

by van Emben *et al.* The authors use simulations to demonstrate that precursor reactivity not only determines the monomer identity (which can change the composition), but also the growth of nuclei nanocrystals.[35] Furthermore, the interaction of the surfactant or ligand with the metal cation and (as described in the previous section, the anion) can also influence the monomer and nuclei formation, as well as the growth of the NCs. Using arguments based on HSAB, van Embden *et al.* suggest that if the strength of the interaction of an cationic precursor and the surfactant is too large it will result slower nucleation. On the other hand, if the interaction is weak, a larger concentration of nuclei will form, which will result in larger particle size dispersion. In light of these conclusions, we tested a variety of precursors and ligands with different levels of reactivity.

Although an abundance of precursors and solvents were screened (see the experimental section for details) it was difficult to establish an overall trend based on reactivity of the precursors and solvents. However, there were a few observations during the screening process that proved pivotal to honing in on the necessary reaction parameters for sufficient zinc incorporation in CZTSe. In contrast to all other S/Se ratios (i.e., x=0, 0.3, 0.5, 0and 0.7), CZTSe synthesized following the protocol provided in section 3.2 always ended up slightly zinc deficient (~10-12 at. % Zn) and heavy in tin (~14-15 at. % Sn). However, this was better than CZTSe from reactions

that were synthesized with previously investigated metal precursors (leading to ~6-10 at. % Zn), and substantially better than those synthesized without the use of glycerol (~0-7 % Zn). One of the characteristics of CZTSe with particularly low Zn (<10 at. %), high Sn (>12.5 at. %) content was the small size (5-10nm) of the particles with respect to the other S/Se ratios (usually >15nm) synthesized under similar conditions. This is in agreement with findings by Collord *et al.* who looked at the differences in CZTS stoichiometry based on particle size. They found that CZTS particles with higher Sn content, and low zinc concentration were smaller than those with larger size.[30] This suggests that in our reactions that produced the smaller CZTSe particles, Sn rich nuclei nucleated in such a high concentration that the monomer was used up before significant growth could take place.[35,48]

The most successful (in terms of Zn content) reaction performed using this synthetic protocol provided particles that exhibited a bimodal size distribution (Figure 3.2a). While some of the particles are ~15-20 nm, there are also a lot of particles that are smaller than 10 nm. In contrast, CZTSe (~14-15 at. % Zn) following the final synthetic procedure described in our manuscript (Chapter 5), had much more of a Gaussian size distribution centered around 14 nm (Figure 3.2c). However, without the use of glycerol in the reaction there is an appearance of much smaller particles (Figure 3.2b), and the zinc content is low (~11 at. %), and tin is high (~14 at. %). This further suggests that the glycerol is helpful for zinc incorporation into the final suspended NC product. Using HSAB theory, Cu^{2+} and Sn^{2+} are soft Lewis acids compared to Zn^{2+}. Similarly, glycerol is a softer Lewis base compared to oleylamine. As such, by stabilizing copper and zinc cations in solution, glycerol is likely inhibiting rapid growth of Sn, Cu rich nuclei. Thus, Zn incorporation is possible during the growth of the nuclei into NCs.

Furthermore, the other two main differences between the final synthetic protocol (Chapter 5), and the protocol given in section 3.2 are the identities of the Sn and Cu precursors. Inspired by a one-pot synthesis of CZTS developed by Steinhagen *et al.* which uses copper(II)acetylacetonate and $SnCl_2 \cdot H_2O$ instead of CuOAc and $SnCl_4 \cdot 5H_2O$. Due to Sn^{2+} being a softer Lewis acid compared to Sn^{4+}, it will form a stronger interaction with the glycerol, thereby inhibiting growth of Sn rich nuclei. Similarly, copper(II)acetylacetonate is comparably slower in the forming of nuclei than copper(I)acetate, primarily due to the increased stability due to chelation of the acetylacetonate groups. Again, the inhibition of the growth of Cu,Sn rich nuclei provides the ability for zinc incorporation to take place. With the use of $Cu(acac)_2$ and $SnCl_2 \cdot H_2O$ as reactants, Zn incorporation was capable up to 17 atomic percent in the final suspended product. However, with zinc content this high, secondary phase formation is probable. Consequently, the last step in the synthetic pursuit was the tuning of the metal precursor concentrations to yield $CZTS_{1-x}Se_x$ with similar Zn for all S/Se ratios.

3.4 Summary

Ultimately, we were able to able to synthesize the full range of $Cu_2ZnSn(S_{1-x}Se_x)_4$ (x=0, 0.3, 0.5, 0,7, and 1), without sacrificing zinc content for any of the chalcogen ratios. Considering the large amount of literature existing in the colloidal syntheses of NCs, many considerations were taken into account. The use of a single pot, heat-up reaction was chosen for ease of synthetic reproducibility, and scalability. Carefully executed heat-up syntheses allowed for reproducibility in particle size, morphology, and cation and anion concentrations (verified by compositional analyses). Environmentally benign solvents and surfactants were chosen in lieu of the commonly used phosphine based surfactants order to reduce cost and environmental impact. Importantly, the particles have the ability to suspend, which allows for facile film deposition. Attention was paid

to minimizing cation and particle size variation between different chalcogen ratios so as to reduce the effects on the resulting film properties. Further characterization on the final product can be found in Chapter 5.

For the purpose of understanding the role of the chalcogen ratio on the CZTSSe NC film electrical properties and PV performance, the development of a film deposition strategy was necessary. The next chapter describes our investigation into tuning the surface ligand chemistry of CZTS NCs in order to achieve electrical communication between particles, without the use of a post annealing or selenization process.

REFERENCES

(1) Suryawanshi, M. P.; Agawane, G. L.; Bhosale, S. M.; Shin, S. W.; Patil, P. S.; Kim, J. H.; Moholkar, A. V. *Materials Technology* **2013**, *28*, 98.
(2) Polizzotti, A.; Repins, I. L.; Noufi, R.; Wei, S.-H.; Mitzi, D. B. *Energy Environ. Sci.* **2013**, *6*, 3171.
(3) Research Cell Efficiency Records, N.R.E.L, http://www.nrel.gov/ncpv/images/efficiency_chart.jpg.
(4) Wang, W.; Winkler, M. T.; Gunawan, O.; Gokmen, T.; Todorov, T. K.; Zhu, Y.; Mitzi, D. B. *Adv. Energy Mater.* **2014**, *4*, 1301465.
(5) Ramasamy, K.; Malik, M. A.; O'Brien, P. *Chemical communications* **2012**, *48*, 5703.
(6) Zhou, H.; Hsu, W.-C.; Duan, H.-S.; Bob, B.; Yang, W.; Song, T.-B.; Hsu, C.-J.; Yang, Y. *Energy Environ. Sci.* **2013**, *6*, 2822.
(7) Ghorpade, U.; Suryawanshi, M.; Shin, S. W.; Gurav, K.; Patil, P.; Pawar, S.; Hong, C. W.; Kim, J. H.; Kolekar, S. *Chemical communications* **2014**, *50*, 11258.
(8) Guo, Q.; Ford, G. M.; Yang, W.-C.; Walker, B. C.; Stach, E. A.; Hillhouse, H. W.; Agrawal, R. *J. Am. Chem. Soc.* **2010**, *132*, 17384.
(9) Korala, L.; Braun, M. B.; Kephart, J. M.; Tregillus, Z.; Prieto, A. L. *Chemistry of Materials* **2017**, *29*, 6621.
(10) Miskin, C. K.; Yang, W. C.; Hages, C. J.; Carter, N. J.; Joglekar, C. S.; Stach, E. A.; Agrawal, R. *Prog Photovoltaics* **2015**, *23*, 654.
(11) Miskin, C. K.; Yang, W.-C.; Hages, C. J.; Carter, N. J.; Joglekar, C. S.; Stach, E. A.; Agrawal, R. *Prog. Photovolt: Res. Appl.* **2015**, *23*, 654.
(12) Yin, X.; Tang, C.; Sun, L.; Shen, Z.; Gong, H. *Chemistry of Materials* **2014**, *26*, 2005.
(13) Hwang, Y.; Park, B.-I.; Lee, B.-S.; Kim, J. Y.; Jeong, J.-H.; Kim, H.; Ko, M. J.; Kim, B.; Son, H. J.; Lee, S. Y.; Lee, J.-S.; Park, J.-K.; Cho, S.-H.; Lee, D.-K. *The Journal of Physical Chemistry C* **2014**, *118*, 27657.
(14) Sardashti, K.; Haight, R.; Gokmen, T.; Wang, W.; Chang, L.-Y.; Mitzi, D. B.; Kummel, A. C. *Advanced Energy Materials* **2015**, *5*, 1402180.
(15) Katagiri, H.; Jimbo, K.; Tahara, M.; Araki, H.; Oishi, K. *MRS Proceedings* **2009**, *1165*.
(16) Riha, S. C.; Parkinson, B. A.; Prieto, A. L. *J. Am. Chem. Soc.* **2011**, *133*, 15272.
(17) Chen, S.; Walsh, A.; Yang, J.-H.; Gong, X. G.; Sun, L.; Yang, P.-X.; Chu, J.-H.; Wei, S.-H. *Physical Review B* **2011**, *83*, 125201.
(18) Nishi, H.; Kuwabata, S.; Torimoto, T. *The Journal of Physical Chemistry C* **2013**, *117*, 21055.
(19) Roelofs, K. E.; Guo, Q.; Subramoney, S.; Caspar, J. V. *Journal of Materials Chemistry A* **2014**, *2*, 13464.
(20) Yang, W.-C.; Miskin, C. K.; Carter, N. J.; Agrawal, R.; Stach, E. A. *Chemistry of Materials* **2014**, *26*, 6955.
(21) Li, J.; Wang, H.; Wu, L.; Chen, C.; Zhou, Z.; Liu, F.; Sun, Y.; Han, J.; Zhang, Y. *ACS Applied Materials & Interfaces* **2016**, *8*, 10283.
(22) Espinosa-Faller, F. J.; Conradson, D. R.; Riha, S. C.; Martucci, M. B.; Fredrick, S. J.; Vogel, S.; Prieto, A. L.; Conradson, S. D. *The Journal of Physical Chemistry C* **2014**, *118*, 26292.d

(23) Kanevce, A.; Repins, I.; Wei, S.-H. *Solar Energy Materials and Solar Cells* **2015**, *133*, 119.
(24) Gershon, T.; Gokmen, T.; Gunawan, O.; Haight, R.; Guha, S.; Shin, B. *MRS Commun.* **2014**, *4*, 159.
(25) Tai, K. F.; Gunawan, O.; Kuwahara, M.; Chen, S.; Mhaisalkar, S. G.; Huan, C. H. A.; Mitzi, D. B. *Adv. Energy Mater.* **2015**, *6*.
(26) Salvador, M.; Vorpahl, S. M.; Xin, H.; Williamson, W.; Shao, G.; Karatay, D. U.; Hillhouse, H. W.; Ginger, D. S. *Nano Letters* **2014**, *14*, 6926.
(27) Redinger, A.; Mousel, M.; Wolter, M. H.; Valle, N.; Siebentritt, S. *Thin Solid Films* **2013**, *535*, 291.
(28) Kuo, D.-H.; Tsega, M. *Materials Research Bulletin* **2014**, *49*, 608.
(29) Rath, T.; Haas, W.; Pein, A.; Saf, R.; Maier, E.; Kunert, B.; Hofer, F.; Resel, R.; Trimmel, G. *Solar Energy Materials and Solar Cells* **2012**, *101*, 87.
(30) Collord, A. D.; Hillhouse, H. W. *Chemistry of Materials* **2015**, *27*, 1855.
(31) Tai, K. F.; Gunawan, O.; Kuwahara, M.; Chen, S.; Mhaisalkar, S. G.; Huan, C. H. A.; Mitzi, D. B. *Advanced Energy Materials* **2016**, *6*, 1501609.
(32) Duan, H.-S.; Yang, W.; Bob, B.; Hsu, C.-J.; Lei, B.; Yang, Y. *Adv. Funct. Mater.* **2013**, *23*, 1466.
(33) Hsu, W.-C.; Zhou, H.; Luo, S.; Song, T.-B.; Hsieh, Y.-T.; Duan, H.-S.; Ye, S.; Yang, W.; Hsu, C.-J.; Jiang, C.; Bob, B.; Yang, Y. *ACS Nano* **2014**, *8*, 9164.
(34) van Embden, J.; Chesman, A. S. R.; Della Gaspera, E.; Duffy, N. W.; Watkins, S. E.; Jasieniak, J. J. *J. Am. Chem. Soc.* **2014**, *136*, 5237.
(35) van Embden, J.; Chesman, A. S. R.; Jasieniak, J. J. *Chemistry of Materials* **2015**, *27*, 2246.
(36) Liu, Y.; Yao, D.; Shen, L.; Zhang, H.; Zhang, X.; Yang, B. *Journal of the American Chemical Society* **2012**, *134*, 7207.
(37) Ou, K.-L.; Fan, J.-C.; Chen, J.-K.; Huang, C.-C.; Chen, L.-Y.; Ho, J.-H.; Chang, J.-Y. *J Mater Chem* **2012**, *22*, 14667.
(38) Lee, P.-Y.; Chang, S.-P.; Hsu, E.-H.; Chang, S.-J. *Solar Energy Materials and Solar Cells* **2014**, *128*, 156.
(39) Ji, S. L.; Shi, T. F.; Qiu, X. D.; Zhang, J.; Xu, G. P.; Chen, C.; Jiang, Z.; Ye, C. H. *Scientific reports* **2013**, *3*.
(40) Talapin, D. V.; Lee, J.-S.; Kovalenko, M. V.; Shevchenko, E. V. *Chemical reviews* **2010**, *110*, 389.
(41) Yin, Y.; Alivisatos, A. P. *Nature* **2005**, *437*, 664.
(42) Boles, M. A.; Ling, D.; Hyeon, T.; Talapin, D. V. *Nat Mater* **2016**, *15*, 141.
(43) Dierick, R.; Van den Broeck, F.; De Nolf, K.; Zhao, Q.; Vantomme, A.; Martins, J. C.; Hens, Z. *Chem. Mater.* **2014**, *26*, 5950.
(44) Bullen, C.; van Embden, J.; Jasieniak, J.; Cosgriff, J. E.; Mulder, R. J.; Rizzardo, E.; Gu, M.; Raston, C. L. *Chemistry of Materials* **2010**, *22*, 4135.
(45) Wei, Y.; Yang, J.; Lin, A. W. H.; Ying, J. Y. *Chemistry of Materials* **2010**, *22*, 5672.
(46) Haas, W.; Rath, T.; Pein, A.; Rattenberger, J.; Trimmel, G.; Hofer, F. *Chemical communications* **2011**, *47*, 2050.
(47) Ji, S.; Shi, T.; Qiu, X.; Zhang, J.; Xu, G.; Chen, C.; Jiang, Z.; Ye, C. *Sci. Rep.* **2013**, *3*.
(48) Jiang, C.; Liu, W.; Talapin, D. V. *Chemistry of Materials* **2014**, *26*, 4038.

CHAPTER 4: LIGAND-EXCHANGED CZTS NANOCRYSTAL THIN FILMS: DOES NANOCRYSTAL SURFACE PASSIVATION EFFECTIVELY IMPROVE PHOTOVOLTAIC PERFORMANCE?[4]

4.1 Overview

Nanocrystal (NC) Cu_2ZnSnS_4 (CZTS) solar cells, composed of a non-toxic and earth abundant absorber material, have great potential in low-cost solar energy harvesting. However, CZTS NC films typically must be thermally annealed at elevated temperatures and under harsh environments in order to produce high efficiency devices. The efficiencies of unannealed CZTS NC solar cells have been hampered by low open circuit potentials (V_{oc}, < 325 mV) and low short circuit current densities ($J_{sc,}$ < 2 mA), primarily due to the incomplete passivation of the crystal surface. Although great progress has made in understanding the surface chemistry of II-VI and IV-VI semiconductor NCs, the surface chemistry of complex quaternary CZTS NCs is largely unexplored. Here, for the first time, we report a comprehensive study of the surface chemistry of CZTS NCs focusing on depositing ligand-passivated, uniform NC thin films to address the issue of large V_{oc} deficit and low current-collection efficiency typically observed for CZTS NC solar cells. The ligand-exchange reactions were rationally designed to target each metal ion on the

[4] This chapter has been adapted by Max B. Braun from a publication in *Chemistry of Materials* **2017**, *29*, 6621-6629 and is available online at http://dx.doi.org/10.1021/acs.chemmater.7b00541. Synthesis, deposition, characterization, device fabrication, testing, and manuscript preparation were performed by both Lasantha Korala, and Max B. Braun. Assistance with syntheses and device fabrication steps and devlopment was provided by Jason M. Kephart and Zoe Tregillus. We kindly acknowledge Kevan C. Cameron at CSU Next Generation PV Center (NGPV) for providing substrates for solar cell fabrication and Professor James Sites (Department of Physics, Colorado State University) for solar cell measurements. Amy L. Prieto offered valuable insight, direction, and aided in the manuscript preparation.

surface (using both organic L-type ligands such as ethylenediamine, and inorganic X-type ligands (I^-, S^{2-})) and to passivate anionic chalcogen sites with inorganic Z-type ligands ($ZnCl_2$). Herein, we show that CZTS/CdS heterojunction NC solar cells made of uniformly passivated CZTS NCs demonstrate a more than 180 mV improvement in V_{oc}. Furthermore, the influence of device configuration on collection efficiency of photogenerated carriers in the CZTS NC absorber layer is presented and the implications of both surface and internal defects in CZTS NCs to photovoltaic performance are discussed.

4.2 Introduction

Solar cells are one of the most important renewable-energy technologies that have the potential to fulfill the terawatt-scale energy demand. Although crystalline wafer-based silicon solar cells are the overwhelming majority of the current global solar-cell market share, thin-film solar-cell technologies are under intense development and investigation, motivated by the goal of fabricating low cost and highly efficient solar cells.[1] Compounds such as CdTe and $CuIn_xGa_{1-x}Se_2$ (CIGS) have been used in mature thin-film solar-cell technologies that show promising efficiencies (>20%)[2] but the toxicity of Cd and scarcity of In may hinder mass production. Recently Cu_2ZnSnS_4 (CZTS) has immerged as an attractive alternative to CIGS due to its non-toxic and earth abundant elemental composition, and its suitable optical properties for solar energy harvesting.[3]

Solution processed deposition methods stand out among a variety of techniques that have been developed to deposit CZTS-based absorber layer owing to the enabling of the fabrication of low-cost solar cells by high-throughput roll-to-roll manufacturing. Hydrazine-processed $Cu_2ZnSn(S,Se)_4$ solar cells hold the current record efficiency (12.6%)[4] and, alternatively, CZTS nanocrystal (NC)-based inks and molecular inks have been successfully utilized to fabricate solar cells with over 8% [5, 6, 7] and 10%[8, 9] efficiency respectively, avoiding the use of highly reactive

and explosive hydrazine. Solution-phase synthetic routes can be utilized to prepare CZTS NCs, and these techniques allow the distinct advantage of convenient tuning of composition and phase before deposition of the films.[10] However, the aforementioned efficiencies were achieved at the cost of annealing the as-deposited NC films at high temperatures under selenium atmosphere (selenization) in which NCs are sintered to form larger grains. The elimination of the post-annealing step is highly advantageous for decreasing the manufacturing cost of solar cells, yet challenging as the highest efficiency reported thus far is only 0.23% for CZTS/CdS heterojunction NC solar cells without any post-annealing treatment.[11]

Deposition of thin films with well passivated surfaces and electronically coupled NCs is critical in solar-cell fabrication for the efficient extraction of photogenerated charge carriers. Surface ligand chemistry plays a vital role in achieving this goal. Tremendous progress has been made in recent years in exchanging long, insulating native ligands (NLs) with shorter organic or inorganic ligands in order to decrease the inter-NC distance and passivate the surface trap states effectively.[12] Solution-phase ligand exchange has shown remarkable success for II-VI and IV-VI binary chalcogenide NCs,[13] and solar cells with reasonable efficiency have been fabricated from ligand-exchanged PbS NC inks in a single-step deposition process.[14] Solid-phase ligand exchange has also been effectively utilized to deposit NC thin films for solar cells through a layer-by-layer approach, and iodide-passivated PbS NC solar cells have shown the highest certified efficiency (10.6 %)[15] and best device stability without any heat treatment.[16] In 2009, Steinhagen *et. al.* utilized as-synthesized CZTS NCs to fabricate substrate devices, which is the standard configuration for CZTS-based solar cells, without any surface ligand treatment.[11] The devices showed low efficiency (0.23 %) and incomplete surface passivation, and large inter-NC distances were believed to contribute to poor photovoltaic performance (V_{oc} = 321 mV and J_{sc} = 1.95 mA).

Recently, Suehiro *et. al.* has employed ligand stripping strategies to improve charge transport in CZTS NC films and devices have been fabricated in the superstrate configuration without much success.[17] Surprisingly, the well established ligand chemistry of II-VI and IV-VI binary chalcogenide NCs has not yet been applied to develop methods to deposit high quality thin films composed of electronically connected and completely-passivated CZTS NCs.[18]

In this report, for the first time, we performed a comprehensive study to determine the best ligand exchange strategies for the deposition of uniform and fully surface-passivated CZTS NC films. Inorganic atomic-ligand, small organic-ligand, and hybrid-ligand passivation were explored to obtain complete surface coverage by considering the type of ligand exchange reaction (X, L, and/or Z) and surface site (cationic or anionic) in the film deposition process. Specifically, attention was paid to the chemical differences expected between Cu (I), Zn (II) and Sn (IV) cationic sites. FT-IR spectroscopy was utilized to monitor the ligand exchange and the optical properties of CZTS NC films were characterized by employing UV-vis-NIR spectroscopy. The modifications of the NC surface after ligand exchange were probed by XPS spectroscopy and the electrical properties of the NC films were evaluated by Hall effect measurements. The V_{oc} of the CZTS/CdS heterojunction solar cells varied in agreement with the extent of surface passivation, and a more than 180 mV enhancement in the V_{oc} was obtained for devices in which surface sites were fully passivated with X, L and Z type ligands.

4.3 Experimental section

4.3.1 Materials

Copper(II) acetylacetonate (99.99+%), zinc acetate (99.99%), tin(II) chloride dihydrate (99.99%), sulfur powder, zinc chloride (≥98%), oleylamine (OLA) (70%), tetrabutylammonium iodide (TBAI) (98%), cadmium sulfate (≥99.99%), thiourea (≥99.0%), (ethylenediamine (EDA)

(ReagentPlus, ≥99%), ammonium hydroxide (28.0-30.0% NH_3 basis), and ammonium sulfide (20 % wt. in water) were purchased from Sigma Aldrich. Se (99.99%) was purchased from Strem Chemicals. ACS grade formamide (FA), chloroform, methanol, acetonitrile, ethanol, and hexanes were obtained from Fisher Scientific.

4.3.2 Synthesis of Cu_2ZnSnS_4 (CZTS) nanocrystals (NCs)

CZTS NCs were synthesized following the method published by Steinhagen et al.[11] In a typical reaction, 0.52 g (2 mmol) of copper (II) acetylacetonate, 0.29 g (1.6 mmol) of zinc acetate, 0.18 g (0.8 mmol) of tin (II) chloride dihydrate, 0.13 g (4.0 mmol) of sulfur, and 40 mL of OLA were added to a 100 mL three-neck flask and degassed under vacuum for two hours. The reaction mixture was then purged with nitrogen for 30 min at 110 °C and then heated to 280 °C. The NCs were grown for one hour and then cooled to room temperature. As-synthesized NCs were purified by precipitation with ethanol and followed by centrifugation. The precipitate was redispersed in chloroform and centrifuged again to remove unreacted precursors and large agglomerates. This procedure was repeated one more time and the final dispersion was precipitated with ethanol. The purified NCs were dried under vacuum and stored in a nitrogen glove box for further use.

4.3.3 Characterization

X-ray diffraction (XRD) was performed on a Scintag X-2 Advanced Diffraction system equipped with Cu Kα radiation (λ = 1.54 Å). Low-resolution transmission electron microscope (TEM) analysis was carried out on a JEOL JEM 1400 TEM operated at an accelerating voltage of 100 keV. High-resolution TEM images and selected area electron diffraction (SAED) patterns were obtained with a JEOL JEM 2100F TEM operated at an acceleration voltage of 200 keV. Semi-quantitative elemental analysis of NC samples was obtained with a JEOL JSM 6500F FE-SEM equipped with an EDAX Genesis energy dispersive spectroscopy detector. Thermo

gravimetric analysis (TGA) measurements were performed on a TA Instruments TGA 2950 thermogravimetric analyzer under nitrogen flow. The temperature of the NC samples (5-10 mg) was increased up to 600 °C at a rate of 10 °C/min. The absorption spectra were obtained with a Cary 500 UV-vis-NIR spectrophotometer on the NC dispersions and ATR FT-IR spectra were obtained using a Thermo Scientific Nicolet 380 on the dried NC powder. The X-ray photoelectron spectroscopy (XPS) spectra were obtained using a Physical Electronics ESCA 5800 system with monochromatic Al K_{α} (E = 1486.6 eV) X-ray source. High-resolution scans were performed with a pass energy of 23.5 eV and a step size of 0.10 eV/step. Data was processed using Multipak software, version 9.3.03. All spectra were shifted using inorganic carbon as a reference at 284.80 eV.

4.3.4 Solution-phase ligand exchange

In order to exchange native ligands (NLs) with S^{2-} anions, NC dispersions in chloroform (10 mg/mL) were mixed with a solution of $(NH_4)_2S$ (1 mL of ammonium sulfide in 14 mL of FA) and the mixture was stirred for two hours and then allowed to phase separate. The NCs were transferred to the FA phase leaving a clear chloroform layer indicative of a successful ligand exchange. The chloroform layer was removed and fresh chloroform was added to the FA phase, and then the mixture was vigorously shaken to remove residual organic ligands from the FA phase. This process was repeated three more times, and acetonitrile was added to the FA phase to precipitate the S^{2-}-capped NCs followed by centrifugation. The isolated NCs were washed with acetonitrile one more time to remove excess S^{2-} anions and dried under vacuum. The ligand exchange was performed under ambient conditions and the dried NCs were stored in a nitrogen glove box for further use.

4.3.5 Solid-phase ligand exchange and thin-film deposition

The glass substrates were cleaned by sonication first in soapy water, then isopropanol, and finally in DI water for 15 minutes. The substrates were stored in fresh DI water after final sonication and blow-dried with nitrogen before film deposition. The films were fabricated by layer-by-layer dip coating using a mechanical dip coater. In a typical deposition, the substrates were first dipped in a NC solution (6.5 mg/mL in hexane) and then in a ligand exchange solution(s), and finally in fresh acetonitrile solution to complete one cycle. Then, 1mM of ammonium sulfide, 20 mM of TBAI, 11 mM of EDA, or 20 mM of TBAI and 22 mM of zinc chloride in methanol were used as ligand exchange solutions. This process was repeated to deposit films with 100-150 nm thickness, as measured by profilometry. Native ligand (NL)-capped CZTS NC films were deposited by drop casting hexane dispersions of NCs onto the glass substrates.

4.3.6 Thin film characterization

UV-vis-NIR and XPS spectroscopy was performed on as-deposited NC films as described previously. FT-IR spectra of NC films were obtained in transmission mode and spectra were normalized according to the fraction of the highest peak absorption in the smaller wavelength region. The electrical properties of NC films were obtained by Hall effect measurements with an Ecopia HMS-3000 system on van der Paw geometry. Finally, Au paste was used to create ohmic contacts on NC film.

4.3.7 Device fabrication and measurements

Fluorine-doped tin oxide (FTO) glass substrates coated with a CdS buffer layer (~130 nm) by close space sublimation[19] were used for superstrate device fabrication. The substrates were first dipped in NC solution (6.5 mg/mL), ligand exchange solution(s), and then acetonitrile as described before, until a desired film thickness was achieved. Gold electrodes (~250 nm) were deposited on

to the NC layers (~250 nm) by thermal evaporation at the base pressure of 1×10^{-6} Torr through a shadow mask. The device area was 0.5 cm^2. Additionally, chemical bath deposition was employed to deposit CdS buffer layer (~30 nm)[11] to fabricate superstrate devices and a i-ZnO window layer (~80 nm) was coated on FTO glass substrates by RF sputtering before CdS deposition. Mo-sputtered (~500 nm) glass substrates were used to deposit ligand-exchanged NC films for substrate devices. The CdS buffer layer (~30 nm) was deposited by chemical bath deposition followed by RF sputtering of i-ZnO (~400 nm) and ZnO:Al as window layer and top contact (~150 nm) through a shadow mask with a device area of 0.5 cm^2 respectively. Current density-voltage $(J-V)$ characteristics were recorded using a Keithley 2401 source meter under a solar simulator with standard-test conditions (A.M. 1.5 Global spectrum with 100 mW cm^{-2} intensity) at 25 °C. External quantum efficiency (EQE) measurements were performed as described elsewhere.[20] Average photovoltaic parameters were obtained from more than 10 devices

4.4 Results and Discussion

The CZTS NCs were synthesized by following a one-pot heating up procedure published by Steinhagen *et. al.*[11] where technical grade oleylamine (OLA) was used as solvent, and the as-synthesized NCs were purified by multiple washing steps using chloroform and ethanol as solvent and antisolvent, respectively (see experimental the section for details). The purified NCs were fully characterized using a wide array of microscopic, spectroscopic and scattering techniques. Figure 4.1a shows a low-resolution transmission electron microscope (TEM) image of CZTS NCs with an average size of 10.4 ± 2.3 nm. The CZTS NCs are highly crystalline as indicated by the high-resolution TEM image (Figure 4.1b) of a single CZTS NC, and the structure matches the kesterite phase of CZTS (PDF # 00-026-0575) as evidenced by the diffraction spots in the selected area diffraction (SAED) pattern (Figure 4.1c) that correspond to the (112), (220) and (312) planes. X-

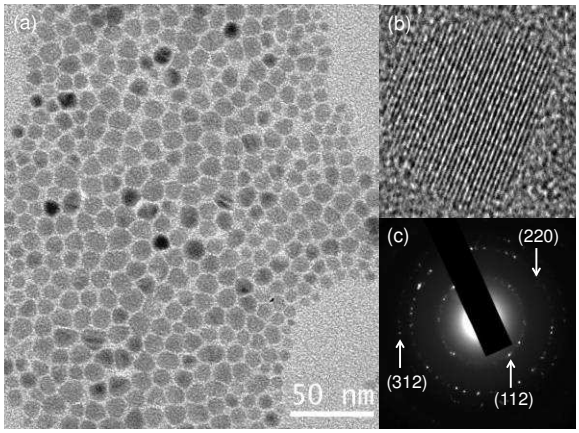

Figure 4.1. (a) Low-resolution and (b) high-resolution TEM images, and (c) SAED pattern of CZTS NCs.

ray diffraction (XRD) analysis of CZTS NCs further confirmed the kesterite structure (Figure S4.1) and according to energy-dispersive X-ray spectroscopy (EDS) elemental analysis, the average composition of CZTS NCs was found to be $Cu_{1.2}Zn_{1.4}Sn_1S_{4.7}$ (Cu/(Zn+Sn)≈0.9 and Zn/Sn≈1.4).

Initially we sought to explore the solution-phase ligand exchange strategies for NL-capped CZTS NCs since the use of inks composed of smaller inorganic ligand-capped NCs enables the deposition of densely packed NC films in a single processing step.[21, 22] Among inorganic ligands, S^{2-} anions have been used to perform solution-phase ligand exchange for CZTS NCs,[23, 24] and accordingly, we replaced NLs with S^{2-} via a biphasic ligand exchange reaction (Scheme 4.1). Briefly, NL-capped CZTS NCs were dispersed in chloroform and then mixed with ammonium sulfide in formamide (FA), and mixture was stirred vigorously for 30 minutes resulting in the transformation of S^{2-} capped CZTS NCs to the FA phase (see experimental section for details). Thermogravimetric analysis (TGA) and FT-IR spectroscopy were performed on purified and dried NCs to determine the efficiency of ligand exchange reaction. The TGA curves of organic and inorganic ligand-capped NCs exhibited different decomposition paths suggesting successful ligand

Scheme 4.1. Illustration of (a) solution-phase and (b) solid-phase ligand exchange methods

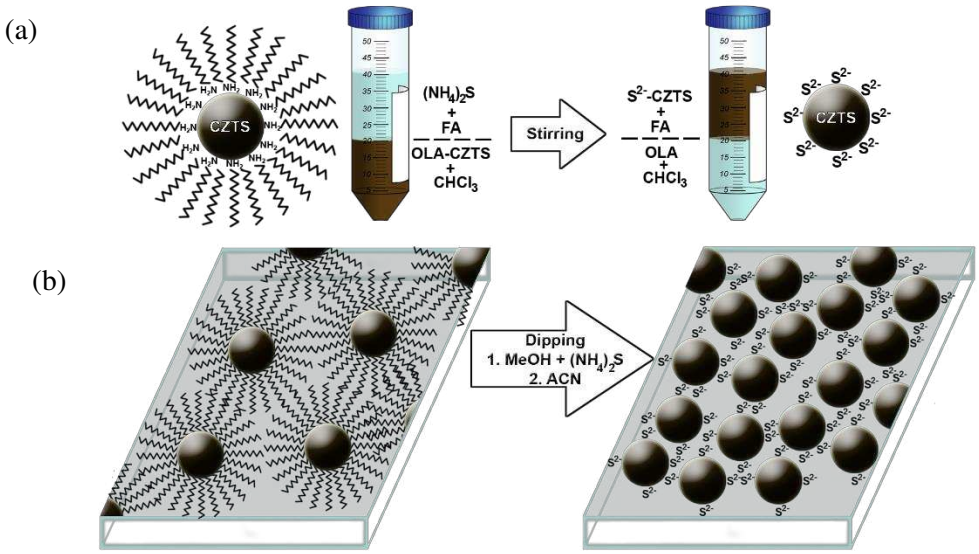

exchange (Figure S4.2a). The TGA curve of NL-capped CZTS NCs showed ~10% weight loss at 600 °C, whereas S^{2-}-capped NCs displayed only a ~5% decrease in weight indicative of replacement of majority of organic molecules with inorganic anions. The observed C-H stretching vibrations (3000-2800 cm-1) mostly disappeared after S^{2-} exchange as shown in FTIR spectra of NL- and S^{2-}-capped CZTS NCs (Figure S4.2b), confirming the presence of only a very low amount of residual organic ligands. We then investigated methods of depositing S^{2-}-capped CZTS NC films for electrical property measurements and solar cell fabrication. The dried S^{2-}-capped CZTS NCs were dispersed in the polar FA solvent and dimethyl sulfoxide (DMSO), and the resulting NC dispersions were used to deposit films by both spin casting and drop casting. Unfortunately, we could not deposit uniform films with appreciable thickness by spin coating from either dispersions due to the low volatility of FA and DMSO. In order to deposit films by drop casting, it was necessary to heat the substrate to evaporate the solvents and this consequently resulted in very uneven films. The low volatility of FA and DMSO also eliminates the possibility of using

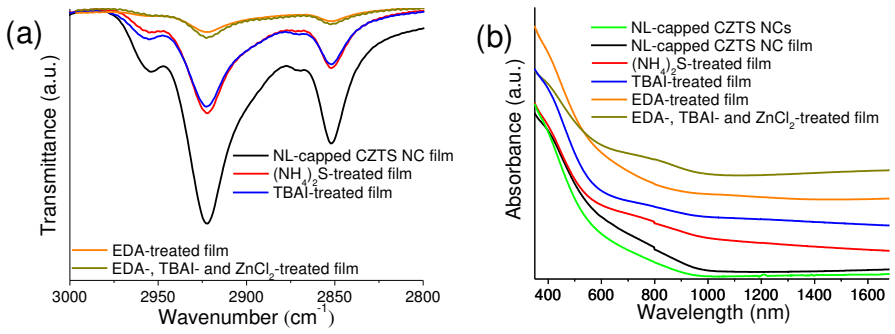

Figure 4.2. (a) FT-IR spectra of CZTS NC films, and (b) UV-vis-NIR spectra of CZTS NCs and films.

spray coating to deposit films without heating the substrate.[25] Overall, the necessity of having to use low-volatile polar solvents to produce S^{2-}-capped CZTS NC dispersions makes it challenging to deposit uniform films with substantial thickness without applying pre- or post-heating treatments.

This lead us to investigate solid-phase ligand exchange strategies that have also been successfully utilized to fabricate iodide-passivated PbS NC thin films and solar cells. [16,21,26] First we examined both S^{2-} and I^- as inorganic ligands to replace the native NLs. The ligand-exchanged NC films were deposited by layer-by-layer dip coating technique using a mechanical dip coater. In order to deposit a layer of CZTS NCs, cleaned glass substrates were dipped into CZTS NC solution in hexane, and then into the ligand exchange solution (ammonium sulfide or tetrabutylammonium iodide (TBAI) in methanol) followed by rinsing in acetonitrile (see the experimental section for details). This process was repeated until the desired film thickness was achieved. Figure 4.2a shows FT-IR spectra of a NL-caped CZTS NC film deposited by drop casting and different ligand-treated NC films. Interestingly, only a partial exchange was observed after solid-phase S^{2-} or I^- ligand exchange as indicated by only ~50 % reduction in C-H stretching

signal, while near complete exchange was taken place in solution-phase inorganic ligand exchange.

This disparity in ligand exchange efficiency could be explained by considering the types of the ligands involved in the exchange reaction. It can be assumed that CZTS NC surface is originally passivated by both L-type OLA and X-type impurities that are present in the technical grade OLA.[27] In the case of a biphasic ligand exchange reaction, X-type S^{2-} anions can be exchanged for X-type impurities and L-type OLA can be replaced by the $[S]^{2-}2[NH_4]^+$ ion pair where the quaternary ammonium cation is stabilized in the highly polar formamide solvent ($\varepsilon \approx 106$).[28] However, solid-phase ligand exchange was performed in the relatively weakly polar solvent methanol ($\varepsilon \approx 33$) that cannot efficiently facilitate the adsorption of $[S]^{2-}2[NH_4]^+$ or $[I]^-[TBA]^+$ ion pair on the surface cation sites efficiently due to the inability to stabilize the quaternary ammonium cation. It is likely that mostly X-type impurities along with some L type ligands are replaced by the S^{2-} or I^- in the solid-phase ligand exchange. Furthermore, it was found that the use of neat FA, or a mixture of FA and methanol as the solvent did not change the outcome significantly. This is not the case for typical oleic acid-capped PbS NCs, where X-type oleic acid can be efficiently exchanged with X-type anions, and the complex formed between deprotonated oleic acid and $[TBA]^+$ can be removed in the rinsing step.[29]

In order to overcome the problems with the L-type OLA exchange, we examined the use of ethylenediamine (EDA) to replace the OLA with a shorter L-type ligand. Successful EDA exchange was confirmed by the ~90 % reduction of C-H stretching signal in the FT-IR spectrum of EDA-treated NC film (Figure 4.2a). As a logical next step, both L-type and X-type ligands bound to CZTS NC surface were exchanged by performing two-step ligand treatment (EDA and S^{2-}) in the dipping process. We also investigated the possibility of using $ZnCl_2$ as a Z-type ligand

to passivate the surface anion sites. Accordingly, L-type (EDA), and then X- and Z-type (TBAI and $ZnCl_2$) ligand exchanges were carried out in the film deposition in order to cover all possible surface sites on the CZTS NCs. Figure 4.2b shows UV-vis-NIR spectra of a hexane dispersion of NL-capped NCs and NC thin films deposited with and without ligand exchange. All the films have more or less similar optical properties and changes in the baseline could be due to variations in the dielectric environment.

We performed X-ray photoelectron spectroscopy (XPS) on the NC films in order to explore the surface changes in CZTS NCs after various ligand exchange processes. High-resolution XPS analysis of NL-capped CZTS NC films (Figure 4.3a and S4.3) confirmed the presence of the oxidation states of Cu (I) (2p3/2: 952.1 eV), Zn (II) (2p3/2: 1022 eV), Sn (IV) (3d3/2: 494.8 eV), and S (II) (2p3/2: 161.7).[30] The iodide surface passivation was revealed by the appearance of significant I 3d signal in both TBAI- and TBAI/$ZnCl_2$-treated films, as shown in Figure 4.3b. However, mixed-ligand treatments caused a very small shift of the I 3d peaks towards higher biding energy values as a consequence of small changes in the oxidation environment. Both sulfide- and iodide-passivated NC films showed very little to no change in the S 2p peak, although a small broad peak was observed in the higher binding energy region (167-169 eV) of the XPS spectrum for sulfide-passivated NC film indicating the presence of sulfate on the NC surface (Figure 4.3a).[31] The TBAI/$ZnCl_2$ treatment noticeably shifted the S 2p peak towards higher binding energies, and this could be caused by the change in the oxidation state of surface S^{2-} sites as a result of the electron donation to the $ZnCl_2$ acceptor ligand. The presence of $ZnCl_2$ on the NC surface was confirmed by detection of the Cl 2p peak signal in TBAI/$ZnCl_2$-treated film (Figure S4.3d). We evaluated the charge transport properties of ligand-exchanged NC films by Hall effect measurements; carrier concentration (n) and conductivity (σ) of different ligand-treated NC films

Table 4.1. Average Electrical Properties of ligand treated-NC films.

CZTS NC Film	**Carrier Concentration (cm^{-3})**	**Conductivity (Scm^{-1})**
$(NH_4)_2S$-treated	$2.7 \pm 3.9 \times 10^{15}$	$1.4 \pm 0.4 \times 10^{-3}$
TBAI-treated	$5.5 \pm 6.7 \times 10^{14}$	$6.0 \pm 2.6 \times 10^{-4}$
EDA-treated	$1.0 \pm 0.4 \times 10^{16}$	$1.8 \pm 0.4 \times 10^{-3}$
EDA- and $(NH_4)_2S$-treated	$2.1 \pm 2.5 \times 10^{17}$	$1.1 \pm 0.8 \times 10^{-2}$
EDA-, TBAI-, and $ZnCl_2$-treated	$3.3 \pm 1.9 \times 10^{17}$	$9.4 \pm 0.4 \times 10^{-3}$

(thickness 100-150 nm) were obtained usinga Ecopia HMS-3000 Hall measurement system (Table 4.1). The average carrier concentration of ligand-treated NC films increased in the order of $I^- < S^{2-} < EDA < EDA/S^{2-} \approx EDA/I^-/ZnCl_2$. Because of the complexity of CZTS NC surface, it is difficulty to rationalize the variation in carrier concentration after different ligand treatments. The average conductivities of NC films followed the same trend except in the case of sulfide passivation. The $(NH_4)_2S$-treated films showed similar conductivity to that of EDA-treated films although with an order of magnitude lower carrier concentration.

Finally, we fabricated CZTS/CdS heterojunction NC solar cells in superstrate configuration. The CdS buffer layer (~120 nm) was deposited on FTO glass substrates by sublimation and CZTS NC films (~250 nm) were deposited as described previously (see Experimental section for more details) followed by thermal evaporation of Au (~250 nm) through a shadow mask with a device area of 0.5 cm^2. Figure 4.4 shows a cross-sectional SEM image (Inset of Figure 4.4f) of a cell (Glass/FTO/CdS/CZTS/Au), and dark and light current-voltage curves of champion solar cells fabricated from I^--, S^{2-}-, EDA-, EDA/S^{2-}-, EDA/I^-/$ZnCl_2$-capped CZTS NC films along with cell parameters and efficiencies. The V_{oc} values of all the cells fluctuated through a reproducibly small range (<10 mV). As we expected, the measured V_{oc} varied with the type of ligand treatment. More importantly, changes in the V_{oc} were clearly correlated with the extent of ligand coverage on the NC surface because unpassivated surface sites act as recombination centers and lead to a decrease in V_{oc}.

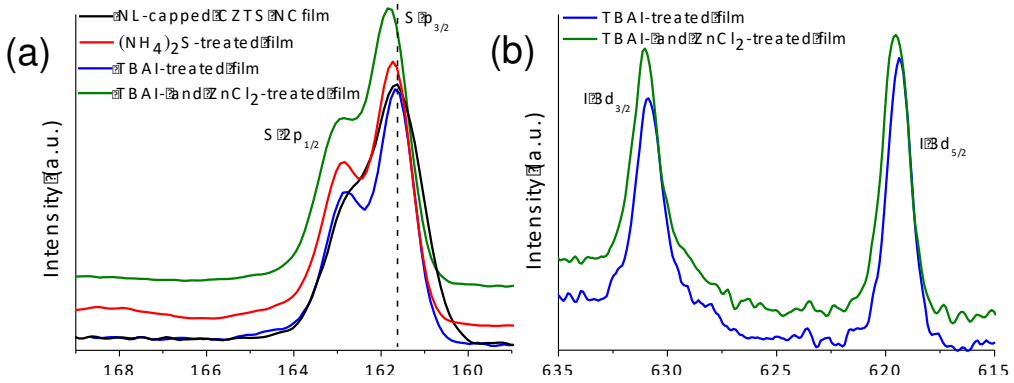

Figure 4.3. High-resolution XPS spectra of (a) S 2p and (b) I 3d core levels of CZTS NC films.

The S^{2-}- and I^--passivated CZTS NC solar cells, in which X-type surface ligation occurred, exhibited an average V_{oc} of 581 $\pm$ 6 mV and 599 $\pm$ 6 mV respectively, indicating that I^- provides slightly better surface passivation compared to S^{2-}. The EDA-passivated CZTS NC solar cell yielded a V_{oc} of 623 $\pm$ 9 mV, which is higher than that of the X-type ligand-passivated cells. As mentioned earlier, NLs on the CZTS NC surface primarily consisted of the L-type OLA. These bulky ligands can be efficiently exchanged with L-type short EDA molecules. The better surface coverage provided by the efficient exchange of the compact EDA ligands could have caused this increase in V_{oc}. Hybrid passivation provided by both EDA and S^{2-} exchange resulted in a significantly further increase in V_{oc} to 674 $\pm$ 7 mV, which can be attributed to the efficient exchange of both L-type and X-type bulky NLs on the CZTS NC surface for compact L-type and X-type Ligands. The highest average V_{oc} (686 $\pm$ 6 mV) was obtained for EDA/I^-/$ZnCl_2$-passivated cells in which complete surface coverage was achieved by efficiently passivating both cation sites (in all of their complexity, considering the three different cations possible) and anion sites by

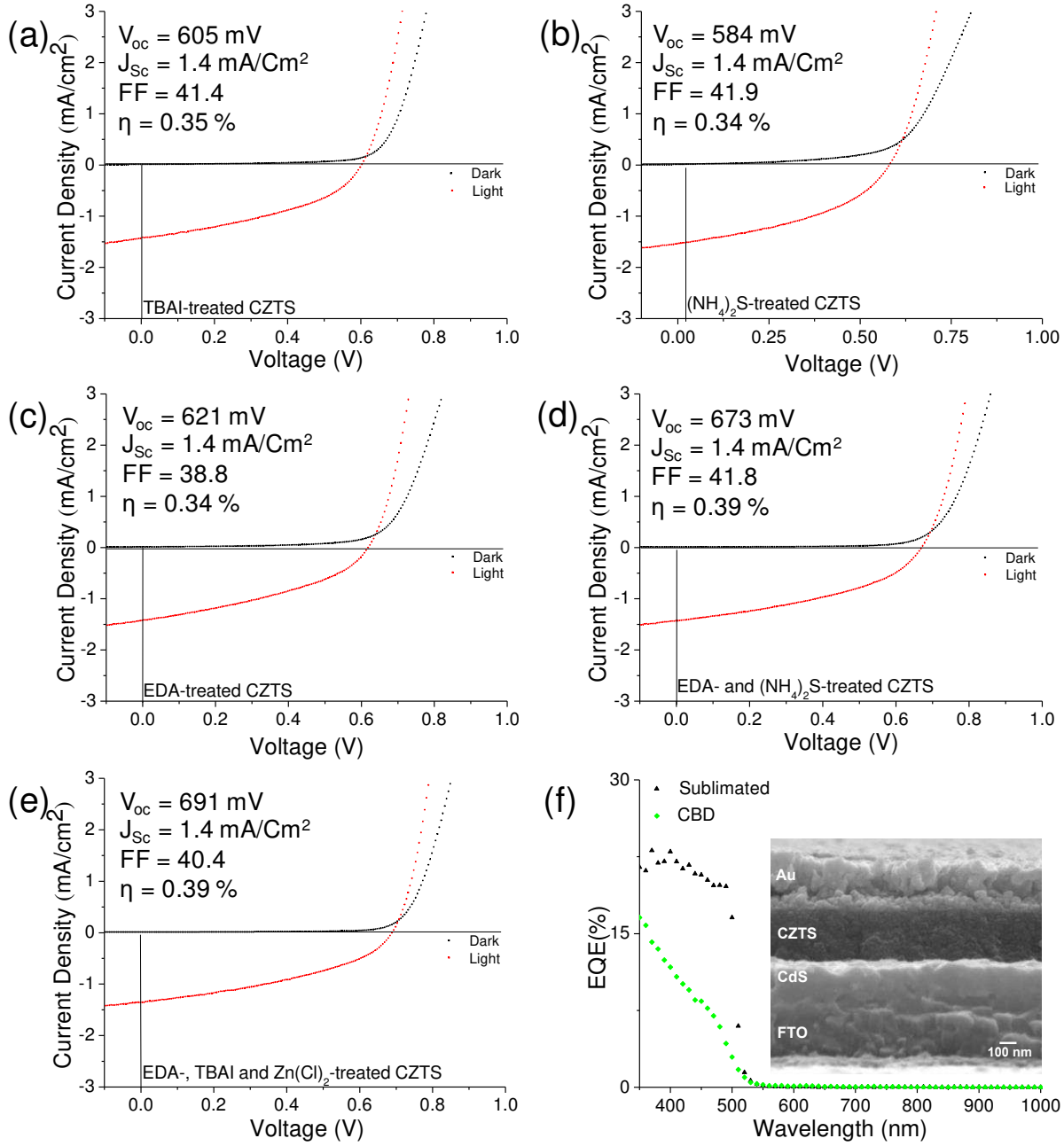

Figure 4.4. The current-voltage characteristics of the champion cells fabricated from (a) I^--capped, (b) S^{2-}-capped, (c) EDA-capped, (d) EDA/S^{2-}-capped, and (e) EDA/ I^-/S^{2-}-capped CZTS NC films. (f) EQE spectra of superstrate devices constructed from EDA/ I^-/S^{2-}-capped CZTS NC films and sublimated CdS or CBD-deposited CdS buffer layers. The inset shows SEM cross-sectional image of the device e.

compact ligands. In contrast, solar cells fabricated from NL-capped CZTS NC films, which were deposited by drop casting, yielded fairly low V_{oc} indicative of incomplete surface passivation

(Figure S4.4). This is, to our knowledge, the highest reported V_{oc} for CZTS NC based solar cells. All of the champion ligand-passivated cells exhibited similar J_{sc} (1.4 mA/Cm^2) and fill factors (FF: 40-42%) although dark conductivities of different ligand-treated CZTS NC films showed considerable fluctuations according to the Hall measurements. Interestingly, as indicated in Figure 4.4e, the EQE spectral response of a fully passivated solar cell reveals that contribution to the extracted photocurrent solely comes from the excitons generated in the depletion region of the CdS buffer layer via ultraviolet photon absorption that we also mistakenly identified as current originated from absorber layer in a previous sudy.[32] All the other ligand passivated-devices exhibited similar behavior and this explains the observed similar current densities for all the champion devices regardless of the variation of dark conductivity in absorber layers. Typically, an optimal spike-like conduction band offset (<0.4 ev) is present at the CZTS/CdS heterojunction[33, 34, 35] in which CdS is deposited by chemical bath deposition (CBD). Since band alignment at the heterojunction interface depends on the processing conditions, we think that the conduction band offset exists at the heterojunction formed by the CZTS NC and sublimated CdS layers, and possesses an unfavorably large spike. This electrical barrier blocks the photogenerated electron collection from the absorber layer, while holes photogenerated in the CdS layer are collected and transported through the NC absorber. As expected, decrease of CdS thickness lowered the photocurrent and overall solar cell performance as a result of reduced absorbance in the buffer layer.

Next, we explored deposition of a thinner CdS layer by CBD, which is the most common method employed in the fabrication of CZTS-based solar cells. The thinner CBD-CdS films (20-80 nm) decrease light absorption in the buffer layer, and provide favorable band alignment and large carrier density, thus enhancing carrier collection in both short- and long- wavelength

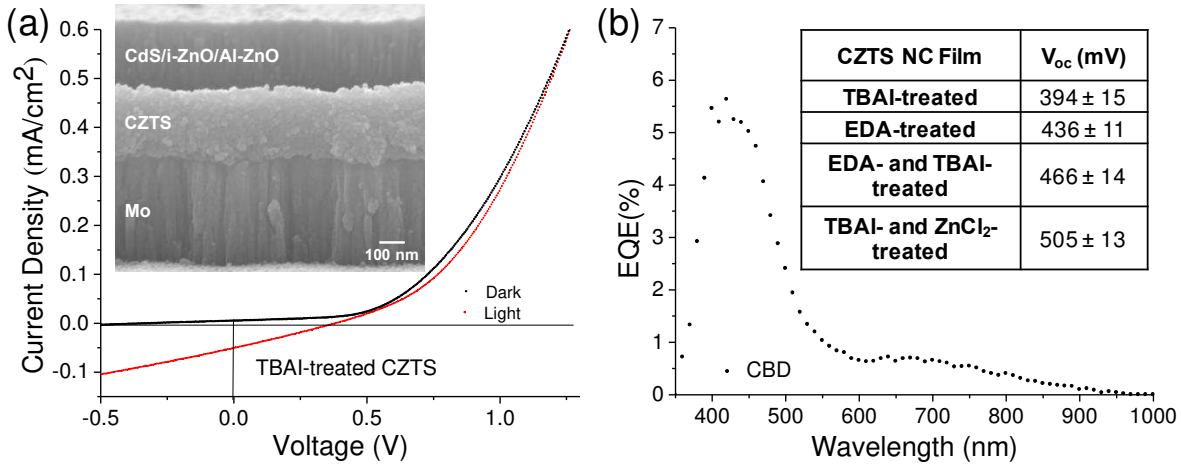

Figure 4.5. (a) The current-voltage characteristics and (b) EQE spectrum of a solar cell with CBD-deposited CdS buffer layer fabricated from I^--capped CZTS NC film in substrate configuration. The insets of figure (a) and (b) show SEM cross-sectional image of the device and average V_{oc} values of solar cells fabricated from different ligand capped-NC films respectively.

regions.[36] Initially, we fabricated devices with CBD-CdS buffer layers (~30 nm) in superstrate configuration. However, photocarriers generated in the absorber layer were still not extracted, as displayed in the EQE spectrum of a fully passivated device (Figure 4.4f). Then we switched to substrate configuration, which is the standard device architecture for CIGS and CZTS-based solar cells. Accordingly, Mo-coated glass substrates were used to deposit the ligand-treated CZTS absorber layer, followed by the CBD-CdS buffer layer, and finally the intrinsic/Al-doped ZnO bilayer. The inset of Figure 4.5a shows cross-sectional image of a substrate device (Glass/MO/CZTS/CdS/i-ZnO/ZnO:Al).

In addition to optimal band alignment, CBD deposition of CdS onto CZTS absorber layer allows epitaxial growth and the creation of buried homojunction due to diffusion of Cd^{2+}, reducing interfacial recombination losses.[36, 37] Accordingly, we were able to fabricate functioning devices with CZTS NC films as the active-light absorber layer confirmed by the EQE spectra in Figure 4.5b. However, the EQE was extremely low throughout the spectrum under zero bias condition,

but slightly increased at long-wavelengths under reverse bias condition. Nevertheless, most importantly, the V_{oc} followed the same trend observed in the superstrate devices, confirming the success of surface passivation via ligand treatment (Inset of Figure 4.5b). In fact, the EDA/I^-/$ZnCl_2$-passivated cells showed a more than 180 mV increase in V_{oc} compared to substrate CZTS/CdS heterojunction NC solar cells fabricated by Steinhagen *et. al.* without ligand passivation.[11] However, our devices exhibited comparatively low current densities (Figure 4.5a). This is primarily due to high series resistance caused by an unoptimized ZnO:Al layer and back contact issues,[38] and absence of Ni/Al grids for comparatively high active area (0.5 cm^2 vs. 0.08 cm^2).

Although complete surface passivation was achieved via rational ligand treatment during the film deposition, NC devices showed significantly high V_{oc} deficit (~ 900 mV) compared to bulk devices,[39] indicating that the internal defects in quaternary CZTS NCs play a major role in dictating the photovoltaic performance. The reported sub-nanosecond charge recombination time (~20 ps) for CZTS NCs,40 combined with expected low mobility due to presence of large number of grain boundaries, severely limit the collection of photo-generated carriers in the absorber layer. Consequently, a drastic improvement of current density cannot be expected even with low series resistance devices without reducing internal defect density.

4.5 Conclusions

In summary, we have developed rational strategies of depositing uniform CZTS NC thin films with well-surface passivated and efficiently coupled NCs via ligand exchange for the fabrication of CZTS NC solar cells. A comprehensive study of surface ligand chemistry was performed to achieve full surface coverage in order to address the issue of surface-related recombination leading to lower V_{oc}. The rationality of the efficient ligand exchange was based on

the type of ligand exchange reaction and accordingly, L-type and X-type bulky NLs on the NC surface were successfully replaced with small organic molecules (EDA) and inorganic anions (I^-, S^{2-}). These compact ligands more efficiently passivate the surface defects and greatly reduce the charge carrier recombination, thereby enhancing the V_{oc}. A record V_{oc} of 505 $\pm$ 13 mV for CZTS/CdS heterojunction NC solar cells was achieved by additional passivation the surface chalcogen sites via Z-type $ZnCl_2$, along with L-, and X-type passivation. Nonetheless, EQE measurements revealed extremely poor collection of photogenerated carriers from the absorber layer, signifying the dominating effects of intrinsic defects in quaternary CZTS NCs on the photovoltaic performance.

REFERENCES

(1) Jean, J.; Brown, P. R.; Jaffe, R. L.; Buonassisi, T.; Bulovic, V. *Energy Environ. Sci.* **2015**, *8*, 1200.
(2) da Conceição, M. O. T.; Brum, M. C.; dos Santos, D. S.; Dias, M. L. *J. Alloy. Compd.* **2013**, *550*, 179.
(3) Walsh, A.; Chen, S.; Wei, S.-H.; Gong, X.-G. *Adv. Energy Mater.* **2012**, *2*, 400.
(4) Wang, W.; Winkler, M. T.; Gunawan, O.; Gokmen, T.; Todorov, T. K.; Zhu, Y.; Mitzi, D. B. *Adv. znergy Mater.* **2014**, *4*, 1301465.
(5) Miskin, C. K.; Yang, W.-C.; Hages, C. J.; Carter, N. J.; Joglekar, C. S.; Stach, E. A.; Agrawal, R. *Prog. Photovolt: Res. Appl.* **2015**, *23*, 654.
(6) van Embden, J.; Chesman, A. S. R.; Della Gaspera, E.; Duffy, N. W.; Watkins, S. E.; Jasieniak, J. J. *J. Am. Chem. Soc.* **2014**, *136*, 5237.
(7) Hsu, W.-C.; Zhou, H.; Luo, S.; Song, T.-B.; Hsieh, Y.-T.; Duan, H.-S.; Ye, S.; Yang, W.; Hsu, C.-J.; Jiang, C.; Bob, B.; Yang, Y. *ACS Nano* **2014**, *8*, 9164.
(8) Werner, M.; Keller, D.; Haass, S. G.; Gretener, C.; Bissig, B.; Fuchs, P.; La Mattina, F.; Erni, R.; Romanyuk, Y. E.; Tiwari, A. N. *ACS Appl. Mater. Interfaces* **2015**, *7*, 12141.
(9) Larramona, G.; Levcenko, S.; Bourdais, S.; Jacob, A.; Choné, C.; Delatouche, B.; Moisan, C.; Just, J.; Unold, T.; Dennler, G. *Adv. Energy Mater.* **2015**, *5*.
(10) Zhou, H.; Hsu, W.-C.; Duan, H.-S.; Bob, B.; Yang, W.; Song, T.-B.; Hsu, C.-J.; Yang, Y. *Energy Environ. Sci.* **2013**, *6*, 2822.
(11) Steinhagen, C.; Panthani, M. G.; Akhavan, V.; Goodfellow, B.; Koo, B.; Korgel, B. A. *J. Am. Chem. Soc.* **2009**, *131*, 12554.
(12) Wang, R.; Shang, Y.; Kanjanaboos, P.; Zhou, W.; Ning, Z.; Sargent, E. H. *Energy Environ. Sci.* **2016**, *9*, 1130.
(13) Boles, M. A.; Ling, D.; Hyeon, T.; Talapin, D. V. *Nat Mater* **2016**, *15*, 141.
(14) Ning, Z.; Dong, H.; Zhang, Q.; Voznyy, O.; Sargent, E. H. *ACS Nano* **2014**, *8*, 10321.
(15) Lan, X.; Voznyy, O.; García de Arquer, F. P.; Liu, M.; Xu, J.; Proppe, A. H.; Walters, G.; Fan, F.; Tan, H.; Liu, M.; Yang, Z.; Hoogland, S.; Sargent, E. H. *Nano Lett.* **2016**, *16*, 4630.
(16) Chuang, C.-H. M.; Brown, P. R.; Bulović, V.; Bawendi, M. G. *Nat Mater* **2014**, *13*, 796.
(17) Suehiro, S.; Horita, K.; Kumamoto, K.; Yuasa, M.; Tanaka, T.; Fujita, K.; Shimanoe, K.; Kida, T. *J. Phys. Chem. C* **2013**, *118*, 804.
(18) Milliron, D. J. *Nat Mater* **2014**, *13*, 772.
(19) Kobyakov, P. S.; Moore, A.; Raguse, J. M.; Swanson, D. E.; Sampath, W. S. *J. Vac. Sci. Technol. A* **2014**, *32*, 021511.
(20) Kephart, J. M.; Geisthardt, R.; Sampath, W. S. In *Photovoltaic Specialists Conference (PVSC), 2012 38th IEEE* 2012, 854.
(21) Zhitomirsky, D.; Furukawa, M.; Tang, J.; Stadler, P.; Hoogland, S.; Voznyy, O.; Liu, H.; Sargent, E. H. *Adv. Mater.* **2012**, *24*, 6181.
(22) Giansante, C.; Carbone, L.; Giannini, C.; Altamura, D.; Ameer, Z.; Maruccio, G.; Loiudice, A.; Belviso, M. R.; Cozzoli, P. D.; Rizzo, A.; Gigli, G. *J. Phys. Chem. C* **2013**, *117*, 13305.
(23) Carrete, A.; Shavel, A.; Fontané, X.; Montserrat, J.; Fan, J.; Ibáñez, M.; Saucedo, E.; Pérez-Rodríguez, A.; Cabot, A. *J. Am. Chem. Soc.* **2013**, *135*, 15982.

(24) Selin Tosun, B.; Chernomordik, B. D.; Gunawan, A. A.; Williams, B.; Andre Mkhoyan, K.; Francis, L. F.; Aydil, E. S. *Chem. Commun.* **2013**, *49*, 3549.
(25) Stolle, C. J.; Panthani, M. G.; Harvey, T. B.; Akhavan, V. A.; Korgel, B. A. *ACS Appl. Mater. Interfaces* **2012**, *4*, 2757.
(26) Ning, Z.; Voznyy, O.; Pan, J.; Hoogland, S.; Adinolfi, V.; Xu, J.; Li, M.; Kirmani, A. R.; Sun, J.-P.; Minor, J.; Kemp, K. W.; Dong, H.; Rollny, L.; Labelle, A.; Carey, G.; Sutherland, B.; Hill, I.; Amassian, A.; Liu, H.; Tang, J.; Bakr, O. M.; Sargent, E. H. *Nat Mater* **2014**, *13*, 822.
(27) Dierick, R.; Van den Broeck, F.; De Nolf, K.; Zhao, Q.; Vantomme, A.; Martins, J. C.; Hens, Z. *Chem. Mater.* **2014**, *26*, 5950.
(28) Zhang, H.; Hu, B.; Sun, L.; Hovden, R.; Wise, F. W.; Muller, D. A.; Robinson, R. D. *Nano Lett.* **2011**, *11*, 5356.
(29) Tang, J.; Kemp, K. W.; Hoogland, S.; Jeong, K. S.; Liu, H.; Levina, L.; Furukawa, M.; Wang, X.; Debnath, R.; Cha, D.; Chou, K. W.; Fischer, A.; Amassian, A.; Asbury, J. B.; Sargent, E. H. *Nat Mater* **2011**, *10*, 765.
(30) Riha, S. C.; Parkinson, B. A.; Prieto, A. L. *J. Am. Chem. Soc.* **2009**, *131*, 12054.
(31) Qiu, L.; Zou, K.; Xu, G. *Appl. Surf. Sci.* **2013**, *266*, 230.
(32) Korala, L.; McGoffin, J. T.; Prieto, A. L. *ACS Appl. Mater. Interfaces* **2016**, *8*, 4911.
(33) Haight, R.; Barkhouse, A.; Gunawan, O.; Shin, B.; Copel, M.; Hopstaken, M.; Mitzi, D. B. *Appl. Phys. Lett.* **2011**, *98*, 253502.
(34) Erkan, M. E.; Chawla, V.; Scarpulla, M. A. *J. Appl. Phys.* **2016**, *119*, 194504.
(35) Neuschitzer, M.; Sanchez, Y.; López-Marino, S.; Xie, H.; Fairbrother, A.; Placidi, M.; Haass, S.; Izquierdo-Roca, V.; Perez-Rodriguez, A.; Saucedo, E. *Prog. Photovolt: Res. Appl.* **2015**, *23*, 1660.
(36) Ben Messaoud, K.; Buffière, M.; Brammertz, G.; ElAnzeery, H.; Oueslati, S.; Hamon, J.; Kniknie, B. J.; Meuris, M.; Amlouk, M.; Poortmans, J. *Prog. Photovolt: Res. Appl.* **2015**, *23*, 1608.
(37) Liu, X.; Feng, Y.; Cui, H.; Liu, F.; Hao, X.; Conibeer, G.; Mitzi, D. B.; Green, M. *Prog. Photovolt: Res. Appl.* **2016**, *24*, 879.
(38) Akhavan, V. A.; Goodfellow, B. W.; Panthani, M. G.; Reid, D. K.; Hellebusch, D. J.; Adachi, T.; Korgel, B. A. *Energy Environ. Sci.* **2010**, *3*, 1600.
(39) Shin, B.; Gunawan, O.; Zhu, Y.; Bojarczuk, N. A.; Chey, S. J.; Guha, S. *Prog. Photovolt: Res. Appl.* **2013**, *21*, 72.
(40) Pundsack, T. J.; Chernomordik, B. D.; Béland, A. E.; Aydil, E. S.; Blank, D. A. *J. Phys. Chem. Lett.,* **2013**, *4*, 2711.

CHAPTER 5: SYNTHETIC CONTROL OF QUINARY NANOCRYSTALS OF A PHOTOVOLTAIC MATERIAL: THE CLEAR ROLE OF CHALCOGEN RATIO ON LIGHT ABSORPTION AND CHARGE TRANSPORT FOR $CU_2ZN_{1+X}SN(S_{1-Y}SE_Y)_4$[5]

5. 1 Overview

Due to its constituent elements being earth abundant and non-toxic, solar cell devices based on a $Cu_2ZnSn(S_{1-x}Se_x)_4$ absorber layer are attractive for next generation photovoltaics.[1-3] The colloidal synthesis of CZTSSe NCs allows for film deposition based on solution based processes, without the need for high temperature annealing or selenization. This in turn provides a means to investigate the effects of changing the NC surface chemistry and composition on CZTSSe NC film electrical properties and PV device performance.[4,5] The cation stoichiometry of CZTSSe has been shown to dramatically effect photovoltaic performance of the absorber layer.[6-12] However, the role of the chalcogen ratio on film transport properties has been comparatively under investigated.[13,14] An introduction to the development of the colloidal synthesis of the full range of chalcogen ratios (x=0 to x=1) for $Cu_2ZnSn(S_{1-x}Se_x)_4$ NCs is described in Chapter 4. There were many considerations, including the synthetic approach, solvent and precursor identity, and final characteristics of the NCs that were important in the development of this synthesis. Ultimately,

[5] This chapter has been adapted by Max B. Braun from a manuscript to be submitted to the American Chemical Society's Journal: *Applied Materials & Interfaces*. Synthesis, deposition, characterization, device fabrication, testing, and manuscript preparation were performed by both Lasantha Korala, and Max B. Braun. Assistance with device fabrication and processing steps and was provided by Jason M. Kephart. We kindly acknowledge Kevan C. Cameron at CSU Next Generation PV Center (NGPV) for providing substrates for solar cell fabrication and Professor James Sites (Department of Physics, Colorado State University) for solar cell measurements. Amy L. Prieto offered valuable insight, direction, and aided in the manuscript preparation.

due to the ease of reproducibility, a facile heat-up method was chosen as the synthetic approach for the colloidal NC synthesis.[15] In order to minimize variation in cation stoichiometry, which could convolute the effects of varying the chalcogen ratio, specific attention was placed in the choice of metallic precursors and solvents. The use of glycerol as a secondary solvent (to OLA) was found to be necessary to maintain consistently Zn-rich, Cu and Sn-poor stoichiometry throughout NCs of all chalcogen ratios. This was especially important for the pure Se analog, thus, Cu and Sn precursors that were less likely to form Cu,Sn rich nuclei were chosen to allow for Zn incorporation. Importantly, the washing procedures for the NC product required that it could suspend in solution, which was necessary for solution based deposition methods to be possible.

5.2 Introduction

The compound $Cu_2ZnSn(S_{1-x}Se_x)_4$ (CZTSSe) is a potential photovoltaic (PV) material based on earth abundant, inexpensive, and non-toxic constituents. Research into the use of CZTSSe materials in thin film PVs is primarily inspired by its similarities to $CuIn_zGa_{1-z}(S_{1-x}Se_x)_2$ (CIGSSe), which is one of the leading thin-film PV materials.[1,2,16,17] Among the variety of thin-film deposition techniques, solution-phase deposition of CZTSSe thin films has gained more attention as a scalable and cost effective process, due to possibilities in roll-to-roll printing. Molecular ink-based and hydrazine-based solution processes have shown tremendous success in fabricating PV cells with over 10% efficiencies,[18, 3] and NC ink-based approaches have also achieved PV efficiency of 9% in which the final bulk absorber film is produced by selenization.[19]

Contrary to predictions of the optimal band gap (1.34 eV) for solar energy conversion by Shockley-Queisser considerations, to date, the best CZTSSe devices have been fabricated with the band gap centered around 1.15 eV through a hydrazine-based approach.[3,20,21] This observation has motivated several studies on the effect of the S/(S+Se) ratio on the electrical

properties of the absorber layer deposited by hydrazine-based process.[22-25] According to these investigations, a higher probability of secondary phase formation, which contributes to enhanced series resistance, at high S/(S+Se) ratios is found to be a major factor in low device performance. Additionlly, the selenization step can lead to variations in phase, composition, and grain size throughout the absorber film at different chalcogen ratios, which can be detrimental to performance and convolute the effects of selenium incorporation.[11,23-30] Moreover, in molecular ink- or hydrazine-based solution processes, the necessity of selenization to achieve desired CZTSSe crystalline phase rules out the flexible device design and further reduction in manufacturing cost.

The NC ink-based approach offers a path towards significant decrease in energy payback time, since desired CZTSSe crystal phase and composition can be synthesized at relatively low temperatures via solution-phase techniques. The as-synthesized NCs then can be assembled into thin films without annealing for device fabrication provided that suppression of surface defects and improvement in charge transport are achieved through a suitable ligand exchange process. In this regard, we recently reported the effect of a variety of ligand exchange strategies on performance of unannealed CZTS NC solar cells.[5] As a logical next step, we set out to evaluate the effect of S/(S+Se) ratio on performance of unannealed CZTSSe NC solar cells in order to find the best chalcogen composition for solar energy harvesting.

Key to this aim, however, is to maintain control over the stoichiometry of the metals in this compound. It is well documented that variation in the cation stoichiometry dramatically affects CZTSSe film optolectronic properties.[3,8,9,26,29,31,32] A more accurate formula, then, is $Cu_{2-x}Zn_{1+x}Sn(S_{1-y}Se_y)_4$. Previously reported synthetic techniques for making suspended particles are incapable of preserving optimal cation composition, the Cu/Zn ratio but specifically the Zn/Sn

ratio, at every chalcogen ratio.[1,10,15,33-37] Our first challenge in this study was to solve this problem by extending what is known about the nanoparticle synthesis for CZTSSe to significantly improve control over all five elements simultaneously. Herein, inspired by a method developed by Steinhagen et al. for CZTS NCs, we describe a one-pot heat-up method to successfully synthesize phase-pure $Cu_{2-x}Zn_{1+x}Sn(S_{1-y}Se_y)_4$ (y = 0, 0.3, 0.5, 0.7, and 1) NCs with desirable Cu/(Zn+Sn) and Zn/Sn ratios for PV applications.[38]

In addition to compositional, structural, and optical characteristics, the effect of chalcogen ratio on intrinsic charge carrier transport properties of ligand-exchanged CZTSSe NC films was assessed based on Hall-effect measurements for the first time. A significant increase in both carrier concentration and conductivity was found as a function of increased selenium incorporation. The improved carrier transport properties were correlated to enhanced photocurrent of PV devices based on the series of CZTSSe NC absorber films, leading to a maximum performance at the sulfur-to-selenium ratio of 1:1. The band gap of the NC absorber layer at highest efficiency (~1.30 eV) is significantly closer to the theoretically calculated optimum band gap value for PV energy conversion than selenized films. This study demonstrates that synthetic control over compositionally Zn rich nanoparticles can be used to decouple variables and understand fundamental structure-composition-properties.

5.3 Experimental Section

5.3.1 Nanocrystal Synthesis

Different compositions of $Cu_{2-x}Zn_{1+x}Sn(S_{1-y}Se_y)_4$ (CZTSSe) nanocrystals (NCs) were made using a simple one-pot heat-up method inspired by a synthetic route for CZTS developed by Steinhagen et al.[38] In a typical reaction 1.2 to 1.4 mmol of zinc acetate (0.220- 0.260 g, Sigma-Aldrich, ≥99.99%), 0.8 mmol of $SnCl_2 \cdot 2H_2O$ (0.180g, Sigma-Aldrich, ≥99.99%), 2 mmol of

copper(II) acetylacetonate (0.520 g, ≥99.99%), the corresponding molar amounts (totaling in 4 mmol) of elemental sulfur (Sigma-Aldrich, reagent grade, purified by sublimation) and selenium (Strem Chemical, 99.99%), 5 g of glycerol (Sigma-Aldrich, ≥99.5%), and 40 mL of OLA (Sigma-Aldrich, tech. grade, 70-80%) were added to a 100 mL three-neck round-bottom flask with a Teflon stir bar. The flask was equipped with a reflux condenser and a thermocouple with an adapter, and capped with rubber septa. All the connections were taped with Teflon to ensure sealing, and the flask was attached to a Schlenk line and purged with nitrogen, followed by heating to 115 °C under nitrogen flow. The reaction mixture was stirred for one hour and then temperature was raised to 260 °C under nitrogen overpressure and nanoparticles were grown for one hour. The heat was removed and the solution was allowed to cool to at least 80 °C while stirring. The reaction mixture was separated into six 15 mL centrifuge tubes. The reaction flask was rinsed with ethanol (Fisher Scientific, histological grade), and this was added to the centrifuge tubes until they were full. The tubes were then subjugated to centrifugation for 5 minutes at 3400 rpm. The precipitated NCs were dispersed in 6 mL of chloroform (Sigma-Aldrich, reagent grade, ≥99.8%) and centrifuged again for 15 minutes at 5800 rpm. The resulting supernatant was transferred to 6 new 15 mL centrifuge tubes. The tubes were then filled with ethanol and centrifuged for two minutes at 3400 rpm. The precipitated NCs were redispersed in 18 mL of chloroform and centrifuged for 15 minutes at 5800 rpm. The final suspended product was precipitated with ethanol and centrifuged for 2 minutes at 5800 rpm. The purified NCs were then dried under vacuum and stored in nitrogen glove box for further use.

5.3.2 Characterization of Structure, Morphology, and Composition.

X-ray diffraction (XRD) patterns were collected using a Scintag X-2 Powder X-Ray Diffractometer (λ= 1.54 Å). Energy dispersive spectroscopy (EDS) was performed with a

JEOL JSM 6500F FESEM equipped with an EDAX Genesis EDS detector. Low-resolution transmission electron microscopy (TEM) images were captured using a JEOL JEM-1400 transmission electron microscope. High-resolution images were acquired with a JEOL JEM-2100F transmission electron microscope (200 keV). UV-visible-near-infrared spectroscopy was carried out with a Cary 500 UV-vis-NIR spectrometer on a dilute NC solution in toluene. Raman spectroscopy was performed using a Horiba THz-Raman spectrometer (iHR550 imaging spectrometer) equipped with an Olympus ix73 microscope.

5.3.3 Film Deposition and Charge Transport Measurements

CZTSSe films for both photovoltaic (PV) and Hall-effect measurements were deposited by a dip-coating method. Approximately 15 mL of hexanes (Fisher Scientific, ACS grade) was added to ~100 mg of nanoparticles in a centrifuge tube and this was sonicated for 10 minutes. The NC solution was subsequently centrifuged for 5 minutes at 5800 rpm and the resulting supernatant was used for film deposition. Then 11 mM ethylenediamine (EDA, Sigma-Aldrich, ReagentPlus, ≥99%) and 1 mM ammonium sulfide (Sigma-Aldrich, 20% in H_2O), both in methanol (MeOH, Fisher Scientific, ACS grade), were used as the ligand exchange solutions. Using a home-made mechanical dip coater, the cleaned glass substrates were first dipped into the CZTSSe NC solution, then into EDA solution, then into ammonium sulfide solution, and finally rinsed by two dips in acetonitrile. This dipping procedure was repeated until a film thickness of ~150 nm was obtained (as determined by profilometry). The Hall-effect measurements were carried out in the four-point probe geometry using an Ecopia HMS-3000 Hall-effect Measurement System equipped with a 0.545T magnet.

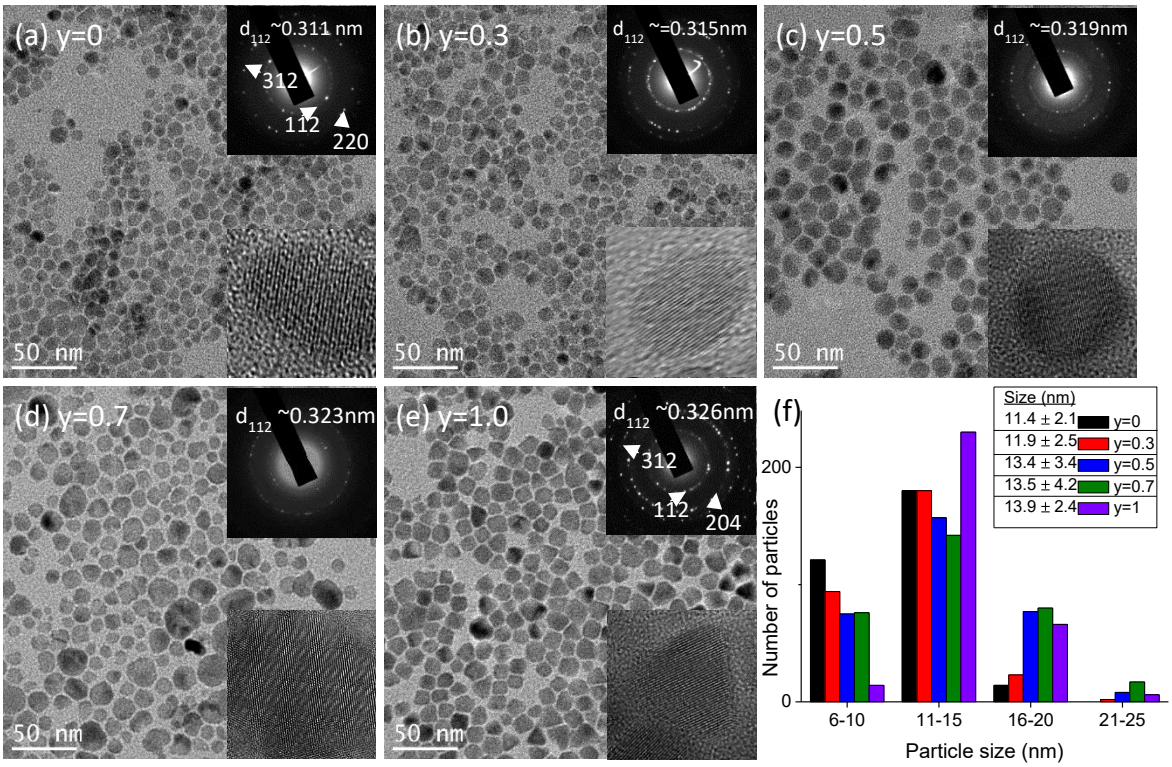

Figure 5.1. TEM images of $CZTS_{1-y}Se_y$ NCs with (a) y=0, (b) y=0.3, (c) y=0.5, (d) y=0.7, and (e) y=1. The lower insets show HRTEM images and upper insets display SAED patterns. (f) Binned size distribution of $CZTS_{1-y}Se_y$ NCs.

5.3.4 Photovoltaic (PV) Device Fabrication and Characterization

Complete PV devices were fabricated using previously reported methods.[5] Briefly, fluorine-doped tin oxide (FTO, TEC-12D) glass substrates covered with a layer of n-type CdS (~ 120nm) grown by close space sublimation were cut into 3 × 1 cm pieces. Subsequently, the NC layers (~250 nm) were deposited onto substrates as described in section 2.2. Gold electrodes (~250 nm) were then deposited on to the NC absorber layers by thermal evaporation at the base pressure of 1×10^{-6} Torr through a shadow mask. The resulting device area was 0.5 cm^2. The ($J-V$) curves were recorded using a Keithley 2401 source meter under a solar simulator with standard-test conditions (A.M. 1.5 Global spectrum with 100 mW cm^{-2} intensity) at 25 °C.

5.4 Results and Discussion

5.4.1 Synthesis and Characterization of CZTSSe Nanocrystals

The use of the heat-up synthetic technique for colloidal NCs offers many advantages with respect to the conventional hot-injection approach (e.g. scalability and batch to batch consistency).[15] Based on a synthetic procedure for CZTS NCs reported by Steinhagen et al., for the first time, we employ a one-pot heat-up synthetic method to produce various $Cu_{2-x}Zn_{1+x}Sn(S_{1-y}Se_y)_4$ (CZTSSe) NC compositions from metal salts for the entire range of chalcogen ratio (see Experimental Section for details).[38] Transmission electron microscopy (TEM) was employed to investigate the size, phase, and morphology of CZTSSe NCs with varying S/(S + Se) ratios. Figure 5.1a-e shows low-resolution TEM images of CZTSSe NCs (y=0, 0.3, 0.5, 0.7, and 1) along with corresponding high-resolution TEM (HRTEM) images and selected-area electron diffraction (SAED) patterns. The use of the heat-up synthesis allowed for NCs with comparable average size (Figure 5.1f) and morphology throughout all compositions. Drastic differences in size and morphology of NCs may convolute the effect of varying sulfur-to-selenium ratio by causing differences in the number of grain boundaries and surface states. Therefore, it was important that the size was controlled throughout all compositions. However, due to the differences between the selenium and sulfur ions there is an expected variation in the nucleation and growth rates of the particles, which lead to a small variation in average size as shown in Figure 5.1. The HR TEM images verified the crystallinity of the NCs, and corresponding indexed SAED patterns confirmed the structural transition from kesterite for pure CZTS (y=0, JCPDS no. 26-0575) to stannite

Table 5.1. Electrical properties of CZTSSe NC films

Sample	Cu:Zn:Sn:S:Se	Carrier concentration (cm^{-3})	Conductivity (Scm^{-1})
CZTS	1.8 : 1.3 : 0.9 : 4 : 0	$6.1 \pm 7.8 \times 10^{14}$	$6.9 \pm 2.6 \times 10^{-4}$
$CZTS_{0.7}Se_{0.3}$	1.8 : 1.3 : 0.9 : 2.9 : 1.2	$1.7 \pm 1.3 \times 10^{17}$	$5.2 \pm 2.0 \times 10^{-3}$
$CZTS_{0.5}Se_{0.5}$	1.8 : 1.2 : 0.9 : 2.1 : 1.9	$2.3 \pm 2.5 \times 10^{18}$	$2.2 \pm 0.8 \times 10^{-2}$
$CZTS_{0.3}Se_{0.7}$	1.8 : 1.3 : 0.8 : 1.3 : 2.7	$3.3 \pm 3.0 \times 10^{19}$	$9.3 \pm 6.6 \times 10^{-2}$
CZTSe	1.8 : 1.2 : 0.9 : 0 : 4	$6.5 \pm 5.1 \times 10^{18}$	$2.9 \pm 0.3 \times 10^{-2}$

for pure CZTSe (y=1, JCPDS no. 52-0868), and gradual incorporation of larger Se atoms as indicated by increase in d-spacing for the 112 plane as x increased.

X-ray diffraction (XRD) on NC powder samples further revealed the crystalline structure and phase as shown in Figure 5.2a. In the XRD patterns, the observed peak shifts to lower 2θ as y increases are characteristic of selenium incorporation due to expanded interplanar spacing.[39] Similarly, the Raman spectra (Figure S5.1) illustrate the gradual loss in CZTS characteristic stretching accompanied by the growth of CZTSe based intensities as y increases.[40] Furthermore, there is an expected shift in the CZTS A_1 mode (~334 cm^{-1}) to lower wavenumbers as Se is incorporated. Eventually, the CZTSe A_1 mode (190 cm^{-1}) and an additional CZTSe stretching mode (~236 cm^{-1}) dominate for the Se heavy phases. Note that there are *no* additional peaks from secondary phases, specifically those that could not be ruled out by XRD, found in any of the spectra.[37,40] Additionally, as displayed in the UV-visible-near-infrared spectra (Figure S5.2), there is a shift in absorption onset to higher wavelengths, indicative of selenium incorporation. The Tauc-plot created from the absorption data exhibits the incremental bandgap shift from ~1.50 eV (CZTS) down to ~1.09 eV (CZTSe) as y increases and the band gap values for the various compositions are comparable to the predicted values for the CZTSSe NCs (Figure 5.2b).[41]

The composition of each NC sample was characterized by energy dispersive X-ray analysis (EDS) and the results are displayed in Table 5.1. The Cu/(Zn+Sn) and Zn/Sn ratios

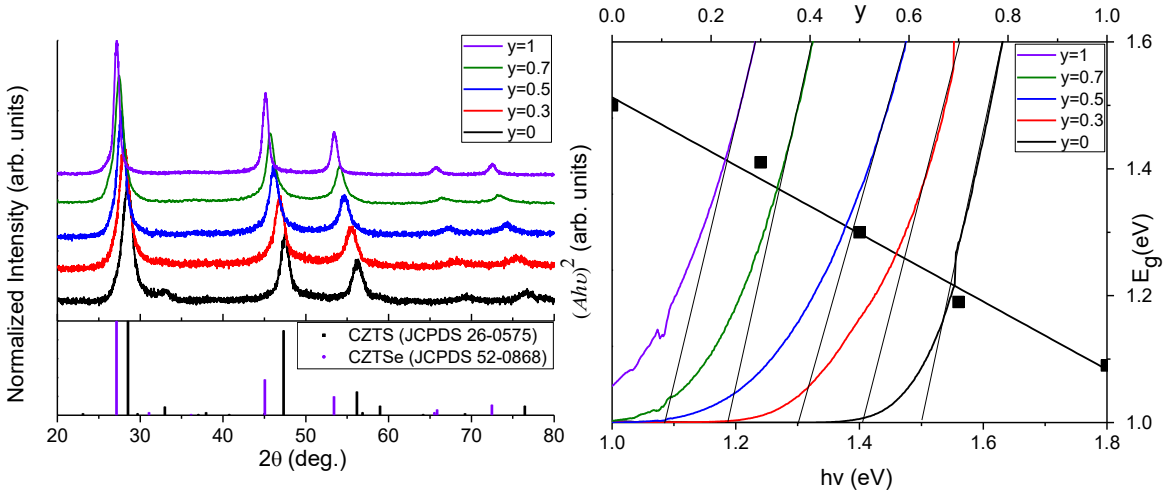

Figure 5.2. (a) PXRD patterns of CZTSSe NCs displaying the incremental shift to lower 2θ as selenium amount is increased. The inset shows reference lines for kesterite CZTS and CZTSe. (b) Plots of $(Ah\upsilon)^2$ vs. $h\upsilon$ and E_g vs. x (black), displaying band gap shift as a function of selenium incorporation.

are around 0.8 and 1.3 respectively, and these values are within the range of cation ratios that have previously yielded the best performing CZTSSe PV devices.[3] It was especially important for this study to maintain the ratios of Cu:Zn:Sn consistent throughout all compositions, as variations in cation ratios affect the film transport properties and convolute the effects of selenium incorporation.[3,8,9,26,29,31,32] Due to these effects from compositional differences, achieving the desirable elemental ratios in CZTSSe based NCs has afforded a large number of reports looking at variations in synthetic techniques andprecursors to yield advantageous compositions.[6,9,10,31,42] In that regard, there are few reports that have looked at the CZTSSe NC synthesis of the full range of sulfur to selenium compositions. In 2011, our group reported the first solution synthesis of the full range of CZTSSe compositions; however, toxic and harsh ingredients (i.e. trioctylphosphine oxide, sodium borohydride) were necessary to synthesize the NCs.[39] Since then, Ou *et al.* and Ji *et al.* have reported alternative syntheses, however these procedures failed to maintain the

optimal cation ratios (discussed above) throughout all compositions.[36,37] This is specifically true for the pure selenium analog, CZTSe, that is historically zinc deficient.[1,10,15,33-37]

In consideration of these difficulties, we were inspired to develop a novel one-pot synthesis over the full range of S/(S+Se) ratios without the use of toxic or harsh ingredients, while maintaining the desirable Cu/(Zn+Sn) and Zn/Sn ratios (0.8 and 1.3, respectively). Many synthetic variations were attempted (e.g. varying precursor reactivity, temperature, and concentration; see the supporting information for further discussion); however, the desired cation ratios were only yielded at every composition when glycerol (~5 g) was used as an additional solvent to oleylamine. The use of glycerol as the main solvent in CZTSSe synthesis was demonstrated by Ji *et al.*, and its hydroxy groups are proposed to help complex with metal precursors and possibly act as a surface capping agent.[37] In the one-pot synthetic process described herein, although it was possible to make the majority of the compositions with oleylamine as the sole solvent, using only oleylamine lead to small (~4-8 nm) nanoparticles of CZTSe with less than ideal zinc concentration (<11 at%). This result suggests that the glycerol forms a complex with a metal precursor that leads to the ideal conditions for the creation of the quaternary/quinary system.

The composition of each NC sample was characterized by energy dispersive X-ray analysis (EDS) and the results are displayed in Table 5.1. The Cu/(Zn+Sn) and Zn/Sn ratios are around 0.8 and 1.35, respectively, and these values are within the range of cation ratios that have previously yielded best-performing CZTSSe PV devices.[3] It was especially important for this study to maintain the ratios of Cu:Zn:Sn consistent throughout all compositions, as variations in cation ratios affect the film transport properties and convolute the effects of selenium incorporation.[3,8,9,26,29,31,32] Due to these effects from compositional differences, achieving the

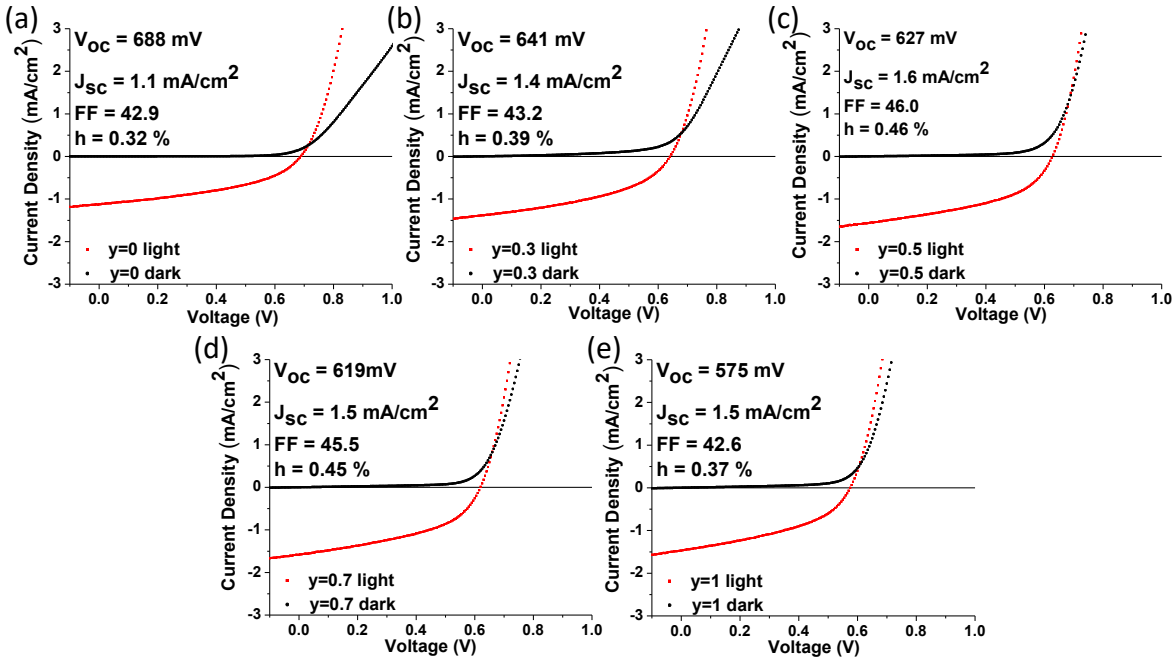

Figure 5.3. J-V curves and device parameters of champion $CZTS_{1-y}Se_y$ PV devices with (a) y=0, (b) y=0.3, (c) y=0.5, (d) y=0.7, and (e) y=1.

desirable elemental ratios in CZTSSe based NCs has afforded a large number of reports looking at variations in synthetic techniques and precursors to yield advantageous compositions.[6,9,10,31,42] In that regard, there are few reports that have looked at the CZTSSe NC synthesis of the full range of sulfur to selenium compositions. In 2011, our group reported the first solution synthesis of the full range of CZTSSe compositions; however, toxic and harsh ingredients (i.e., Trioctylphosphine oxide, sodium borohydride) were necessary to synthesize the NCs.[39] Since then, Ou *et al.* and Ji *et al.* have reported alternative syntheses, however these procedures failed to maintain the optimal cation ratios (discussed above) throughout all compositions.[36,37] This is specifically true for pure selenium analog, CZTSe, that is historically zinc deficient.[1,10,15,33-37] In consideration of these difficulties, we were inspired to develop a novel one-pot synthesis over the full range of S/(S+Se) ratios without the use of toxic or harsh ingredients, while maintaining the desirable Cu/(Zn+Sn) and Zn/Sn ratios. Many synthetic variations were attempted (e.g., varying precursor reactivity,

temperature, and concentration; see supporting information for further discussion); however, the desired cation ratios were only yielded at every composition when glycerol (~5 g) was used as an additional solvent to oleylamine. The use of glycerol as the main solvent in CZTSSe synthesis was demonstrated by Ji *et al.*, and its hydroxy groups are proposed to help complex with metal precursors and possibly act as a surface capping agent.[37] In the presented one-pot synthetic process, although it was possible to make the majority of the compositions with oleylamine as the sole solvent, using only oleylamine lead to small (~4-8 nm)nanoparticles of CZTSe with less than ideal zinc concentration (<11 at%). This result suggests that the glycerol forms a complex with a metal precursor that leads to the ideal conditions for the creation of the quaternary/quinary system.

5.4.2 Film Deposition and Hall-effect Measurement

In a previous study, our group demonstrated that the conductivity of CZTSSe NC powders with varying S/(S+Se) ratio increased as a function of Se concentration.[39] However, the measurements were performed on unannealed bulk NC powders and not thin-films. For a more accurate look at the NC-based thin film transport properties, we have recently employed rational ligand exchange strategies to reduce defects on the surface of the complicated, quaternary CZTS NCs in film deposition process paper following the current advances in ligand-exchange chemistry for binary metal chalcogenide NCs.[5, 43, 44] Accordingly, in this study we deposited NC films by layer-by-layer dip coating method, and the native ligands on the NC surface were exchanged with ethylenediamine (EDA) and sulfide at each dipping cycle (see experimental section for details). The intrinsic charge transport properties as a function of S/(S+Se) ratio were determined, for the first time, via Hall-effect measurement on the NC thin films (~150 nm) of each composition deposited

onto glass substrates (Table 5.1). The Hall-effect measurements confirmed the increase in conductivity of NC films with increasing selenium concentration as previously observed.[39]

When sulfur is completely replaced by selenium, the conductivity and carrier concentration of the NC films were increased by up to 2 and 4 orders of magnitude, respectively (Table 5.1). The observed carrier concentrations in NC films, on the order of 10^{14} to 10^{21} cm^{-3}, agree well with previously reported results for CZTSSe films deposited by other methods.[1,25,45] Additionally, the observed trend in conductivity is consistent with a recent report by Tai et al. that used Hall-effect measurements to look at the electrical properties of CZTSSe films deposited by the hydrazine-based process.[25] The authors found that both the conductivity and carrier concentrations increased by an order of magnitude when changing the S/(S+Se) ratio from 0.9 to 0. However, in our NC films, a dramatic change in carrier density was not observed after 50% of Se incorporation.[24,25]

5.4.3 Photovoltaic (PV) Performances of CZTSSe Films

In order to correlate the results from the Hall-effect measurements with PV device performance, the absorber layers of the PV devices were deposited following the same procedure that was used for the film transport property measurements, with the exception being the substrate. The CZTSSe films (~250 nm) were deposited onto CdS-coated FTO glass substrates to form heterojunction NC PV devices in superstrate configuration (see Experimental Section for details). The performances of the champion PV devices, made from each of the five S/(S + Se) compositions, revealed that increased selenium incorporation was beneficial until reaching an apex at x=0.5 (Figure 5.3). The maximum performance (PCE= 0.46%) at this composition is due to competition between the enhanced film conductivity with selenium incorporation (resulting in higher J_{sc}) countered by band

gap reduction. The increase of sulfur-to-selenium ratio beyond this optimal composition caused lower efficiency due to the degradation of V_{oc} and the fill factor (FF) because of a decrease in the band gap. It is important to note that photogenerated carriers in the absorber layer were not collected in this device configuration as shown in EQE spectrum of device c (Figure S5.3). However, variation in PV characteristics reflected the changes in the absorber layer since all the other layers were not altered in the device fabrication. This was further confirmed in a separate study, where we have investigated the impact of device configuration and deposition method of CdS buffer layer on collection efficiency of photocarriers in the absorber layer.[5]

Table S5.1 contains statistics of PV parameters of CZTSSe devices from this study, as well as PV characteristics of devices fabricated by Tai *et al.* and the record CZTSSe device .[6d, 3] As seen in Table S5.1 and other previous reports, the record performances for CZTSSe PV devices were obtained at heavily selenium rich compositions (y = 0.7-0.9) with band gap centered around 1.15 eV.[3,24,25,45] For our devices, however, the optimum composition range (y = 0.5-0.7) shifted towards larger band gap values (E_g= 1.19-1.30 eV), which are closer to the optimal band gap (1.34 eV) predicted for maximum theoretical solar conversion efficiency according to the Shockley-Queisser limit.[20,21] This behavior is primarily related to differences in absorber layer production. In contrast to NC films deposited at room temperature, the absorber layers prepared by selenization have a high probability of secondary phase formation in the bulk of the film and at the back contact interface. These secondary phases have adverse effects on device performance. For example, formation of wider band gap martials such as ZnS and ZnSe can hinder carrier transport although ZnS is less favorable with respect to ZnSe due to a relatively high band

gap. This has been proposed as a reason for better performance in Se rich compounds.[23,24] Furthermore, Tai *et al.* proposed that a primary reason for improved performance at highly Se rich compositions is due to low propensity of secondary phase formation (e.g. $(SnS(Se)_2$, ZnS(Se), $MoS(Se)_2)$) at the back contact interface that contributes to high series resistance.[25] Due to the absence of the selenization step in our CZTSSe NC-based PV device fabrication process, secondary phase formation at the interface is minimal and this leads to a more inherent material-based behavior. However, as reported previously, there is a possibility that intra- and inter-particle inhomogenities presence in the quaternary/quinary NCs could convolute the effect of S/(S + Se) ratio.[46,47] Due to the very close similarities in synthetic procedures for all compositions presented here, this convolution is likely minimal.

5.5 Conclusions

Using a one-pot synthetic method, we fabricated a series of $Cu_{2-x}Zn_{1+x}Sn(S_{1-y}Se_y)_4$ (y=0, 0.3, 0.5, 0.7, 1) NC compounds with exceptional control over the concentration of all elemental constituents. Importantly, all of the compositions were synthesized with a zinc rich, copper poor configuration with Cu/(Zn+Sn) and Zn/Sn ratios around 0.8 and 1.35, respectively. Transport measurements of ligand-passivated NC films revealed that an increase in selenium incorporation leads to an inherent increase in conductivity and carrier concentration by up to two and four orders of magnitude, respectively. Using low-temperature approaches to fabricate our photovoltaic devices provided a route to understand the relationship between chalcogen ratio, transport properties, and device performance. The compromise between the enhancement in electrical properties and the reduction of band gap with Se concentration resulted in maximum performance at composition y=0.5. Notably, the band gap (E_g=1.30 eV) at this composition is much closer to

the predicted optimal band gap (E_g=1.34 eV) compared to the bulk devices (E_g=1.15 eV) based on selenized CZTSSe absorber materials.

REFERENCES

(1) Zhou, H.; Hsu, W.-C.; Duan, H.-S.; Bob, B.; Yang, W.; Song, T.-B.; Hsu, C.-J.; Yang, Y. *Energy Environ. Sci.* **2013**, *6*, 2822.
(2) Suryawanshi, M. P.; Agawane, G. L.; Bhosale, S. M.; Shin, S. W.; Patil, P. S.; Kim, J. H.; Moholkar, A. V. *Materials Technology* **2013**, *28*, 98.
(3) Wang, W.; Winkler, M. T.; Gunawan, O.; Gokmen, T.; Todorov, T. K.; Zhu, Y.; Mitzi, D. B. *Adv. Energy Mater.* **2014**, *4*, 1301465.
(4) Talapin, D. V.; Lee, J.-S.; Kovalenko, M. V.; Shevchenko, E. V. *Chemical reviews* **2010**, *110*, 389.
(5) Korala, L.; Braun, M. B.; Kephart, J. M.; Tregillus, Z.; Prieto, A. L. *Chemistry of Materials* **2017**, *29*, 6621.
(6) Collord, A. D.; Hillhouse, H. W. *Chemistry of Materials* **2015**, *27*, 1855.
(7) Katagiri, H.; Jimbo, K.; Tahara, M.; Araki, H.; Oishi, K. *MRS Proceedings* **2009**, *1165*.
(8) Li, J.; Wang, H.; Wu, L.; Chen, C.; Zhou, Z.; Liu, F.; Sun, Y.; Han, J.; Zhang, Y. *ACS Applied Materials & Interfaces* **2016**, *8*, 10283.
(9) Nishi, H.; Kuwabata, S.; Torimoto, T. *The Journal of Physical Chemistry C* **2013**, *117*, 21055.
(10) Rath, T.; Haas, W.; Pein, A.; Saf, R.; Maier, E.; Kunert, B.; Hofer, F.; Resel, R.; Trimmel, G. *Solar Energy Materials and Solar Cells* **2012**, *101*, 87.
(11) Roelofs, K. E.; Guo, Q.; Subramoney, S.; Caspar, J. V. *Journal of Materials Chemistry A* **2014**, *2*, 13464.
(12) Riha, S. C.; Parkinson, B. A.; Prieto, A. L. *J. Am. Chem. Soc.* **2009**, *131*, 12054.
(13) Duan, H.-S.; Yang, W.; Bob, B.; Hsu, C.-J.; Lei, B.; Yang, Y. *Adv. Funct. Mater.* **2013**, *23*, 1466.
(14) Tai, K. F.; Gunawan, O.; Kuwahara, M.; Chen, S.; Mhaisalkar, S. G.; Huan, C. H. A.; Mitzi, D. B. *Adv. Energy Mater.* **2015**, *6*.
(15) van Embden, J.; Chesman, A. S. R.; Jasieniak, J. J. *Chemistry of Materials* **2015**, *27*, 2246.
(16) Zhou, C.; Fang, Z. Z.; Bowman, R. C. *The Journal of Physical Chemistry C* **2015**, *119*, 22261.
(17) Polizzotti, A.; Repins, I. L.; Noufi, R.; Wei, S.-H.; Mitzi, D. B. *Energy Environ. Sci.* **2013**, *6*, 3171.
(18) Larramona, G.; Levcenko, S.; Bourdais, S.; Jacob, A.; Chone, C.; Delatouche, B.; Moisan, C.; Just, J.; Unold, T.; Dennler, G. *Advanced Energy Materials* **2015**, *5*, 1501404.
(19) Miskin, C. K.; Yang, W.-C.; Hages, C. J.; Carter, N. J.; Joglekar, C. S.; Stach, E. A.; Agrawal, R. *Prog. Photovolt: Res. Appl.* **2015**, *23*, 654.
(20) Rau, U.; Werner, J. H. *Applied Physics Letters* **2004**, *84*, 3735.
(21) Shockley, W.; Queisser, H. J. *Journal of Applied Physics* **1961**, *32*, 510.
(22) Gunawan, O.; Gokmen, T.; Warren, C. W.; Cohen, J. D.; Todorov, T. K.; Barkhouse, D. A. R.; Bag, S.; Tang, J.; Shin, B.; Mitzi, D. B. *Applied Physics Letters* **2012**, *100*, 253905.
(23) Redinger, A.; Mousel, M.; Wolter, M. H.; Valle, N.; Siebentritt, S. *Thin Solid Films* **2013**, *535*, 291.

(24) Duan, H.-S.; Yang, W.; Bob, B.; Hsu, C.-J.; Lei, B.; Yang, Y. *Advanced Functional Materials* **2013**, *23*, 1466.
(25) Tai, K. F.; Gunawan, O.; Kuwahara, M.; Chen, S.; Mhaisalkar, S. G.; Huan, C. H. A.; Mitzi, D. B. *Advanced Energy Materials* **2016**, *6*, 1501609.
(26) Kanevce, A.; Repins, I.; Wei, S.-H. *Solar Energy Materials and Solar Cells* **2015**, *133*, 119.
(27) Yin, X.; Tang, C.; Sun, L.; Shen, Z.; Gong, H. *Chemistry of Materials* **2014**, *26*, 2005.
(28) Hwang, Y.; Park, B.-I.; Lee, B.-S.; Kim, J. Y.; Jeong, J.-H.; Kim, H.; Ko, M. J.; Kim, B.; Son, H. J.; Lee, S. Y.; Lee, J.-S.; Park, J.-K.; Cho, S.-H.; Lee, D.-K. *The Journal of Physical Chemistry C* **2014**, *118*, 27657.
(29) Neuschitzer, M.; Sanchez, Y.; Olar, T.; Thersleff, T.; Lopez-Marino, S.; Oliva, F.; Espindola-Rodriguez, M.; Xie, H.; Placidi, M.; Izquierdo-Roca, V.; Lauermann, I.; Leifer, K.; Pérez-Rodriguez, A.; Saucedo, E. *Chemistry of Materials* **2015**, *27*, 5279.
(30) Hsu, W.-C.; Zhou, H.; Luo, S.; Song, T.-B.; Hsieh, Y.-T.; Duan, H.-S.; Ye, S.; Yang, W.; Hsu, C.-J.; Jiang, C.; Bob, B.; Yang, Y. *ACS Nano* **2014**, *8*, 9164.
(31) Kuo, D.-H.; Tsega, M. *Materials Research Bulletin* **2014**, *49*, 608.
(32) Yu, K.; Carter, E. A. *Chemistry of Materials* **2016**, *28*, 4415.
(33) Liu, Y.; Yao, D.; Shen, L.; Zhang, H.; Zhang, X.; Yang, B. *Journal of the American Chemical Society* **2012**, *134*, 7207.
(34) van Embden, J.; Chesman, A. S. R.; Della Gaspera, E.; Duffy, N. W.; Watkins, S. E.; Jasieniak, J. J. *J. Am. Chem. Soc.* **2014**, *136*, 5237.
(35) Lee, P.-Y.; Chang, S.-P.; Hsu, E.-H.; Chang, S.-J. *Solar Energy Materials and Solar Cells* **2014**, *128*, 156.
(36) Ou, K.-L.; Fan, J.-C.; Chen, J.-K.; Huang, C.-C.; Chen, L.-Y.; Ho, J.-H.; Chang, J.-Y. *J Mater Chem* **2012**, *22*, 14667.
(37) Ji, S.; Shi, T.; Qiu, X.; Zhang, J.; Xu, G.; Chen, C.; Jiang, Z.; Ye, C. *Sci. Rep.* **2013**, *3*.
(38) Steinhagen, C.; Panthani, M. G.; Akhavan, V.; Goodfellow, B.; Koo, B.; Korgel, B. A. *J. Am. Chem. Soc.* **2009**, *131*, 12554.
(39) Riha, S. C.; Parkinson, B. A.; Prieto, A. L. *J. Am. Chem. Soc.* **2011**, *133*, 15272.
(40) Fernandes, P. A.; Salomé, P. M. P.; da Cunha, A. F. *Journal of Alloys and Compounds* **2011**, *509*, 7600.
(41) Chen, S.; Walsh, A.; Yang, J.-H.; Gong, X. G.; Sun, L.; Yang, P.-X.; Chu, J.-H.; Wei, S.-H. *Physical Review B* **2011**, *83*, 125201.
(42) Jiang, C.; Liu, W.; Talapin, D. V. *Chemistry of Materials* **2014**, *26*, 4038.
(43) Chuang, C.-H. M.; Brown, P. R.; Bulović, V.; Bawendi, M. G. *Nat Mater* **2014**, *13*, 796.
(44) Ip, A. H.; Thon, S. M.; Hoogland, S.; Voznyy, O.; Zhitomirsky, D.; Debnath, R.; Levina, L.; Rollny, L. R.; Carey, G. H.; Fischer, A.; Kemp, K. W.; Kramer, I. J.; Ning, Z.; Labelle, A. J.; Chou, K. W.; Amassian, A.; Sargent, E. H. *Nat Nano* **2012**, *7*, 577.
(45) Gershon, T.; Gokmen, T.; Gunawan, O.; Haight, R.; Guha, S.; Shin, B. *Mrs Communications* **2014**, *4*, 159.
(46) Haas, W.; Rath, T.; Pein, A.; Rattenberger, J.; Trimmel, G.; Hofer, F. *Chemical communications* **2011**, *47*, 2050.
(47) Yang, W.-C.; Miskin, C. K.; Carter, N. J.; Agrawal, R.; Stach, E. A. *Chemistry of Materials* **2014**, *26*, 6955.

CHAPTER 6: SUMMARY AND OUTLOOK FOR CZTSSE NCS FOR PHOTOVOLTAIC APPLICATIONS[6]

6.1 Synthesis, film deposition, and full device fabrication for fundamental studies on CZTSSe NC surface and composition effects on PV performance

6.1.1 Synthesis of CZTSSe NCs with exceptional control over composition

Due to its constituent elements being earth abundant and non-toxic, solar cell devices based on a $Cu_2ZnSn(S_{1-x}Se_x)_4$ absorber layer are attractive for next-generation photovoltaics.[1-3] The colloidal synthesis of CZTSSe NCs allows for film deposition based on solution based processes, without the need for high temperature annealing or selenization. This in turn provides a means to investigate the effects of changing the NC surface chemistry and composition on CZTSSe NC film electrical properties and PV device performance.[4,5] The cation stoichiometry of CZTSSe has been shown to dramatically effect photovoltaic performance of the absorber layer.[6-12] However, the role of the chalcogen ratio on film transport properties has been comparatively under investigated.[13,14]

An introduction to the development of the colloidal synthesis of the full range of chalcogen ratios (x=0 to x=1) for $Cu_2ZnSn(S_{1-x}Se_x)_4$ NCs is described in Chapter 4. There were many considerations, including the synthetic approach, solvent and precursor identity, and final characteristics of the NCs that were important in the development of this synthesis. Ultimately, due to the ease of reproducibility, a facile heat-up method was chosen as the synthetic approach

[6] This chapter was written by Max B. Braun with assistance in editing and direction provided by Amy L. Prieto. It serves as a conclusions and future directions chapter for Part II of this dissertation.

for the colloidal NC synthesis.[15] In order to minimize variation in cation stoichiometry, which could convolute the effects of varying the chalcogen ratio, specific attention was placed in the choice of metallic precursors and solvents. The use of glycerol as a secondary solvent (to OLA as the primary solvent) was found to be necessary to maintain consistently Zn-rich, but Cu and Sn-poor stoichiometry throughout NCs of all chalcogen ratios. This was especially important for the pure Se analog; thus, Cu and Sn precursors that were less likely to form Cu, Sn rich nuclei were chosen to allow for Zn incorporation. Importantly, the washing procedures for the NC product required that proved to be suspendable in solution, a feature necessary for solution-based deposition methods to be possible.

6.1.2 CZTSSe NC surface treatment, device fabrication and performance analysis

Chapter 4 describes investigations into the deposition methods that would be employed for CZTSSe NC film creation. These investigations looked at the use of solution based ligand exchange to remove the bulky ligands on the surface with shorter organic and inorganic ligands. Due to the complicated surface of the quaternary/quinary CZTSSe system, ligand-exchange strategies were employed to passivate the multiple surface states that can exist that are detrimental to film transport properties, and ultimately photovoltaic performance. Hall-effect measurements showed that the transport properties (i.e., carrier concentration and conductivity) of ligand exchanged CZTS NC films could be improved by exchanging and treating the NC surface with multiple types (X-, L-, and Z-) of ligands.[5] However, even with the enhancement of the film transport properties due to surface passivation, PV devices based on the ligand-exchanged CZTS NCs still show low conversion efficiency (<0.5% PCE). Although the optimized ligand exchange strategies (i.e., the use of X-, L-, and Z- type ligands) yielded CZTS NC PV devices with ~180 mV increase in V_{oc}, a large voltage deficit ($V_{oc,def}$ ~900 mV) is still seen for the CZTS NC devices.

This deficit likely due to the internal defects inherent to the complicated quaternary NCs.[16,17] Nonetheless, the ligand exchange strategies allowed for the deposition of NC films with considerably high conductivity and carrier concentrations.[5] This allowed for the investigation into the role of chalcogen ratio on NC film transport properties for films made with $CZTS_{1-x}Se_x$ (x=0 to x=1) NCs.

Using a novel colloidal synthetic technique to synthesize the full range of $Cu_2ZnSn(S_{1-x}Se_x)_4$ (x=0, 0.3, 0.5, 0.7, 1) NCs, NC films were deposited using the ligand exchange strategy developed in Chapter 4. In Chapter 5, the synthetic protocol for the CZTSSe NCs is presented, as well as the full morphological and structural characterization of these NCs. The XRD patterns, EDS, UV-Vis spectra, and Raman spectra all confirm the correct S to Se ratios for all compositions (x=0, 0.3, 0.5, 0,7 and 1). Furthermore, NC size (12-14 nm) and cationic stoichiometry (Zn-rich, Sn,Cu-poor) were successfully maintained throughout all S/Se ratios. Hall effect studies on $CZTS_{1-x}Se_x$ (x=0 to 1) NC films were performed for the first time, and indicated Se inclusion was followed by an increase in conductivity and carrier concentration. PV measurements reflected this trend, with devices based on Se rich CZTSSe exhibiting higher current density compared to the S rich compositions. However, as a result of a decrease in band gap, the open circuit voltage decreased with increasing Se inclusion. This lead to the best PV performance to be centered around 1.3 eV (x=0.5), which is than previous champion devices (~1.15 eV) to the optimal value predicted based on the Shockley-Queisser limit (1.34 eV).[18] The reason for this shift is likely due to the lack of complications introduced during the selenization process, thus providing a more inherent look at material properties based on chalcogen ratio.[19-21] However, despite exceptional transport properties for the CZTSSe NC films, PV performance was still quite low (<0.5% PCE). As mentioned in Chapter 4, this is due to internal defects inherent to the CZTSSe material, the number

of grain boundaries for the unannealed films, an unoptimized ZnO:Al layer, and back contact issues.[5]

6.2 Future directions: Device optimization and reduction of trap states

6.2.1 Back and front contact optimization

In Chapter 4, the issue of the device configuration is discussed. Originally, the superstrate configuration was used during device fabrication. This involves the deposition of the n-type semiconductor layer (CdS) onto transparent conducting oxide, followed by the p-type semiconductor (CZTSSe), and finally the back contact (Au). However, upon measurement of the external quantum efficiency, it was evident that the majority of carrier collection was coming from the CdS window layer. This indicated that excitons generated in the CZTSSe NC layer were recombining before they could be extracted. As mentioned in Chapter 4, this is likely due to a barrier at the p-n junction (due to improper band alignment), or at the back contact that prevents the extraction of the charge carriers from the absorber layer. By adopting the substrate device architecture (deposition starts from the back contact), charge carriers were collected from both the CdS and CZTS layer NC layer. This a result of the diffusion of Cd^{2+} into the CZTS layer, and consequent epitaxial growth of the CdS layer onto the CZTS film. This allows for a higher quality p-n junction, due to buried homojunctions lowering the potential for recombination.[22,23] Similarly, in devices that use selenization or annealing procedures during the deposition of the CZTSSe layer onto the back contact (Mo), S and Se diffuse into the Mo layer. This allows for more facile extraction of charge carriers at this junction.[3] For our devices, however, this process is less likely. Consequently, treatment of the Mo with S or Se prior to deposition may increase the charge carrier extraction at this junction. Alternatively, other metals, with work functions that more properly align with CZTSSe NCs conduction band edge could be explored.[24]

Correspondingly, the deposition of the transparent conducting oxide (aluminum doped zinc oxide) was unoptimized and the resulting TCO layer did not have high conductivity. This lead to a large series resistance in the devices which affected the current generated. Through the optimization of this layer (i.e., increasing its conductivity), the device performance could be increased.

6.2.2 Reduction of trap states in NC based devices

CZTSSe NC films have a large chance for exciton recombination due to the large number of trap states from internal defects, and low mobility from an abundance of grain boundaries. Consequently, even after performing the optimizations described above, it is likely that the overall device performance will remain low. Recently, Hages *et al.* have shown that alloying CZTSe with Ag decreases the number of internal defects that could act as trap states. Thus, they report an increase in V_{oc} with just 5% Ag^{+} inclusion into CZTSe.[25] Similarly, the presence of alkali metals (i.e., Li, Rb, Ca, K and Na) prior to the selenization of CZTS precursors has been shown to increase the V_{oc} of the final CZTSSe based device. The alkali-metal mechanism of enhancement has mostly been attributed to improved grain growth, although reduction in secondary phase formation, and surface passivation have been reported.[26,27] Correspondingly, the exploration of CZTSSe syntheses with a small amount of additional cations (be it another transition metal, or an alkali metal) could reduce trap states and improve PV performance of the NC based films.

6.3 Summary

In summary, through the development of novel NC synthetic and deposition techniques, we were able to uncover some fundamental structure-property relationships in the CZTSSe system that were previously unattainable. The use of NC CZTSSe has some inherent drawbacks, -notably,

trap states, cation distribution, and low carrier lifetime- but there is still room for improvement and development with CZTSSe, especially in the broad arena of earth abundant metal chalcogenides. The work presented in the Part II of this dissertation provides a foundation for fundamental research on NC systems similar to CZTSSe. By developing a better understanding of existing, and especially complicated systems like the quinary CZTSSe, the selection and design of better performing materials is closer to realization.

REFERENCES

(1) Zhou, H.; Hsu, W.-C.; Duan, H.-S.; Bob, B.; Yang, W.; Song, T.-B.; Hsu, C.-J.; Yang, Y. *Energy Environ. Sci.* **2013**, *6*, 2822.
(2) Suryawanshi, M. P.; Agawane, G. L.; Bhosale, S. M.; Shin, S. W.; Patil, P. S.; Kim, J. H.; Moholkar, A. V. *Materials Technology* **2013**, *28*, 98.
(3) Wang, W.; Winkler, M. T.; Gunawan, O.; Gokmen, T.; Todorov, T. K.; Zhu, Y.; Mitzi, D. B. *Adv. Energy Mater.* **2014**, *4*, 1301465.
(4) Talapin, D. V.; Lee, J.-S.; Kovalenko, M. V.; Shevchenko, E. V. *Chemical reviews* **2010**, *110*, 389.
(5) Korala, L.; Braun, M. B.; Kephart, J. M.; Tregillus, Z.; Prieto, A. L. *Chemistry of Materials* **2017**, *29*, 6621.
(6) Collord, A. D.; Hillhouse, H. W. *Chemistry of Materials* **2015**, *27*, 1855.
(7) Katagiri, H.; Jimbo, K.; Tahara, M.; Araki, H.; Oishi, K. *MRS Proceedings* **2009**, *1165*.
(8) Li, J.; Wang, H.; Wu, L.; Chen, C.; Zhou, Z.; Liu, F.; Sun, Y.; Han, J.; Zhang, Y. *ACS Applied Materials & Interfaces* **2016**, *8*, 10283.
(9) Nishi, H.; Kuwabata, S.; Torimoto, T. *The Journal of Physical Chemistry C* **2013**, *117*, 21055.
(10) Rath, T.; Haas, W.; Pein, A.; Saf, R.; Maier, E.; Kunert, B.; Hofer, F.; Resel, R.; Trimmel, G. *Solar Energy Materials and Solar Cells* **2012**, *101*, 87.
(11) Roelofs, K. E.; Guo, Q.; Subramoney, S.; Caspar, J. V. *Journal of Materials Chemistry A* **2014**, *2*, 13464.
(12) Riha, S. C.; Parkinson, B. A.; Prieto, A. L. *J. Am. Chem. Soc.* **2009**, *131*, 12054.
(13) Duan, H.-S.; Yang, W.; Bob, B.; Hsu, C.-J.; Lei, B.; Yang, Y. *Adv. Funct. Mater.* **2013**, *23*, 1466.
(14) Tai, K. F.; Gunawan, O.; Kuwahara, M.; Chen, S.; Mhaisalkar, S. G.; Huan, C. H. A.; Mitzi, D. B. *Adv. Energy Mater.* **2015**, *6*.
(15) van Embden, J.; Chesman, A. S. R.; Jasieniak, J. J. *Chemistry of Materials* **2015**, *27*, 2246.
(16) Shin, B.; Gunawan, O.; Zhu, Y.; Bojarczuk, N. A.; Chey, S. J.; Guha, S. *Prog. Photovolt: Res. Appl.* **2013**, *21*, 72.
(17) Pundsack, T. J.; Chernomordik, B. D.; Béland, A. E.; Aydil, E. S.; Blank, D. A. *The journal of physical chemistry letters* **2013**, *4*, 2711.
(18) Shockley, W.; Queisser, H. J. *Journal of Applied Physics* **1961**, *32*, 510.
(19) Hwang, Y.; Park, B.-I.; Lee, B.-S.; Kim, J. Y.; Jeong, J.-H.; Kim, H.; Ko, M. J.; Kim, B.; Son, H. J.; Lee, S. Y.; Lee, J.-S.; Park, J.-K.; Cho, S.-H.; Lee, D.-K. *The Journal of Physical Chemistry C* **2014**, *118*, 27657.
(20) Miskin, C. K.; Yang, W. C.; Hages, C. J.; Carter, N. J.; Joglekar, C. S.; Stach, E. A.; Agrawal, R. *Prog Photovoltaics* **2015**, *23*, 654.
(21) Yin, X.; Tang, C.; Sun, L.; Shen, Z.; Gong, H. *Chemistry of Materials* **2014**, *26*, 2005.
(22) Ben Messaoud, K.; Buffière, M.; Brammertz, G.; ElAnzeery, H.; Oueslati, S.; Hamon, J.; Kniknie, B. J.; Meuris, M.; Amlouk, M.; Poortmans, J. *Progress in Photovoltaics: Research and Applications* **2015**, *23*, 1608.

(23) Liu, X.; Feng, Y.; Cui, H.; Liu, F.; Hao, X.; Conibeer, G.; Mitzi, D. B.; Green, M. *Progress in Photovoltaics: Research and Applications* **2016**, *24*, 879.
(24) Akhavan, V. A.; Goodfellow, B. W.; Panthani, M. G.; Reid, D. K.; Hellebusch, D. J.; Adachi, T.; Korgel, B. A. *Energy & Environmental Science* **2010**, *3*, 1600.
(25) Hages, C. J.; Koeper, M. J.; Agrawal, R. *Solar Energy Materials and Solar Cells* **2016**, *145, Part 3*, 342.
(26) Altamura, G.; Wang, M.; Choy, K.-L. **2016**, *6*, 22109.
(27) Johnson, M.; Baryshev, S. V.; Thimsen, E.; Manno, M.; Zhang, X.; Veryovkin, I. V.; Leighton, C.; Aydil, E. S. *Energy & Environmental Science* **2014**, *7*, 1931.

APPENDIX II-A

SUPPORTING INFORMATION FOR CHAPTER 4: LIGAND-EXCHANGED CZTS NANOCRYSTAL THIN FILMS: DOES NANOCRYSTAL SURFACE PASSIVATION EFFECTIVELY IMPROVE PHOTOVOLTAIC PERFORMANCE?

Lasantha Korala, Max B. Braun, Jason M. Kephart, Zoe Tregillus, and Amy L. Prieto

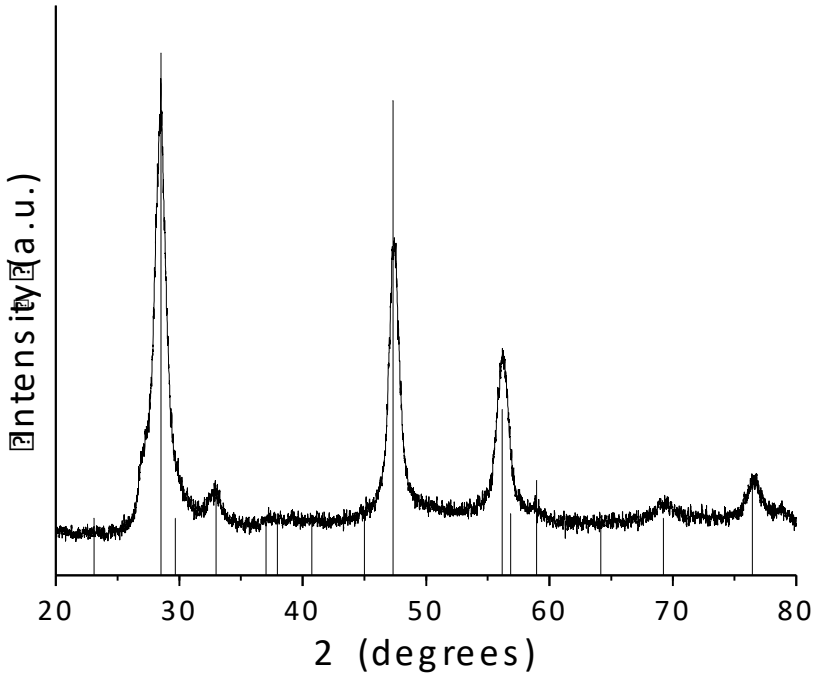

Figure S4.1. XRD pattern of CZTS NCs. The reference lines correspond to kesterite CZTS structure (PDF # 00-026-0575).

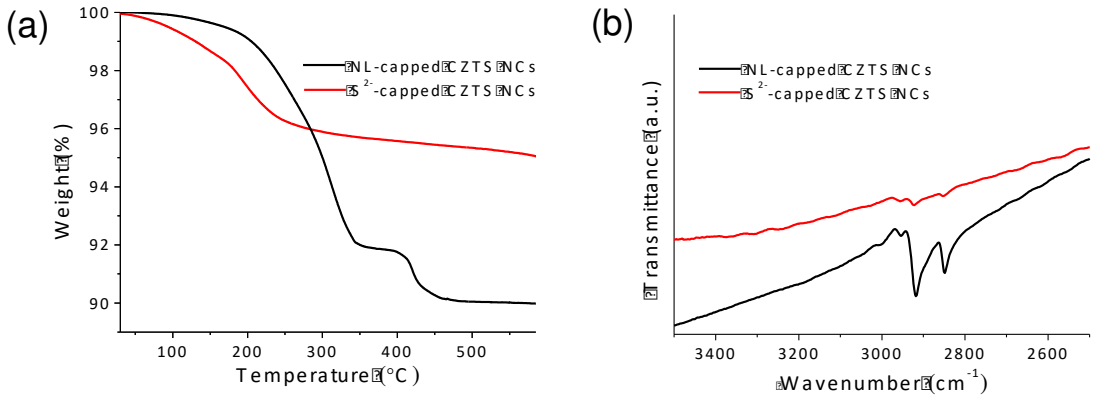

Figure S4.2. (a) TGA curves and (b) ATR-FTIR spectra of CZTS NCs before and after ligand exchange.

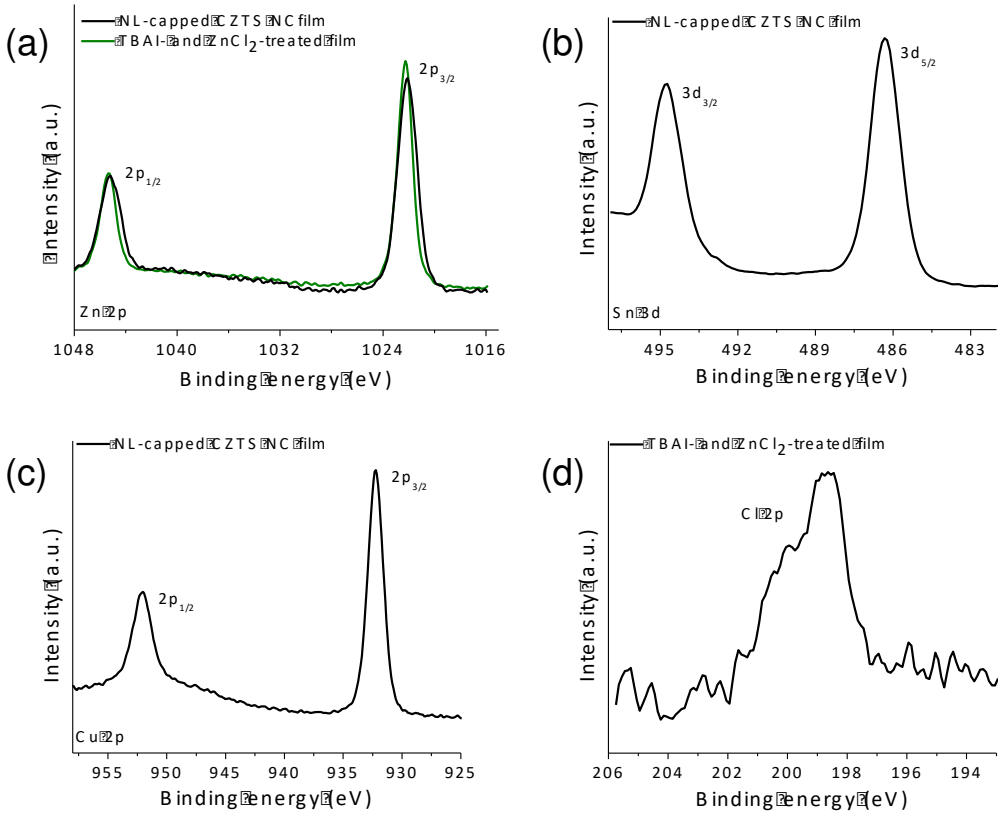

Figure S4.3. High-resolution XPS spectra of (a) Zn 2p, (b) Sn 3d, (c) Cu 2p, and (d) Cl 2p core levels of NL-capped and ligand-exchanged CZTS NC films.

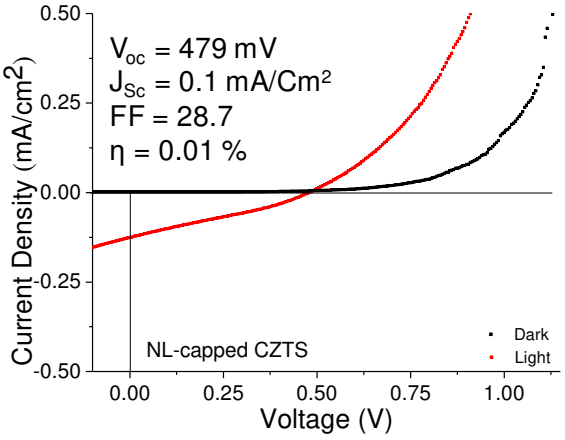

Figure S4.4. The current-voltage characteristic of a solar cell fabricated from NL-capped NC film.

APPENDIX II-B

SUPPORTING INFORMATION FOR: CHAPTER 5: DEPOSITION OF SURFACE MODIFIED $CU_2ZNSN(S_{1-X}SE_X)_4$ NANOCRYSTAL FILMS: THE ROLE OF CHALCOGEN RATIO ON CHARGE TRANSPORT AND PHOTOVOLTAIC DEVICE PERFORMANCE

Max B. Braun, Lasantha Korala , Jason M. Kephart, and Amy L. Prieto

S5.1 Brief Synthetic Discussion

As mentioned in the main manuscript, the composition, size, morphology, as well as the ability to be a colloidal solution were all characteristics of the nanoparticles that needed to be refined for the purposes of this study. The main challenge was to maintain optimal cation ratios throughout the compositions (i.e., Cu/(Zn+Sn) and Zn/Sn ratios = 0.8 and 1.35, respectively). Many different procedures were attempted, most of which resulted in the pure selenium analog samples possessing zinc deficiency, or produced samples that did not suspend well enough for our film deposition procedure.[1-7] Various attempts were made by altering the time of reaction, the concentration and the reactivity of the copper, zinc, and tin precursors (i.e., copper(I) acetate, copper(II) acetylacetonate, copper(I) chloride, copper(II) chloride, zinc chloride, zinc acetate, tin(II) chloride, tin(IV)chloride, and the hydrates of many of these precursors) until the desired composition was found in the suspended product. Interestingly, it was found that increasing zinc precursor reactivity, generally lead to increased amount of zinc in the precipitated product, rather than the suspended particles. Moreover, because we separated the precipitated (generally larger or agglomerated particles) and the suspended product, general trends with concentration and reactivity were difficult to establish. However, it was found that the addition of glycerol, inspired by a synthetic procedure developed by Ji et al., allowed for increased zinc incorporation in the suspended product.[4] This finding lead us to re-test the different procedures until the desired composition, size, and morphology were achieved for the suspended product.

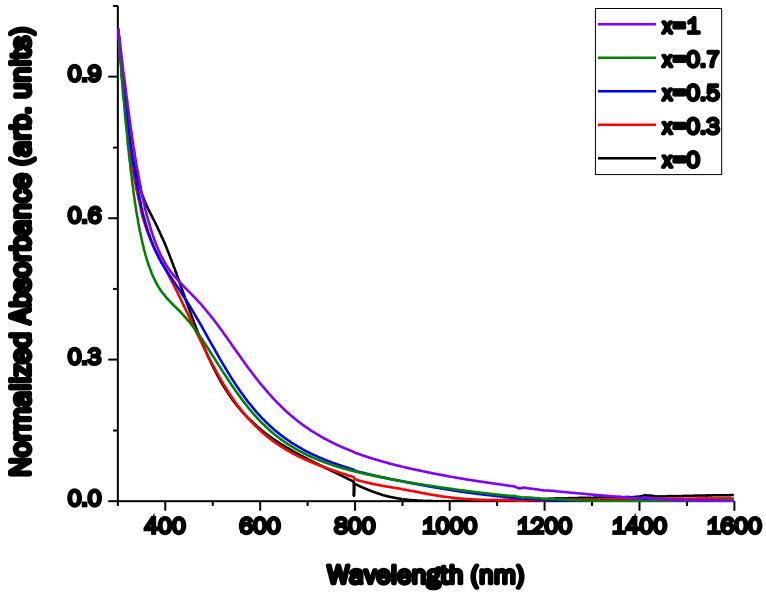

Figure S5.1. Absorption spectra of CZTSSe NCs with different Sulfur-to-selenium ratio.

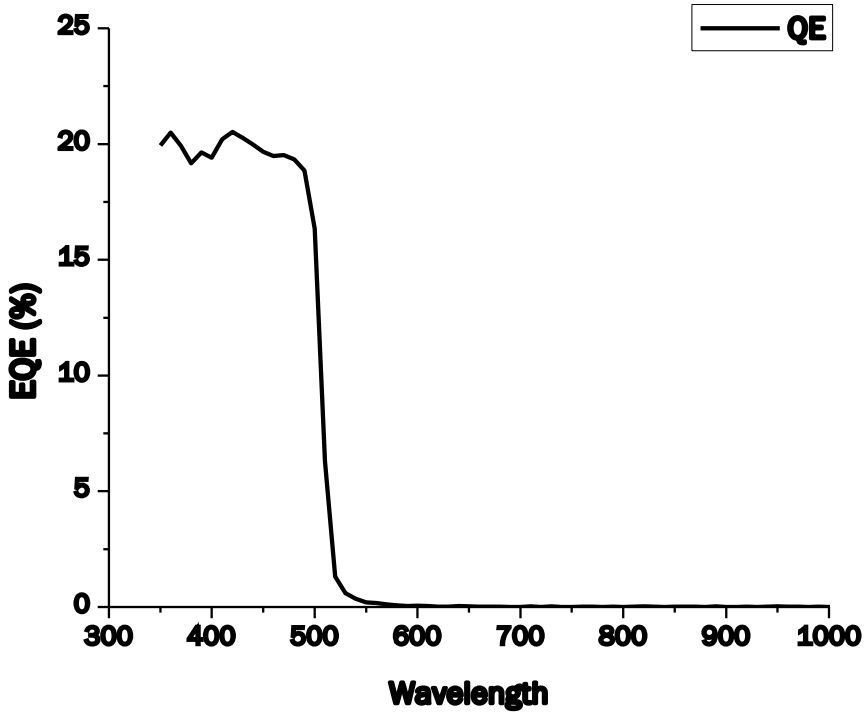

Figure S5.2. EQE spectrum of device c.

Table S5.1. PV characteristics for various CZTSSe cells

Sample	**Eff (%)**	**V_{oc} (V)**	**E_g (eV)**	**$E_g/q-V_{oc}$ (V)**	**$J_{sc\ (mA/cm^2)}$**	**FF (%)**
CZTS*	0.30 ± 0.02	0.661 ± 0.022	1.50	0.81	1.1 ± 0.1	41.2 ± 1.5
$CZTS_{0.7}Se_{0.3}$*	0.37 ± 0.02	0.644 ± 0.004	1.41	0.77	1.3 ± 0.1	43.9 ± 2.2
$CZTS_{0.5}Se_{0.5}$*	0.42 ± 0.03	0.615 ± 0.005	1.30	0.67	1.5 ± 0.1	45.6 ± 0.33
$CZTS_{0.3}Se_{0.7}$*	0.42 ± 0.02	0.615 ± 0.008	1.19	0.57	1.6 ± 0.1	44.2 ± 2.0
CZTSe*	0.35 ± 0.01	0.580 ± 0.005	1.09	0.52	1.5 ± 0.1	41.5 ± 0.9
Z1 (x=1.0)[a]	11.6	0.423	1	0.576	40.6	67.3
Z2 (x=0.89)[a]	10.5	0.424	1.08	0.656	38.5	64.5
Z3 (x=0.66)[a]	10.4	0.495	1.2	0.705	33.8	62.1
Z4 (x=0.46)[a]	9.8	0.532	1.28	0.748	29.8	61.8
Z5 (x=0.28)[a]	9.1	0.577	1.38	0.802	25.8	61.1
Z6 (x=0.10)[a]	6.0	0.557	1.49	0.933	21.3	50.9
D1[b]	12.6	0.513	1.13	0.62	35.2	69.8

*Statistics from 4-6 cells, for each composition, from this study. [a]The devices fabricated by Tai *et al.*[8] [b]The champion CZTSSe single junction PV device to date.[9] Note: Both of these studies used the hydrazine-based process to deposit CZTSSe absorber layer.

REFERENCES

(1) Rath, T.; Haas, W.; Pein, A.; Saf, R.; Maier, E.; Kunert, B.; Hofer, F.; Resel, R.; Trimmel, G. *Solar Energy Materials and Solar Cells* **2012**, *101*, 87.

(2) Ou, K.-L.; Fan, J.-C.; Chen, J.-K.; Huang, C.-C.; Chen, L.-Y.; Ho, J.-H.; Chang, J.-Y. *J Mater Chem* **2012**, *22*, 14667.

(3) Liu, Y.; Yao, D.; Shen, L.; Zhang, H.; Zhang, X.; Yang, B. *Journal of the American Chemical Society* **2012**, *134*, 7207.

(4) Ji, S.; Shi, T.; Qiu, X.; Zhang, J.; Xu, G.; Chen, C.; Jiang, Z.; Ye, C. *Sci. Rep.* **2013**, *3*.

(5) Lee, P.-Y.; Chang, S.-P.; Hsu, E.-H.; Chang, S.-J. *Solar Energy Materials and Solar Cells* **2014**, *128*, 156.

(6) Zhou, H.; Hsu, W.-C.; Duan, H.-S.; Bob, B.; Yang, W.; Song, T.-B.; Hsu, C.-J.; Yang, Y. *Energy Environ. Sci.* **2013**, *6*, 2822.

(7) van Embden, J.; Chesman, A. S. R.; Jasieniak, J. J. *Chemistry of Materials* **2015**, *27*, 2246.

(8) Tai, K. F.; Gunawan, O.; Kuwahara, M.; Chen, S.; Mhaisalkar, S. G.; Huan, C. H. A.; Mitzi, D. B. *Advanced Energy Materials* **2015**.

(9) Wang, W.; Winkler, M. T.; Gunawan, O.; Gokmen, T.; Todorov, T. K.; Zhu, Y.; Mitzi, D. B. *Adv. Energy Mater.* **2014**, *4*, 1301465.